Multianode Photomultiplier Tubes for the LHCb RICH Photodetectors

Reinhardt Julien Ulrich Chamonal

Thesis submitted for the degree of Doctor of Philosophy

School of Physics & Astronomy

The University of Edinburgh

2005

"No general rule, no rigorous rule; a multitude of little rules applicable to each particular case. These rules are not imposed upon us by themselves, and we might amuse ourselves in inventing others; but they could not be cast aside without greatly complicating the laws of physics, mechanics, and astronomy. We choose these rules, therefore not because they are true, but because they are the most convenient"..."In other words, all theses rules, all theses definitions are nothing but the fruits of an unconscious opportunism."

Henri Poincaré, "La mesure du Temps" (1970)

Abstract

The LHCb experiment is being built at the Large Hadron Collider facility at CERN in Geneva, Switzerland. The aim of the experiment is the precise measurement of CP violation parameters in the B-meson system. A critical requirement of the detector is a good pion/kaon separation provided by two Ring Imaging CHerenkov (RICH) counters. This thesis presents studies on the feasibility of using Multianode PhotoMultiplier Tubes (MaPMTs) as photodetectors in the LHCb RICH. We will establish the performances of MaPMTs in magnetic fields and also investigate how to shield them. Finally we present a testbeam analysis of a cluster of MaPMTs equipped with lenses at the CERN PS beam. The purpose of this testbeam was to demonstrate the operation of MaPMTs in a RICH prototype using the LHCb readout electronics.

Declaration

This work represents the effort of many members of the LHCb collaboration at CERN, in Switzerland. I have been an integral part of a small team of people who have been working on the MaPMT project for the LHCb RICH photodetectors. The writing of this thesis is entirely my own work.

Acknowledgements

First of all I would like to thank the Chamonal corp. based on the remote island of Mayotte . They have provided me with the much needed funding, moral support and sun required to accomplish this thesis. Visiting the island turned out to be very beneficial in restoring my peace of mind too. I will always be grateful to my parents for allowing me to pursue a PhD and to be a student for another four years. I would also like to thank my family down in Bourg who became my port d'attache during all these years (the last one was specially long). I would like to acknowledge my supervisor, Franz Muheim for is guidance and understanding and from whom I learnt a lot.. Stephan Eisenhardt who was like a third supervisor to me and with whom I had endless conversations about MaPMTs and not so related topics. Alan Walker my second supervisor for taking care of all the administrative stuff and being very helpfull in general. I also enjoyed working for Sci-fun, thanks. Arthur and Marina who I enjoyed cooking for. Steve Thorn for his great job as a group administrator. James Lawrence for his expertise. Vive Jersey ! Nicolas for bringing more French into my daily life in the office and also together with Greig for letting me win at Badminton. The youngsters: Alan, Show Smith, Judith and Alisdair. Now I am scared of forgetting someone so I am going to be more general.. so thanks to the PPE group as a whole, I really mean it. More formally I would like to thank Steve Jolly for explaining Finite Element Analysis to me. I am deeply grateful to Didier Puertolas and Thierry Gys for their help on setting up the experiment to cross check the FEA, at a time when they were overloaded with the HPD project. Alex Howard for remotely setting up the testbeam simulation on my exotic computer at Edinburgh and for answering all my often dull questions. I had a great time in Geneva with the CERN mafia among whom I'll mention Guy, Lisa, Mountain Dave specially for his expertise in finding the right places to ski, Snow Genie, Dan, Charlotte, all the Andrews and everyone I can't mention because I either forgot their names or I just don't remember right now. Fred for showing me

the salsa club in town. Jeroen for the nice walk up the Jura. I almost forgot to thank the guys from the sandwich family. I won't forget all the CERN secretaries who have been of great help. Members and old members of the sheep-team I really enjoyed the irls and the long discussion on irc. The wine society guys, the first year was tough. Neil for playing badminton and sharing his wine and whiskey expertise. Andrea my flat mate who predicted I was in there for another year. I didn't believe him at the time. Finally I would like to thank the people who had the most influence on my moral. Reto (plus Anna) and Running Bear, the hardcore of the international postgraduate ceremony who remained great friend during all these years. Charles Pat and again James for their friendship. Stef the busy bee and Gwen for the long talks. Finally, promised, I would like to thank Mme Mozon, my English teacher, for allowing me to start this British adventure.

Contents

List of Figures

List of Tables

Chapter 1

Motivation

1.1 Introduction

The apparent absence of primordial anti-matter in the universe requires a deeper understanding of the baryogenesis process by which this asymmetry was created. From the Big Bang theory and the inflation model, one would intuitively expect that matter and its counter part were created in the same quantities. Over time matter and anti-matter would annihilate, leaving the universe significantly less dense than observed. Instead, matter prevails and antimatter is very rare. Furthermore most of the observed universe is made of dark matter. The baryon asymmetry, Ω, can be formulated as the ratio of the baryon number, n_B, to the number of photons, s, in the universe, $\Omega = n_B/s$. It is found from the observation of the number of galaxies, the average number of stars per galaxy... that Ω has a value of only 10^{-10}. If antimatter were to exist today in significant amounts, it would have formed in clusters of "anti-galaxies" colliding with galaxy clusters and producing a large number of detectable γ-rays. The other assumption, that it could exist in a remote, separate place of the universe, would also generate a significant distortion in the cosmic microwave background (CMB) by the interactions at the boundaries. Most of the anti-matter observed in the CMB comes from non-primordial sources and mainly from the production $p + p \rightarrow 3p + \bar{p}$ with a $\bar{p}$ to p ratio of 10^{-4} [2].

In 1967, Sahkarov [1] suggested that baryogenesis arises under the following conditions:

- Baryon number violation in order to be able to produce different type of particles from a species.
- Thermal equilibrium violation to allow for baryonic number violation.
- Charge Parity violation (CP violation).

These cosmological observations together with the baryogenesis conditions provide constraints to the Standard Model (SM) describing the interaction of the realm of subatomic particles. The SM has been verified to an extraordinary level of accuracy. However, the CP violation effects are estimated to be too small to account for the asymmetry of the universe. The study of CP violation in Particle Physics hence provides a way to test the SM and our understanding of the universe.

1.2 Charge and Parity Transformation

Parity transformation (P) is the reflection of all spatial coordinates of a system. It can be achieved in two steps; a mirror reflection on the coordinate plane and a 180° rotation around the axis perpendicular to that plane. This way the handedness[1] of the system is changed. Parity is hence often referred to as mirror or left-right transformation. Algebraically, P changes the sign of the position vector of a particle such that $\vec{r} \rightarrow -\vec{r}$ and quantities such as velocity reverse sign while axial vectors, like angular momentum, remain unchanged.

Charge conjugation (C) is the transposition of a particle to its anti-particle. It is indeed not just the mere change of charge and the term "C" is somewhat misleading, it also reverses all quantum numbers (baryon, lepton, strangeness...). This notion of antiparticle arises from relativistic quantum theory and was confirmed in 1933 with Anderson's discovery of the positron.

It is logical to think that under these transformations, the laws of physics are conserved, i.e. that these are totally symmetric. C and P are called discrete symmetries in that they

[1] the handedness of a particle refers to the sign of its helicity, the component of spin in the direction of motion of the particle.

are groups in which the operator can only take a finite number of values. There is a priori no reason to have different laws when the coordinates are swapped or when considering the realm of anti-particles. This is however not the case.

1.3 Separate C and P Violation

It was suggested in 1956 by T.D Lee and C.N Yang [3], and experimentally confirmed by C.S Wu in 1957 [4], that C and P symmetries are broken in weak interactions: C and P are only partial discrete symmetries. An example violating P and C separately is the decay of the charged pion π^+ into $\nu_\mu\mu^+$. As illustrated in Figure 1.1, C-symmetry means that the π^+ would decay to a anti-muon neutrino with its spin in the opposite direction of its momentum, defined as left-handed(c). However anti-neutrinos are only found as right-handed. Similarly P-symmetry means that the left-handed neutrino of (a) would swap its spin to become right-handed which is not possible. The simultaneous transformation of C and P is however allowed (d).

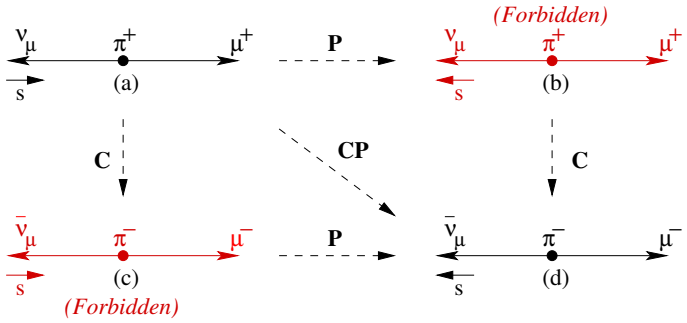

Figure 1.1: *C, P and CP transformation of the decay $\pi^+ \to \nu_\mu\mu^+$: (b) and (c) are not observed in Nature, proving the separate violation of C and P. The vector* s *denotes the spin direction.*

1.4 CP Violation

CP was considered an exact symmetry of nature until it was discovered in 1964 that it was broken in the K_L decay [5]. An example is the K_L decaying to both $\pi^+e^-\overline{\nu_e}$ and $\pi^-e^+\nu_e$, but with a branching ratio slightly different by 6.6×10^{-3}. The K^0 remained for 37 years the only system where CP violation had been observed. The long awaited evidence of CP

violation in the B-meson decays was finally shown in 2001 in B_d^0 decays by the Babar [6] and the Belle [7] experiments.

1.4.1 CP Violation Phenomenology

Let us consider a neutral pseudo scalar particle P^0 and its anti-particle $\overline{P^0}$ which are predominantly subject to the weak interactions under which they are allowed to decay to the same common state. In this case they can oscillate between themselves, i.e. they can mix. The states vectors $|P^0\rangle$ and $|\overline{P^0}\rangle$ define a complete state vector $|\Psi\rangle$ such that:

$$|\Psi\rangle = a(t)\,|P^0\rangle + b(t)\,|\overline{P^0}\rangle + c_1 n_1 + c_2 n_2 + ... \tag{1.1}$$

where a(t) and b(t) are the probability amplitudes of having P^0 or $\overline{P^0}$ at a time t. c_i are the probability amplitudes to decay into other types of particles n_i which will be neglected here. The time dependent decay is given by the Schrödinger equation:

$$i\partial_t\,|\Psi\rangle = \mathbf{H}\,|\Psi\rangle \tag{1.2}$$

where $\mathbf{H}$ is the Hamiltonian matrix of the mixing transitions through the weak interaction $\hat{T}_w$ such that:

$$\mathbf{H} = \begin{pmatrix} H_{11} & H_{12} \\ H_{21} & H_{22} \end{pmatrix} \quad |P^0\rangle = \begin{pmatrix} 1 \\ 0 \end{pmatrix} \quad |\overline{P^0}\rangle = \begin{pmatrix} 0 \\ 1 \end{pmatrix} \tag{1.3}$$

with $H_{11} = \langle P^0|\hat{T}_w|P^0\rangle$, $H_{22} = \langle \overline{P^0}|\hat{T}_w|\overline{P^0}\rangle$, $H_{12} = \langle P^0|\hat{T}_w|\overline{P^0}\rangle$, $H_{21} = \langle \overline{P^0}|\hat{T}_w|P^0\rangle$

$\mathbf{H}$ can be split into its Hermitian mass matrix $\mathbf{M}$ and its decay matrix $\mathbf{\Gamma}$

$$\mathbf{H} = \mathbf{M} - \frac{i}{2}\mathbf{\Gamma} \tag{1.4}$$

CPT-symmetry implies that M_{11}=M_{22}=M and Γ_{11}=Γ_{22}=Γ and hence H_{11}=$H_{22} = H$. The time dependent differential equation then becomes:

$$i\partial_t = \mathbf{H}\begin{pmatrix} a \\ b \end{pmatrix} = \begin{pmatrix} H & H_{12} \\ H_{21} & H \end{pmatrix}\begin{pmatrix} a \\ b \end{pmatrix} = \begin{pmatrix} M - \frac{i}{2}\Gamma & M_{12} - \frac{i}{2}\Gamma_{12} \\ M_{12}^* - \frac{i}{2}\Gamma_{12}^* & M - \frac{i}{2}\Gamma \end{pmatrix}\begin{pmatrix} a \\ b \end{pmatrix} \tag{1.5}$$

with the following solutions:

$$\begin{aligned} |P_1\rangle &= e^{-i(M_1 - \frac{i}{2}\Gamma_1)t} \\ |P_2\rangle &= e^{-i(M_2 - \frac{i}{2}\Gamma_2)t} \end{aligned} \tag{1.6}$$

where $|P_{1,2}\rangle$ are the eigenstates linear combinations of the particle and anti-particle states:

$$|P_1\rangle = p\,|P^0\rangle + q\,|\overline{P^0}\rangle \tag{1.7}$$
$$|P_2\rangle = p\,|P^0\rangle - q\,|\overline{P^0}\rangle$$

with p and q denoting the amount of mixing as complex numbers such that $|p^2| + |q^2|$=1. The relationship between p and q in terms of mass and decay eigenvalues is:

$$\frac{q}{p} = \sqrt{\frac{H_{21}}{H_{12}}} = \sqrt{\frac{M_{12}^* - \frac{i}{2}\Gamma_{12}}{M_{12} - \frac{i}{2}\Gamma_{12}}} \tag{1.8}$$

The eigenvalues of the Hamiltonian are resolved by requiring:

$$|H - EI| = 0 \tag{1.9}$$

where I is the unitary matrix and E is the eigenvalues matrix. That is $(H-E)^2 - H_{12}H_{21} = 0$ which gives two solutions:

$$E_1 = H - \sqrt{H_{12}H_{21}} \tag{1.10}$$
$$E_2 = H + \sqrt{H_{12}H_{21}} \tag{1.11}$$

Rearranging 1.7 and substituting 1.6

$$|P^0(t)\rangle = f_+(t)\,|P^0\rangle + \frac{q}{p} f_-(t)\,|\overline{P^0}\rangle \tag{1.12}$$
$$|\overline{P^0}(t)\rangle = f_+(t)\,|\overline{P^0}\rangle + \frac{p}{q} f_-(t)\,|P^0\rangle \tag{1.13}$$

with $f_\pm(t) = \frac{1}{2}\left[e^{-i(m_H - \frac{i}{2}\Gamma_H)t} \pm e^{-i(m_L - \frac{i}{2}\Gamma_L)t}\right]$. The probabilities of finding P^0 or $\overline{P^0}$ at time t for an initial state P^0 are then:

$$|\,\langle P^0|P^0(t)\rangle\,|^2 = |f_+(t)|^2 \tag{1.14}$$
$$|\,\langle \overline{P^0}|P^0(t)\rangle\,|^2 = |\frac{q}{p} f_-(t)|^2 \tag{1.15}$$

Generalising 1.15 for the time-dependent decay amplitude of a particle going to any final state F including mixing gives:

$$\langle F|H|P^0(t)\rangle = f_+(t)\,\langle F|H|P^0\rangle + \frac{q}{p} f_-(t)\,\langle F|H|\overline{P^0}\rangle \tag{1.16}$$
$$\langle F|H|\overline{P^0}(t)\rangle = f_+(t)\,\langle F|H|\overline{P^0}\rangle + \frac{p}{q} f_-(t)\,\langle F|H|P^0\rangle \tag{1.17}$$

or considering the decay rates Γ and setting $A_f = \langle F|H|P^0(t)\rangle$ and $\overline{A_f} = \langle F|H|\overline{P^0}(t)\rangle$:

$$\Gamma_{(P^0(t)\to F)} \propto |A_f f_+(t) + \frac{q}{p}\overline{A_f} f_-(t)|^2 \tag{1.18}$$

$$\Gamma_{(\overline{P^0}(t)\to F)} \propto |\frac{p}{q}(A_f f_+(t)) + \frac{q}{p}\overline{A_f} f_-(t))|^2 \tag{1.19}$$

CP violation hence occurs if $\frac{q}{p} \neq 1$ and/or when there is a difference in the decay amplitudes: $|A_f| \neq |\overline{A_f}|$. It is convenient to quantify CP violation with the following observable:

$$\Lambda_f = \frac{q}{p}\frac{\overline{A_f}}{A_f} \tag{1.20}$$

Λ_f shows that there are three types of CP violation:

- Indirect CP violation also called CP violation in the mixing when $|q/p| \neq 1$.
- Direct CP violation in the decay amplitudes where $|A_f| \neq |\overline{A_f}|$ in charged or neutral systems.
- CP violation in the interference between both the mixing and the decay amplitude.

1.4.2 CP Violation and the Standard Model

In the Standard Model (SM) charged weak interactions are defined by the following Lagrangian [12]:

$$\mathcal{L} = \frac{-g_w}{\sqrt{2}}\overline{U_L}\gamma^\mu V_{CKM} D_L W_\mu^+ + h.c. \tag{1.21}$$

where $\overline{U_L} = (u_L, c_L, t_L)^T$ and $D_L = (d_L, s_L, b_L)^T$ are the left-handed quark fields ($q_L = (1-\gamma_5)q/2$) with u the up quark, c the charmed quark, t the top, d the down, s the strange and b is the bottom or also called beauty quark. W_μ^+ is the W boson field, g_w is the weak gauge coupling, and V_{CKM} is the unitary Cabibbo-Kobayashi-Maskawa mixing matrix defined as:

$$V_{CKM} = \begin{pmatrix} V_{ud} & V_{us} & V_{ub} \\ V_{cd} & V_{cs} & V_{cb} \\ V_{td} & V_{ts} & V_{tb} \end{pmatrix} \tag{1.22}$$

where V_{jk} denotes the coupling between the quarks j and k. The rotation between the weak eigenstates (d', s', b') and the mass eigenstates (d, s, b) is described by:

$$\begin{pmatrix} d' \\ s' \\ b' \end{pmatrix} = V_{CKM} \begin{pmatrix} d \\ s \\ b \end{pmatrix} \tag{1.23}$$

Before 1973, the quark mixing was expressed by Cabibbo as a 2×2 matrix because only two families of quarks were known. In order to incorporate CP violation the mixing matrix needs to be complex. This could only be achieved with a three (or higher) dimensional matrix and hence a third generation of quarks was introduced [8]. A phase is introduced to the matrix by applying a phase factor to every row and column $V_{jk} \rightarrow e^{i(\phi_j - \phi_k)} V_{jk}$, with i,j=1,2,3 for the generation labels. The CKM matrix is then described by four real parameters where one is a phase parameter while the other three are rotation angles in flavour space. The standard parametrisation proposed by Harari and Leurer (1986) [9] is:

$$V_{CKM} = \begin{pmatrix} c_{12}c_{13} & s_{12}c_{13} & s_{13}e^{-i\delta_{13}} \\ -s_{12}c_{23} - c_{12}s_{23}s_{13}e^{i\delta_{13}} & c_{12}c_{23} - s_{12}s_{23}s_{13}e^{i\delta_{13}} & s_{23}c_{13} \\ s_{12}s_{23} - c_{12}c_{23}s_{13}e^{i\delta_{13}} & -c_{12}s_{23} - s_{12}c_{23}s_{13}e^{i\delta_{13}} & c_{23}c_{13} \end{pmatrix} \tag{1.24}$$

where $c_{jk} = cos\theta_{jk}$, $s_{jk} = sin\theta_{jk}$ with $(0 \leq \theta_{jk} \leq \pi/2)$ and $s_{jk} > 0$, $c_{jk} > 0$.

A useful and commonly used representation is the Wolfenstein parametrisation (1984) [10]. It emphasises the coupling between the quark transitions. It relies on a series expansion in the experimentally determined parameter $s_{12} = \lambda \approx 0.22$, known as the Cabibbo angle:

$$V_{CKM} = \begin{pmatrix} 1 - \frac{\lambda^2}{2} & \lambda & A\lambda^3(\rho - i\eta) \\ -\lambda & 1 - \frac{\lambda^2}{2} & A\lambda^2 \\ A\lambda^3(1 - \rho - i\eta) & -A\lambda^2 & 1 \end{pmatrix} + \mathcal{O}(\lambda^n) \tag{1.25}$$

where the following substitutions have been made $s_{23} = A\lambda^2$ and $s_{13}e^{-i\delta} = A\lambda^3(\rho - i\eta)$ and $\mathcal{O}(\lambda^n)$ is the next n leading order. CP violation occurs for $\eta \neq 0$.
Greater precision is achieved by adding the corresponding leading orders. The LHC experiments are foreseen to have an insight to the fifth order.

Jarlskog [11] pointed out that because the matrix is unitary, the CP violation can be described via an invariant quantity:

$$J = \pm\mathcal{I}m(V_{ij}V_{kl}V_{il}^{*}V_{kj}^{*}) \approx A^2\lambda^6\eta = \mathcal{O}(10^{-5}) \tag{1.26}$$

where i, j, k, l are the quark flavours with $i \neq k$, $j \neq l$. Hence showing that overall, CP violation is actually a small effect in the SM and thus needs to be searched in rare decays.

1.4.3 CP Violation in the B-meson system: $B_q^0 \longleftrightarrow \overline{B_q^0}$ mixing

CP violation has only been extensively tested in the neutral kaon system and demonstrated the consistency of the SM. In the new millennium the study of CP violation has extended to the B-mesons which involves the third generation bottom quarks flavour transitions. Table 1.1 shows the weakly decaying B-mesons with their quark content, masses and lifetimes.

Mesons	Quark Content	Mass (MeV)	Lifetime ($10^{-12}s$)
B^+	$\overline{b}u$	5279.0±0.5	1.671±0.018
B_d^0	$\overline{b}d$	5279.4±0.5	1.536±0.014
B_s^0	$\overline{b}s$	5369.6±2.4	1.464±0.057
B_c^+	$\overline{b}c$	6400±400	$0.46^{+0.18}_{-0.16}$

Table 1.1: *Masses and lifetimes of the B-mesons [9].*

From the particles shown in Table 1.1 only neutral particles are of interest. Even though in principle CP violation in the charged decay can be measured, theoretical predictions are very hazardous due to hadronic uncertainties [13]. CP violation studies is hence mainly focused on the $B_q^0 - \overline{B_q^0}$ systems from which the box diagram is shown in Figure 1.2. Based on experimental and theoretical arguments [13] it is also assumed that there is no indirect CP violation in the mixing of B-meson decays: $|q/p| = 1$. This leaves two possible forms: the direct CP violation and CP violation in the interference for which the decays rates become:

$$\Gamma[B^0(t) \to f] = \frac{|A_f|^2 e^{-\Gamma t}}{2}\left[1 + |\Lambda_f|^2 + (1 - |\Lambda_f|^2)cos(\Delta mt) + 2\mathcal{I}m(\Lambda_f)sin(\Delta mt)\right] \tag{1.27}$$

$$\Gamma[\overline{B^0}(t) \to f] = \frac{|A_f|^2 e^{-\Gamma t}}{2}\left[1 + |\Lambda_f|^2 - (1 - |\Lambda_f|^2)cos(\Delta mt) - 2\mathcal{I}m(\Lambda_f)sin(\Delta mt)\right] \tag{1.28}$$

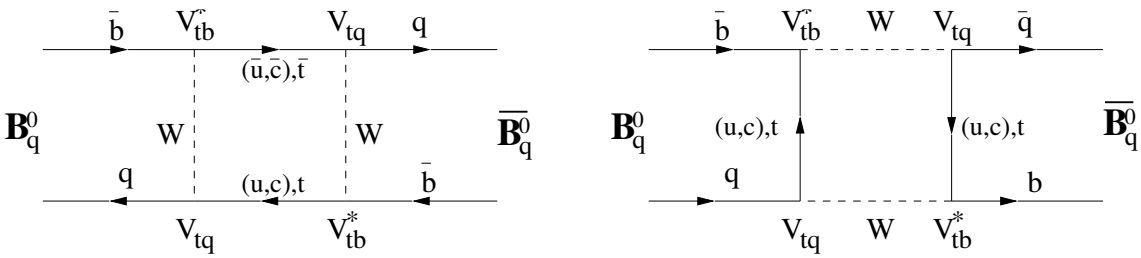

Figure 1.2: *The lowest-order Feynman diagrams for* $B_q^0 \longleftrightarrow \overline{B_q^0}$ *mixing, where* q *can either be a down or a strange quark. The intermediate quarks can be up, charm or top, but since the mixing amplitude is proportional to the mass in the loop, the* t*-contribution is predominant.*

giving the following CP-violating asymmetry for a B-meson going to a final state f:

$$A_{CP}(t) \equiv \frac{\Gamma[B^0(t) \to f] - \Gamma[\overline{B^0}(t) \to f]}{\Gamma[B^0(t) \to f] + \Gamma[\overline{B^0}(t) \to f]} \tag{1.29}$$

$$= \frac{(1 - |\Lambda_f|^2)cos(\Delta mt) + 2\mathcal{I}m(\Lambda_f)sin(\Delta mt)}{(1 + |\Lambda_f|^2)cosh(\Delta\Gamma t/2) + 2Re(\Lambda_f)sinh(\Delta\Gamma t/2)} \tag{1.30}$$

In the case of B_d mesons it is assumed that $\Delta\Gamma = 0$ and the equation hence becomes:

$$A_{CP}(t) = \frac{1 - |\Lambda_f|^2}{1 + |\Lambda_f|^2}cos(\Delta mt) + \frac{2\mathcal{I}m\Lambda_f}{1 + |\Lambda_f|^2}sin(\Delta mt) \tag{1.31}$$

$$= a^{dir}cos(\Delta mt) + a^{int}sin(\Delta mt) \tag{1.32}$$

where a^{int} measures CP violation in the interference and a^{dir} measures direct CP violation.

1.4.4 The Unitary Triangle

The CKM matrix and the unitary condition of equation 1.22 lead to nine orthogonality conditions equations from which two are of interest for B-meson decays.

$$V_{ud}V_{ub}^* + V_{cd}V_{cb}^* + V_{td}V_{tb}^* = 0 \tag{1.33}$$

$$V_{tb}V_{ub}^* + V_{ts}V_{us}^* + V_{td}V_{ud}^* = 0 \tag{1.34}$$

These two relations can be drawn as triangles shown in Figure 1.3. Both triangles are the same up to the third order Wolfenstein Parametrisation. The triangle on the left is referred to as the "Unitary Triangle" while the second is only distinguishable from the

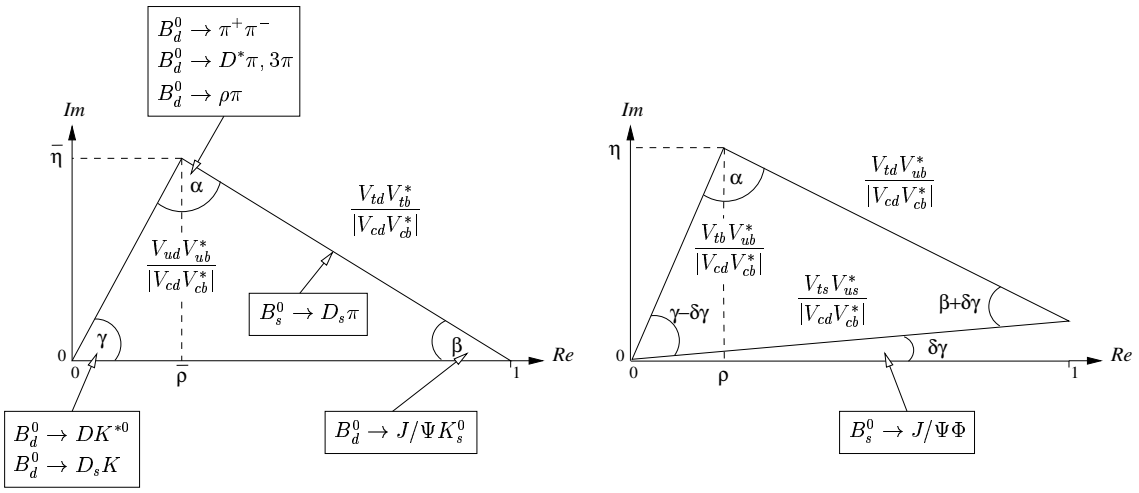

Figure 1.3: *The two unitary triangles where* $\overline{\rho} = \rho(1-\lambda^2/2)$ *and* $\overline{\eta} = \eta(1-\lambda^2/2)$ *in the fifth order Wolfenstein's parametrisation. Some of the B-meson decays which experimentally constrain the parameters triangles are also shown.*

first with a precision to the fifth order in the parametrisation. The angles of the triangles are defined as follow:

$$\begin{aligned} \alpha &= arg\left(-\frac{V_{td}V_{tb}^*}{V_{ud}V_{ub}^*}\right) \\ \beta &= arg\left(-\frac{V_{cd}V_{cd}^*}{V_{td}V_{tb}^*}\right) \\ \gamma &= arg\left(-\frac{V_{ud}V_{ub}*}{V_{cd}V_{cb}*}\right) \end{aligned} \tag{1.35}$$

These angles can be determined using the decays shown in Figure 1.3. These particles decays are rare and have small branching ratios driving the need for high statistics. Experiments are being specially dedicated to the production of these B-mesons: the B-factories. Their goal is to over-constrain the triangle parameters. A non-closure of the triangles i.e. $\alpha + \beta + \gamma \neq \pi$ would suggest that the understanding of CP violation within the SM is incomplete and thus new physics beyond it is required.

The precision measurement on B physics have been greatly improved by current B factories such as Belle and Babar. They however do not allow for the study of all B-mesons and only allow for precise measurements of β. Their quark production mechanism is indeed based on $e^+e^- \to \Upsilon(4s)$ where only B_d^0 $\overline{B_d^0}$ and $B^\pm$ are produced. The new LHCb experiment will however make use of the high energy proton-proton LHC collider. The new collider will allow to produce all species of B hadrons in the approximate ratio: $B^\pm : B_d^0 : B_s^0$:b−baryon: $B_c^\pm \approx 39 : 39 : 11 : 12 : 1\%$ [14]. This will allow to overconstrain the unitary triangle and also to gain access to the second triangle of Figure 1.3. Of

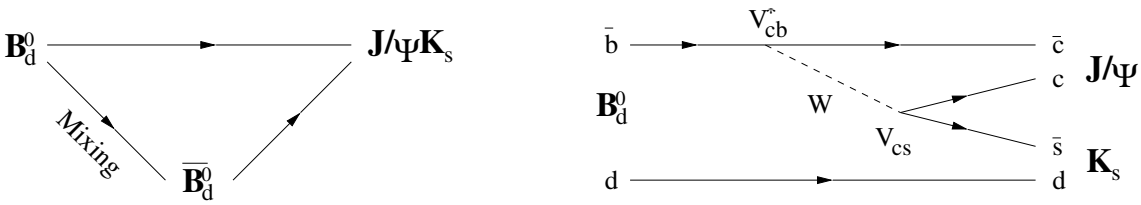

Figure 1.4: *The $B_d^0 \to J/\Psi K_s$ decay diagram illustrating the mixing (left) and its tree-level contribution (right).*

relevance for this thesis we are presenting the $B_d^0 \to J/\Psi K_s$ decay which will be used by the LHCb experiment as a reference channel, the $B_d^0 \to \pi^+\pi^-$ and $B_s^0 \to D_s K$ decays for which it is essential to have a good particle identification system provided by the LHCb Ring Imaging Cherenkov Detectors described in Chapter 3, see Figures 3.12 and 3.13.

Probing β with $B_d^0 \to J/\Psi K_s$

The $B_d^0 \to J/\Psi K_s$ decay is shown in the diagrams of Figure 1.4. This so called "golden channel" is the most tested channel from the BaBar and Belle factories. The decay is dominated by its tree level diagram. CP violation arises due to the interference with $B^0 - \overline{B^0}$ and $K^0 - \overline{K^0}$ mixing, therefore:

$$\Lambda_{(B_d^0 \to J/\Psi K_s)} = \left(\frac{q}{p}\right)_{B_d^0} \left(\frac{q}{p}\right)_{K^0} \left(\frac{\overline{A}}{A}\right)_{J/\Psi K_s} \tag{1.36}$$

$$= -\left(\frac{V_{tb}^* V_{td}}{V_{tb} V_{td}^*}\right) \left(\frac{V_{cs} V_{cd}^*}{V_{cs}^* V_{cd}}\right) \left(\frac{V_{cb} V_{cs}^*}{V_{cb}^* V_{cs}}\right) \tag{1.37}$$

Direct CP violation in this channel is negligible and hence $|\Lambda_{B_d^0 \to J/\Psi K_s}|^2 = 1$. Equation 1.30 can then be simplified to:

$$A_{CP}(t) = \frac{\Gamma[B_d^0(t) \to J/\Psi K_s] - \Gamma[\overline{B_d^0}(t) \to J/\Psi K_s]}{\Gamma[B_d^0(t) \to J/\Psi K_s] + \Gamma[\overline{B_d^0}(t) \to J/\Psi K_s]} \tag{1.38}$$

$$= sin(\Delta m t)\, a_{J/\Psi K_s}^{int} \tag{1.39}$$

with

$$a_{J/\Psi K_s}^{int} = \mathcal{I}m(\Lambda_{B_d^0 \to J/\Psi K_s}) = \mathcal{I}m\left(\frac{q}{p}\frac{\overline{A}_{J/\Psi K_s}}{A_{J/\Psi K_s}}\right) = \mathcal{I}m\left(\frac{V_{td}}{V_{td}^*}\right) = \mathcal{I}m(e^{-i2\beta}) = -sin(2\beta) \tag{1.40}$$

and thus the asymmetry is the amplitude is related to β by:

$$A_{CP}(t) = -sin(\Delta m t)\, sin(2\beta) \tag{1.41}$$

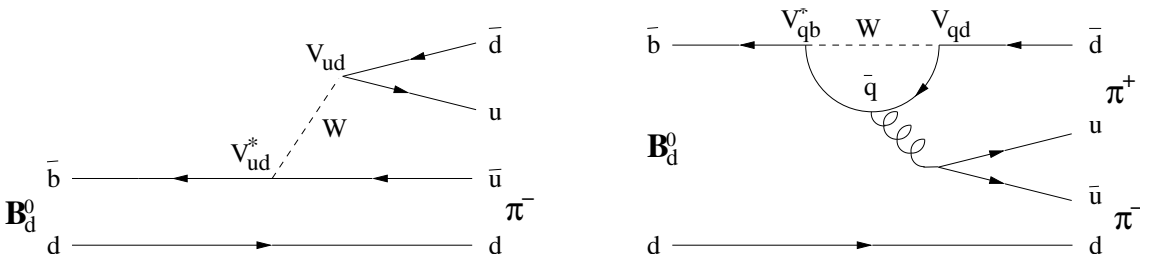

Figure 1.5: *The $B_d^0 \to \pi^+\pi^-$ decay diagrams showing its tree-level (left) and its leading penguin (right) contributions where $\bar{q}$ can be a $\bar{t}$, $\bar{c}$ or $\bar{u}$ quark.*

Probing α with $B_d^0 \to \pi^+\pi^-$

The $B_d^0 \to \pi^+\pi^-$ decay, shown in Figure 1.5, allows us to determine the α angle of the unitary triangle. The final state is generated by the b→u tree diagram and by the small but not negligible b→d penguin diagram. The mixing phase in Equation 1.20 is given by:

$$\Lambda_{(B_d^0 \to \pi^+\pi^-)} = \left(\frac{q}{p}\right)_{B_d^0} \left(\frac{\overline{A}}{A}\right)_{\pi\pi} \tag{1.42}$$

$$= -\left(\frac{V_{tb}^* V_{td}}{V_{tb} V_{td}^*}\right) \left(\frac{V_{ud}^* V_{ub}}{V_{ud} V_{ub}*}\right) \tag{1.43}$$

and the CP asymmetry in the decay is then given to the sign by Equation 1.30 as:

$$A_{CP}(t) = \frac{\Gamma[B_d^0(t) \to \pi^+\pi^-] - \Gamma[\overline{B_d^0}(t) \to \pi^+\pi^-]}{\Gamma[B_d^0(t) \to \pi^+\pi^-] + \Gamma[\overline{B_d^0}(t) \to \pi^+\pi^-]} \tag{1.44}$$

$$= a^{int}(\Delta m t) - a^{dir} cos(\Delta m t) \tag{1.45}$$

where

$$a_{\pi\pi}^{int} = \frac{2\mathcal{I}m(\Lambda_{\pi\pi})}{1 + |\Lambda_{\pi\pi}|^2} \quad a_{\pi\pi}^{dir} = \frac{1-|\Lambda_{\pi\pi}|^2}{1+|\Lambda_{\pi\pi}|^2} \quad \Lambda_{\pi\pi} = \frac{q}{p}\frac{\bar{A}_{\pi\pi}}{A_{\pi\pi}} \tag{1.46}$$

The penguin pollution introduces a strong phase factor making the relation to the unitary triangle more difficult . a^{int} and a^{dir} can be re-expressed in terms of the penguin, P, and tree contribution, T, to relate them to the α angle as:

$$a_{\pi\pi}^{int} = sin(2\alpha) + 2\left|\frac{P}{T}\right| cos(\delta_{P/T}) cos(2\alpha) sin\alpha \tag{1.47}$$

$$a_{\pi\pi}^{dir} = 2\left|\frac{P}{T}\right| sin(\delta_{P/T}) sin\alpha \tag{1.48}$$

where $\delta_{P/T}$ is the difference between the strong phases of the penguin pollution and the tree contribution.

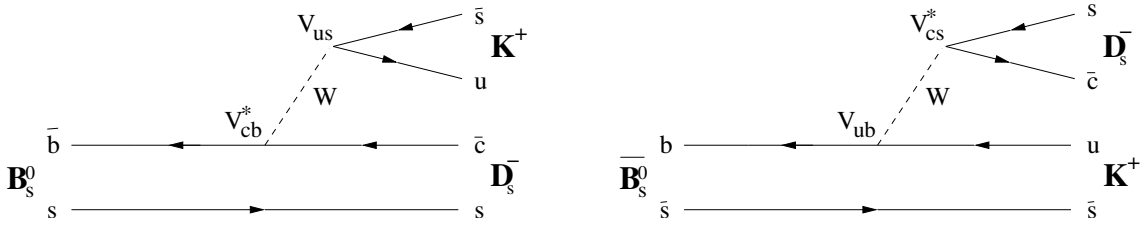

Figure 1.6: *The $B_s^0, \overline{B_s^0} \to D_s^- K^+$ decay diagrams.*

Probing γ from $B_s^0 \to D_s^- K^+$

The $B_s^0 \to D_s^- K^+$ decay shown in Figure 1.6 is different from the precedent decays in that there is no Penguin pollution. Instead the B_s and $\overline{B_s}$ can decay to the same final state via tree diagrams with a phase difference of $-\gamma$. While theoretically clean the selection of this mode is experimentally specially challenging. $D_s K$ is indeed kinematically very similar to the $D_s \pi$ decay which has a branching ratio 20 times bigger requiring an adequate mean of discrimination. The second issue is that $D_s K$ is not a CP eigenstate and there is a CP conserving contribution Δ due to the strong interaction. This extra phase can be separated using the CP-conjugate, $B_s^0, \overline{B_s^0} \to D_s^+ K^-$ which has a similar branching ratio such that: $|\Lambda_{D_s^- K^+}| = |\Lambda_{D_s^+ K^-}|$ and:

$$\mathcal{I}m(\Lambda_{D_s^- K^+}) = sin(-\gamma + 2\delta\gamma + \Delta) \tag{1.49}$$

$$\mathcal{I}m(\overline{\Lambda_{D_s^- K^+}}) = sin(\gamma - 2\delta\gamma + \Delta) \tag{1.50}$$

Furthermore the $\Delta\Gamma$ in Equation 1.30 is not negligible in the B_s system. The asymmetry in the amplitude to the final state remains hence complicated:

$$A_{CP}(t) \approx \frac{(1 - |\Lambda_{D_s K}|^2) cos(\Delta m t) + 2\mathcal{I}m(\Lambda_{D_s K}) sin(\Delta m t)}{(1 + |\Lambda_{D_s K}|^2) cosh(\Delta\Gamma t/2) + 2Re(\Lambda_{D_s K}) sinh(\Delta\Gamma t/2)} \tag{1.51}$$

$\Delta\Gamma$ and Δm must be independently determined from other decays: $2\delta\gamma - \gamma$ is measured by comparing $\mathcal{I}m(\overline{\Lambda_{D_s^- K^+}})$, obtained from the measurement of the asymmetry $A_{D_s^+ K^-}$ and $\mathcal{I}m(\Lambda_{D_s^- K^+})$, obtained from the measurement of the asymmetry $A_{D_s^- K^+}$. The angle $2\delta\gamma$ will also be measured from $B_s^0 \to J/\Psi\Phi$ allowing to further constrain the angle γ.

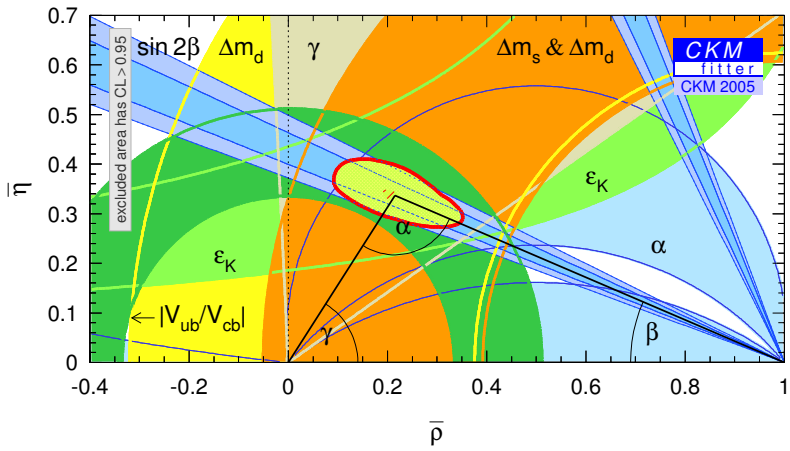

Figure 1.7: *The current experimental bounds on the Unitary Triangle [16].*

1.5 Experimental Results on Testing the Standard Model

The current experimental status [15] of the CKM matrix is as follows:

$$\begin{pmatrix} |V_{ud}| & |V_{us}| & |V_{ub}| \\ |V_{cd}| & |V_{cs}| & |V_{cb}| \\ |V_{td}| & |V_{ts}| & |V_{tb}| \end{pmatrix} = \begin{pmatrix} 0.97399 \pm 0.00046 & 0.2265 \pm 0.0020 & 0.00379^{+0.00025}_{-0.00023} \\ 0.2264 \pm 0.0020 & 0.97316^{+0.00046}_{-0.00047} & 0.04113^{+0.00134}_{-0.0058} \\ 0.00807^{+0.00045}_{-0.00035} & 0.04050^{+0.00133}_{-0.0057} & 0.999147^{+0.000024}_{-0.000057} \end{pmatrix} \tag{1.52}$$

Where $|V_{ud}|$ is determined from nuclear decays, $|V_{us}|$ comes from semi-leptonic kaon and hyperon decays, $|V_{cd}|$ is measured from deep inelastic neutrino excitation of charm, $|V_{cs}|$ is extracted from semi-leptonic decays of charm mesons, $|V_{ub}|/|V_{cb}|$ is obtained from the end point of the lepton-energy spectrum in semi-leptonic B-meson decays and finally $t \to bl^+\nu_l$ gives $|V_{tb}^2|/(|V_{td}^2| + |V_{ts}^2|| + V_{tb}^2|)$.

The current values on the unitary triangle angles are:

$$\begin{aligned} \alpha &= 93.1^{\circ\,+9.6}_{-12.5} \\ \beta &= 23.1^{\circ\,+1.5}_{-1.5} \\ \gamma &= 58.2^{\circ\,+6.7}_{-5.4} \end{aligned} \tag{1.53}$$

with the corresponding unitary triangle for the B_d^0 system shown in Figure 1.7.

Chapter 2

The LHCb Experiment

The Large Hadron Collider beauty experiment (LHCb) is being built for the precise measurement of CP violation parameters in a wide range of B-meson decays. The LHCb detector will use the Large Hadron Collider (LHC), a new accelerator under construction at CERN[1]. A layout of the LHC accelerator complex and its experiments is given in Figure 2.1. The LHC will allow high precision measurements, extending the scope of the existing measurements from the BaBar and Belle experiments. While the former are only analysing B_d and B_u decay modes, LHCb will measure a wider range of B-hadron decays including B_s-mesons and Λ_b-baryons (bud). The LHCb experiment will test the Standard Model (SM) to its limits and beyond, probing for new Physics.

The LHC will operate at a centre-of-mass energy of 14 TeV and it will produce collisions with a large particle multiplicity. This poses a challenge in charged particle tracking and identification within the detector environment. The b-hadrons will be produced predominantly in a forward and backward cone. LHCb will however study only one of these cones. For this reason the detector has been designed as a single-arm spectrometer with an angular coverage of 10 mrad to 300 (250) mrad in the bending (non-bending) plane.

This chapter is aimed at giving a brief description of the main LHCb detector components with some details of their performances. The reader is invited to go through the references for more details.

[1] European Council for Nuclear Research in Geneva - Switzerland

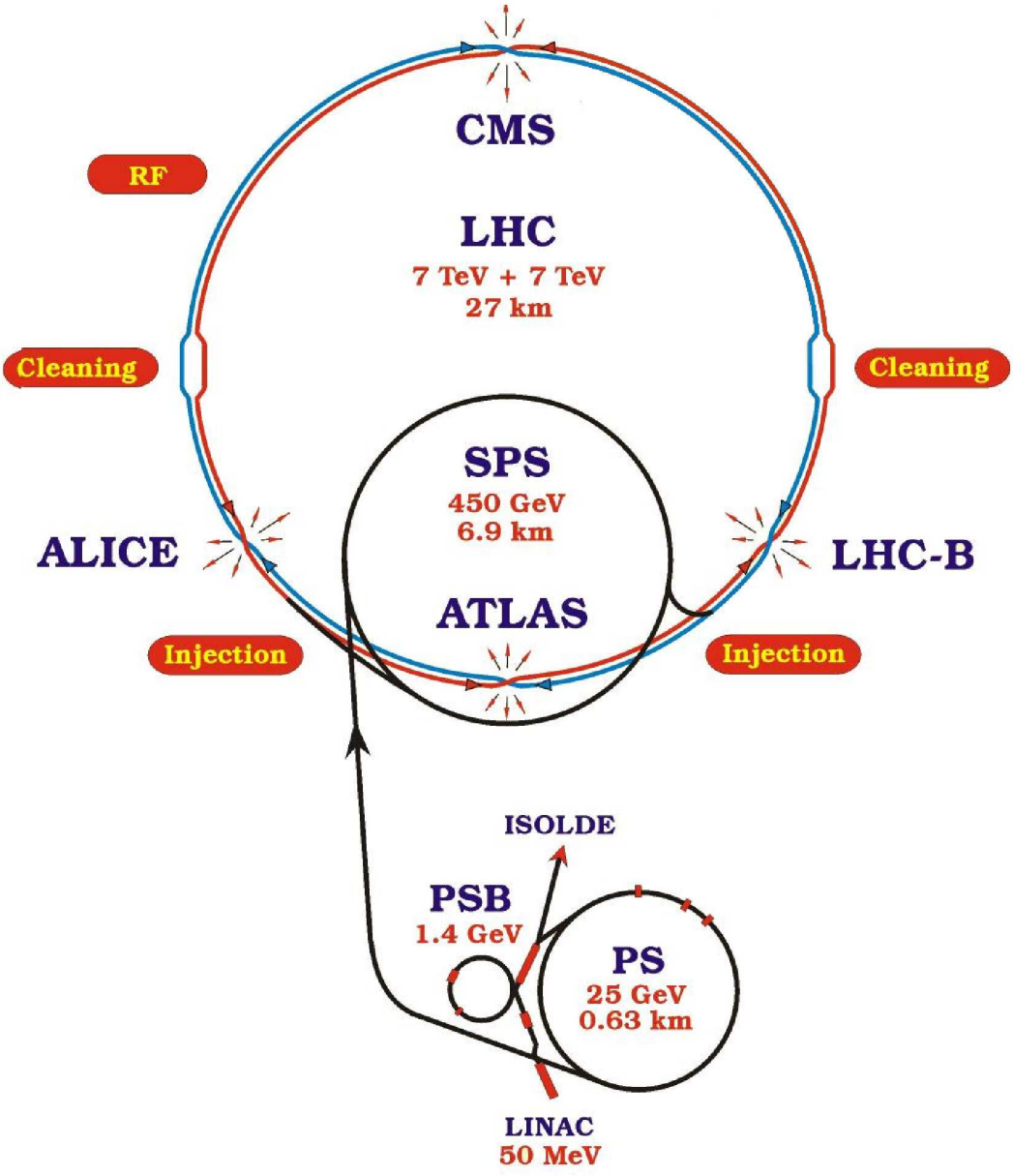

Figure 2.1: *The Large Hadron Collider with its injection beams and its experiments. The ALICE experiment aims at studying heavy-ions interactions. The CMS and ATLAS experiments are general purpose detectors and focus on the search for the Higgs particle and new physics (SUSY..). The LHCb experiment will study CP violation and rare decays.*

2.1 The LHCb Detector

The LHCb detector [38] is shown in Figures 2.2 and 2.3. A Vertex detector (VELO) placed around the interaction point measures track parameters of charged particles. A system of tracking stations on both sides of a magnet separates charged particles for the reconstruction of the trajectories of charged tracks. The particle identification is performed by two Ring Imaging CHerenkov (RICH) detectors, an Electromagnetic CALorimeter (ECAL) with a preshower detector, a Hadron CALorimeter (HCAL) and a muon detector. The RICH1 detector is located before the magnet to measure low momentum particles while the other detectors are positioned downstream of the magnet to capture high momentum tracks. The installation of all detectors will require 16 months and the whole detector is expected to be completed by the time the LHC is ready to operate in 2007. Most of the electronics and online computer farms will be housed behind the shielding wall as visible in Figure 2.2.

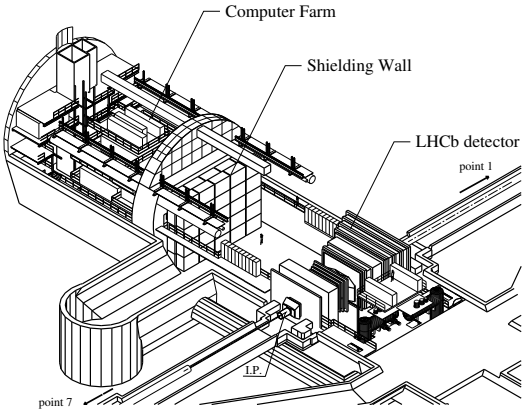

Figure 2.2: *3D-isometric view of the LHCb detector in the underground area UX85. IP stands for Interaction Point.*

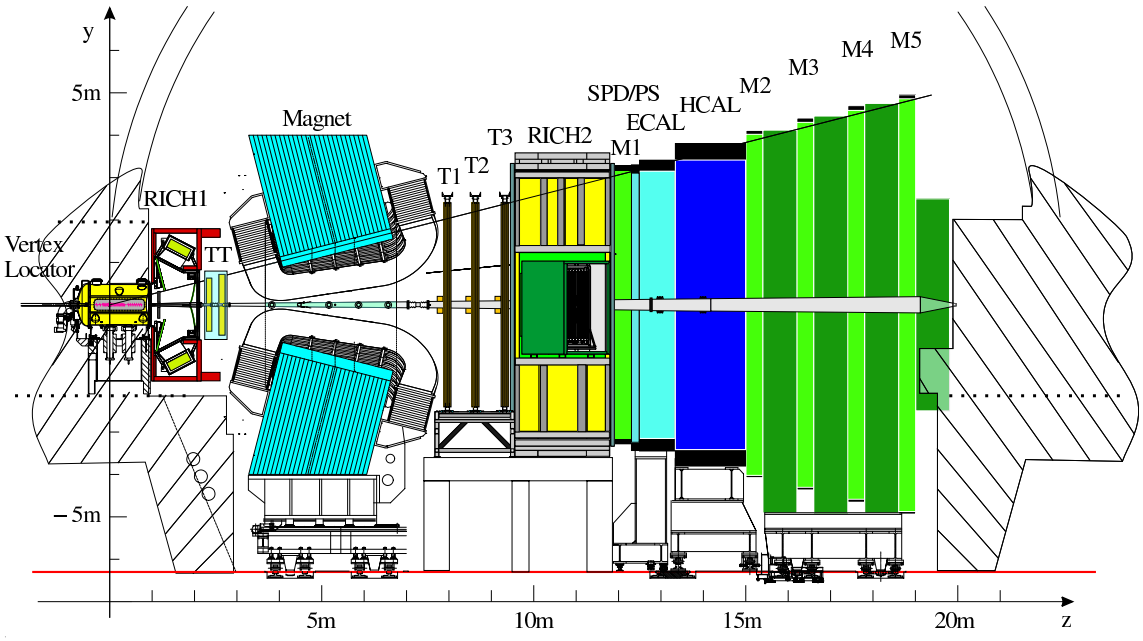

Figure 2.3: *Side cut of the LHCb detector. The x-coordinate is perpendicular to the page.*

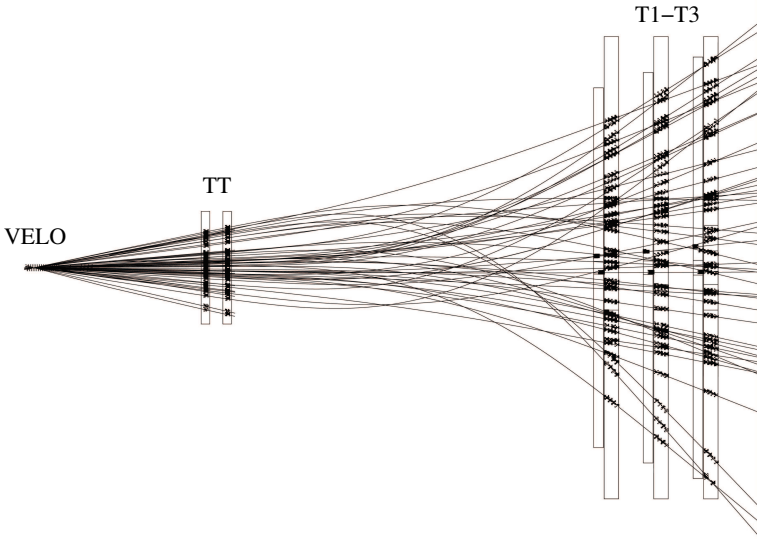

Figure 2.4: *Display of the reconstructed tracks and assigned hits in an event using the vertex locator and the tracking stations. This particular event contains 50% more hits than average.*

2.2 Charged Track Reconstruction

In LHCb, charged particle trajectories, shown in Figure 2.4, are reconstructed by the Vertex detector placed at the interaction point and by the Tracking stations. The magnet provides bending power for charged particles to allow for particle momentum measurements.

2.2.1 Dipole Magnet

The warm dipole magnet [39] of the LHCb experiment provides a bending power of 4 Tm for tracks originating from the primary interaction point. The design is of two trapezoidal coils bent at 45 degrees. The coils are made of 15 individual aluminium "pancakes" stacked together. The generated field is then shaped and guided by an iron yoke on which the coils are mounted.

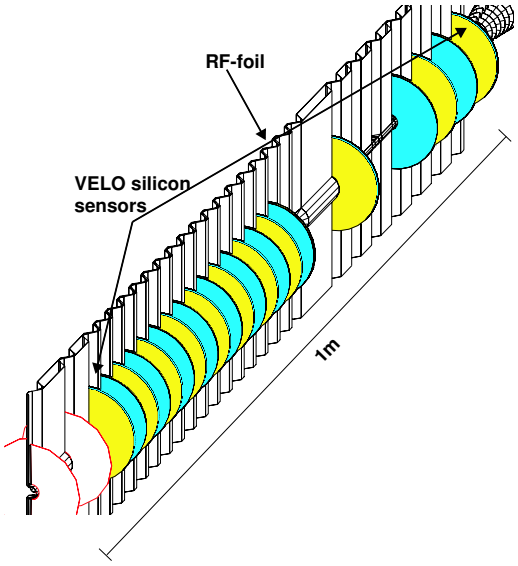

Figure 2.5: *Silicon sensors layout with the RF foil along the beam axis.*

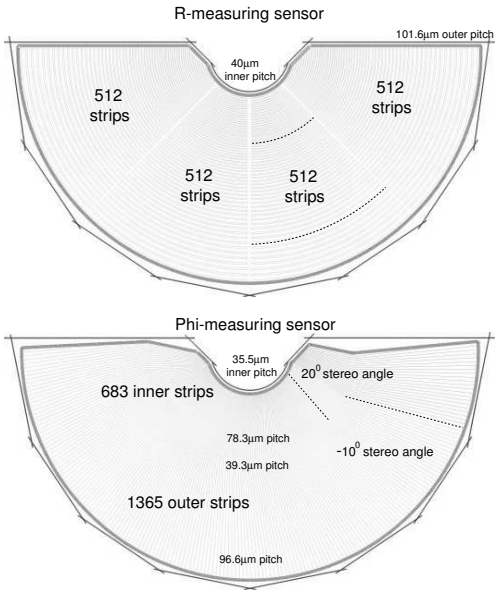

Figure 2.6: *Sensors strip layout with some strips illustrated in dotted lines.*

2.2.2 The Vertex Locator Detector

The VErtex LOcator detector (VELO) [41] provides measurements in the vicinity of the interaction point. The main tasks are to reconstruct the trajectories of charged tracks coming from primary vertices and the reconstruction of secondary b-hadron decay vertices.

The VELO, shown in Figure 2.5, is made out of stations consisting of two half modules: the left and the right half modules are separated during of the filling of the beam. Each of the 21 circular stations is made of 2×2 half-circles of 300 μm thin silicon micro-strips to register the hits of the charged tracks passing through. Put all together they allow for track identification in the angular range of 15 mrad to 390 mrad. Each station shown in Figure 2.6 consists of one R and one Phi measuring sensor of radius 34 mm. The strip pattern on the R-sensor has a constant radius separation with 512 strips ordered into four sectors of approximately 45°. The Phi-sensor has straight strips with an inner zone at a 20° stereo angle while the outer zone as a stereo angle of 10°. In addition, two R-measuring sensors are placed upstream of the VELO to act as a pile-up veto. They select beam crossings with only one pp-interaction by reconstructing the z-position of the interactions to determine the number of primary interactions within one bunch crossing. For an average event, the resolution on the primary vertex in the z-direction is 42 μm and 10 μm perpendicular to the beam. The precision on the decay length ranges from 220 μm

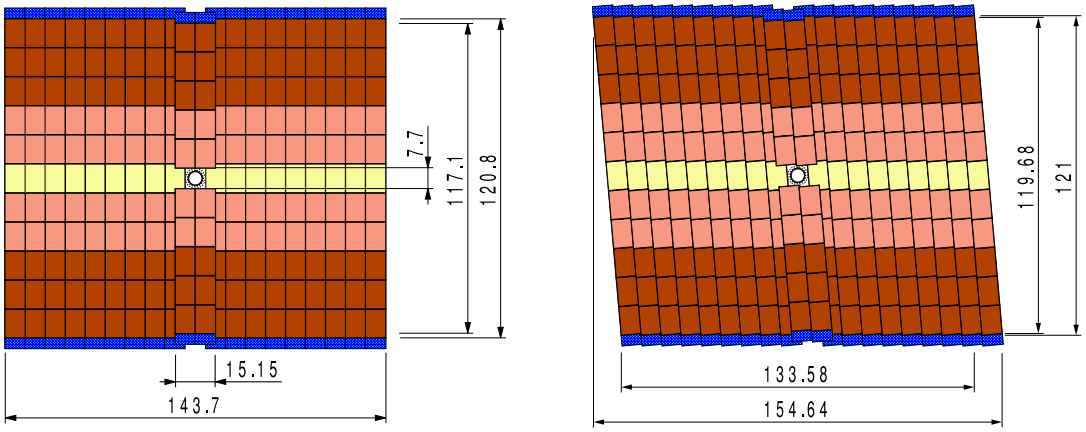

Figure 2.7: *The x-layer (left) and one stereo layer (right) in TT. Units are in cm.*

to 370 μm depending on the decay channel which corresponds to a lifetime resolution of 40 fs for a typical B-meson decay.

2.2.3 Tracking Stations

The tracking stations provide measurements of track coordinates for momentum determination in the horizontal bending plane of the magnet and sufficient resolution for pattern recognition in the vertical coordinate. The system consists of four planar tracking stations grouped as a Trigger Tracker station (TT) in front of the dipole magnet and three Tracking stations (T1-T3) placed downstream.

Trigger Tracker

The role of the Trigger Tracker is to determine transverse momentum parameters of charged tracks and to reconstruct long lived neutral particle trajectories decaying downstream of the VELO. TT may also reconstruct low-momentum particles bent out of the acceptance of the experiment before reaching tracking stations T1-T3, further downstream. The entire TT will be equipped with silicon micro-strip detectors [42] with a strip pitch of 198 μm and strip lengths of up to 33 cm. Each sensor is 11 cm long and 7.8 cm wide. The total surface area of TT is 8.3 m^2. There are four detection layers of the two types illustrated in Figure 2.7. The first and the fourth layer have vertical readout strip (x-layers) whilst the second and the third have strips rotated by a stereo angle of +5° and -5°, respectively (u and v layers) in order to measure the y-coordinate and minimise ghost tracks. The layers are grouped in pairs with the two groups 30 cm apart.

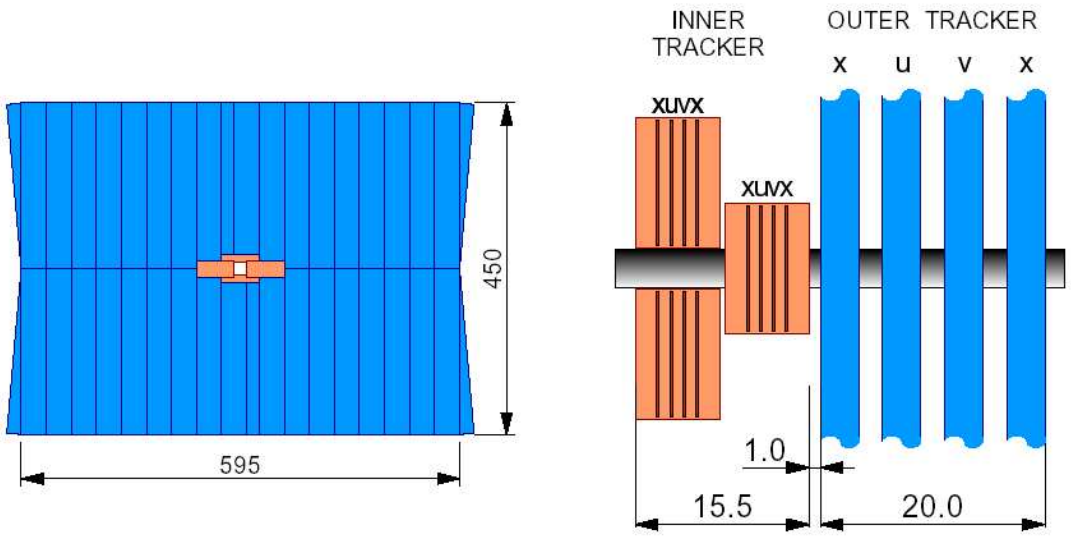

Figure 2.8: *Front view (left) and top view (right) of one Tracking station. Dimensions are given in cm.*

Tracking Stations

The three tracking stations T1, T2 and T3 are equidistantly positioned along the beam pipe between the downstream face of the LHCb magnet and the entrance window of RICH2. Each tracking station consists of four detection layers with the same "xuvx" topology as the TT stations. The stations shown in Figure 2.8, are divided into two trackers.

Most of the acceptance of the tracking stations is covered by the Outer Tracker [43] straw drift-tube modules. Each module is 34 cm wide and contains two layers of straw tubes inside a gas tight box filled with a drift gas mixture $Ar(75\%)$ $CF_4(15\%)$ $CO_2(10\%)$. A standard module is made of 64 straws per layer while smaller modules of 32 tubes are placed where the track density is small above and below the Inner Tracker acceptance.

In contrast, the Inner tracker [42] covers only 1.3% of the sensitive area but approximately 20% of all charged particles go through that region. Each Inner Tracker station is made of four "xuvx" layers equipped with silicon detectors as for TT of which two layers are illustrated in Figure 2.9. The sensitive elements of the four layers overlap with each other and with adjacent Outer Tracker modules in both horizontal and vertical direction, as shown is in Figure 2.8.

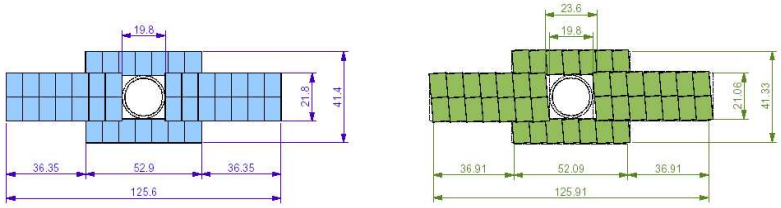

Figure 2.9: *Layout of the x-layer (left) and the stereo layer (right) in T2. Dimensions are given in cm and refer to the sensitive surface covered by the Inner Tracker.*

2.2.4 Performance

Hits from the VELO and the tracking stations are combined to form the particle trajectories for all particles. Identified tracks are represented by state vectors of the x and y coordinates to the reference z, dx/dz and dy/dz the track slope in the corresponding plane and Q/p the inverse particle momentum, which is positive or negative depending on the charge. Several classes of tracks are defined according to the number of detectors they pass through. In the case of B-meson decays the long tracks, i.e. tracks traversing the full tracking setup, are the most relevant. The B-field of the magnet has been optimised to achieve a momentum resolution of 0.6 % for long tracks [47]. The efficiency in finding a correct hit and hence reconstruct a track is of the order of 94 % for large multiplicity decays such as $B \to J/\psi K^0_s$. The efficiency is over 98 % for the pions from the $B \to \pi\pi$ decay.

2.3 Particle Identification

Particle identification is performed by the following three detector systems:

- The Ring Imaging Cherenkov Detectors (RICH) are mainly used to separate charged particles, especially kaons and pions. The RICH will be described in more detail in Chapter 3.
- The Calorimeters identify high transverse energy particles: electrons, neutral particles (photons), π_0 or hadrons.
- Muon chambers are used for muons identification.

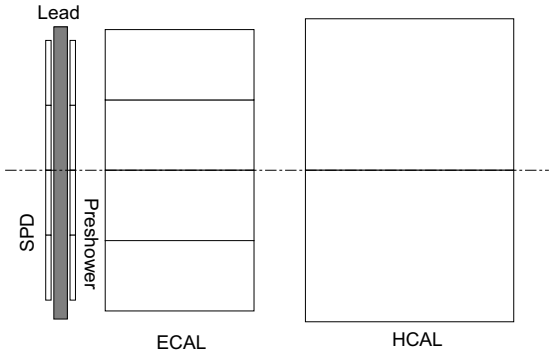

Figure 2.10: *Schematic side view of the Calorimeter system.*

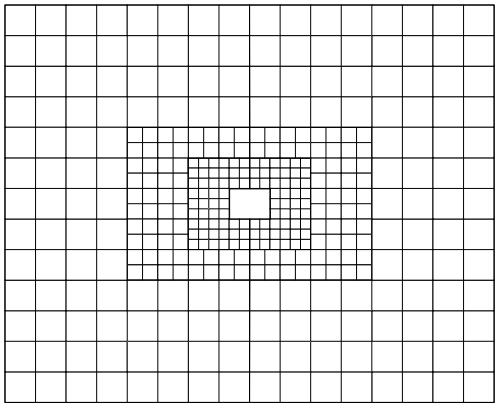

Figure 2.11: *Cells layout of the SPD, PD and the ECAL detectors. Each square represents 16 cells.*

2.3.1 Calorimeters

The calorimeters are destructive detectors which identify particles by absorbing their energies and momenta in active and passive detector elements. The LHCb calorimeters are made of four detectors as shown in Figure 2.10. They provide high transverse energy, E_t, particle identification at the early L0 trigger level when the RICH information is not yet available.

The Scintillator Pad Detector (SPD) identifies charged particles by means of 15 mm-thick scintillator tiles which allow to separate photons from electrons. The light produced by a ionising particle traversing the tiles is collected by Wavelength Shifting fibres (WLS) [43]. The re-emitted green light is guided outside the detector acceptance towards 16 channel Multianode PhotoMultiplier Tubes (MaPMT) via clear plastic fibres.

The SPD is followed by the Preshower detector (PD) and consists of a 12 mm-thick lead plane placed in front of a 15mm-thick scintillator plane. The lead plates allow electrons to interact and hence produce an extra shower before reaching the scintillator plates. As a result they have a larger energy deposit than pions hence improving the separation.

The Electromagnetic CALorimeter (ECAL) then measures the energy of the electromagnetic showers from photons and electrons. The shower's energy is sampled by detector elements with a geometry shown in Figure 2.11. The ECAL is structured to respond to the different track density areas with three cell sections of decreasing resolution. The cells

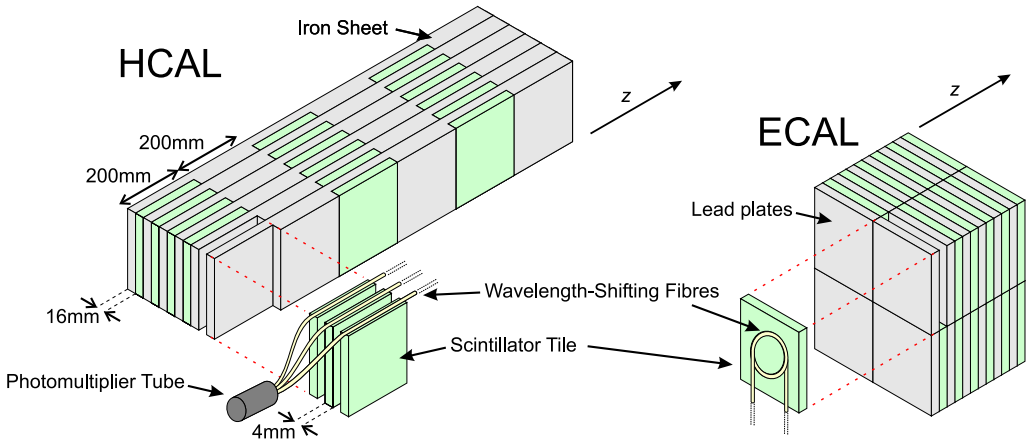

Figure 2.12: *Schematic layout of the scintillator tiles and absorbers of the HCAL (left) and ECAL (right) [36].*

size are 4×4 cm in the central region, 6×6 cm in the middle region and 12×12 cm in the outer region with a total of 5984 cells. The cells, shown in Figure 2.12, are alternating planes of 4 mm-thick lead sheets as absorbing material, and 2 mm-thick scintillator tiles which sample the particle showers. The shower energy resolution is $10\%\sqrt{E}\,\text{GeV}\oplus 1.5\%$.

The Hadron CAlorimeter (HCAL) samples the remaining hadrons with 16 mm iron sheet interspaced with 4 mm scintillator tiles as illustrated in Figure 2.12. The 1468 cells are spread in a way that the HCAL cell boundaries project to the ECAL cell boundaries. There are only two regions with 13×13 cm and 26×26 cm cell sizes for an energy resolution of $80\%\sqrt{E}\,\text{GeV}\oplus 10\%$.

2.3.2 Muon Chambers

Muons are present in many CP-sensitive B-meson decays and rare decays with new physics potential. Triggering on muons and their efficient identification is hence a fundamental requirement for LHCb.

The muon system [44], shown in Figure 2.3, consists of five tracking stations M1 to M5 which rely on the penetrative power of muons. The first station M1 is dedicated to the transverse-momentum (p_t) measurement of the muon track used for the muon triggering. It combines a 20% resolution for the p_t measurement with a stand-alone muon track reconstruction. The remaining four stations are interspersed with an iron shield to attenuate

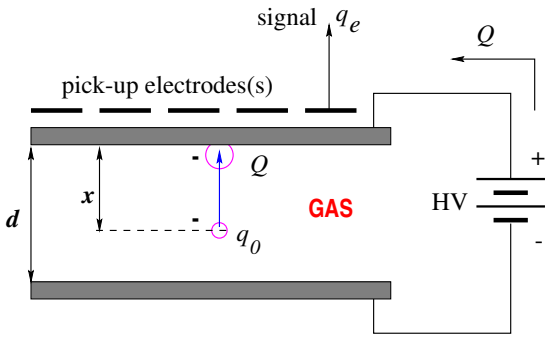

Figure 2.13: *Schematic diagram of a Resistive Plate Chamber showing the signal induced by a q_0 charge in the $C_2H_2F_4$ / C_4H_10/SF_6 (95:4:1) gas.*

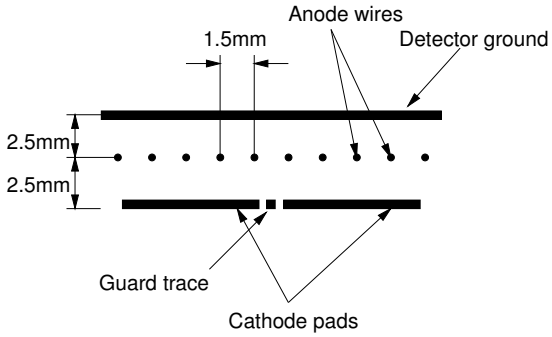

Figure 2.14: *Schematic diagram of one sensitive gap filled with $Ar/CO_2/CF_4$ (40:50:10) in a Multi Wire Proportional Chamber. Each chamber is made of four gaps connected in pairs.*

background contribution from hadrons, electrons and photons. The electromagnetic and hadronic calorimeters and three iron filters give a total absorber thickness of 20 nuclear interaction-lengths for a total detector area of 435 m^2.

Just like the calorimeter system, the detector responds to the large variation of particle flux by subdividing each station into four regions with different pad dimensions. Regions and pad sizes are scaled by a factor two from one region to the next starting at 250×300 mm, for Region1. Two types of technology are used in order to cope with the varying occupancy: Resistive Plate Chambers (RPC) and Multi-Wire Proportional Chambers (MWPC). Their principle of operation are shown in Figures 2.13 and 2.14, respectively. MWPCs are mostly used for the outer regions while centre regions use RPCs except in M2 and M3 where a mixed MWPC and RPC readouts is used.

The muons reconstruction efficiency has been estimated for a sample of $B_d^0 \to J/\psi K_s$ and is on average 94.3% above 10 GeV/c with a pion mis-identification rate of 2.9%. This pion mis-identification can be reduced by taking into account the RICH and the Calorimeters systems data.

	L0	L1	HLT	Offline
Data rates	40 MHz	1 MHz	40 KHz	200 Hz
Subdetectors used	VELO, ECAL, HCAL, MUON	All but RICH and T1-T3	All but RICH	All
CPU usage (out of 1800 nodes)	On detector	20%	55%	25% +GRID

Table 2.1: *Data rates, CPU usage and subdetectors used for the different trigger levels.*

2.4 Triggers

The LHCb experiment will operate at an average luminosity of $2\times10^{32}\,\mathrm{cm}^{-2}\mathrm{s}^{-1}$. With this choice single interactions dominate which eases the event selection and reconstruction. Of the beam crossing rate of 40 MHz, only 10 MHz produce visible interactions, i.e. interactions producing at least two charged particles with sufficient hits in the VELO and T1-T3 stations to allow for reconstruction. The role of the Trigger system is to select the interesting events and lower the rate down to manageable computing and storage capabilities. To do so the trigger is designed around three levels distinguishing minimum bias events from events containing B-mesons by requiring the presence of particles with large transverse momentum and the existence of secondary vertices.

The first level trigger (Level-0) uses the Pile Up Veto to suppress multiple interactions. Events are selected based on the reconstruction of the highest transverse energy hadron, electron and photons in the calorimeters together with the two highest p_t muons from the muon trigger M1. Implemented as fast on-detector electronics it lowers the data rate from 40 MHz to 1 MHz.

The second level trigger (Level-1) reconstructs tracks in the VELO and matches them to Level-0 muons or calorimeters clusters. It is then able to identify the tracks and measure their momenta. Momenta are also deduced from the known magnetic field and the track bending between the VELO and the TT stations. Particle momenta can be determined with a resolution of 20-40%. Data from the tracking stations T1-T3 and the muons stations M2-M5 are not used at this stage but the system has been designed to be scalable in order to later improve the performances. Level-1 reduces the data rate to 40 kHz which allows for the execution of more elaborate selection algorithms.

The third and final level trigger is called the High Level Trigger (HLT) and makes use of

the all subdetectors information. The lower input rate allows it to refine the parameters obtained from Level-1 to higher precision. Additional momentum information can then be gained from the tracks reconstructed from the VELO to the T1-T3 stations. The HLT finally applies selection cuts dedicated to specific final states. Bandwidth limits are then imposed according to the physics goals. The selected events are then written on disk at a rate of 200 Hz where an offline analysis can be applied. A summary of the trigger system and its performances is given in Table 2.4.

Chapter 3

The LHCb RICH Detector

As mentioned in Chapter 1, Section 1.4.4 CP violation measurements require excellent charged pion/kaon separation to efficiently identify the final state particles in B-meson decays. The LHCb experiment will use two Ring Imaging Cherenkov detectors (RICH1 and RICH2) for charged particle identification across the full angular acceptance of the detector.

3.1 Principle of the RICH Detectors

RICH detectors are based on the Cherenkov effect which was first observed by Pierre and Marie Curie in the early 1900's in their work on radioactivity. This phenomenon was only fully explained in 1937 by P.A Cherenkov, I.M Frank and I.Y Tamm who earned the Nobel Price for their work in 1958. They established that a charged particle travelling in a medium in which its velocity is greater than the speed of light, c, emits light along its path. A common analogy is that of a plane breaking the sound barrier causing a shock wave. The particle breaking the light speed emits a "light wave" as a cone of light around its trajectory. The size of the angle of emission called Cherencov angle, θ_c, is related to the velocity of the particle $v_p = \beta c$ through:

$$cos\theta_c = \frac{1}{\beta n} \tag{3.1}$$

where n is the refractive index of the medium. The threshold velocity above which Cherenkov light is emitted is $\beta_t = 1/n$. The first proposal to make use of this process

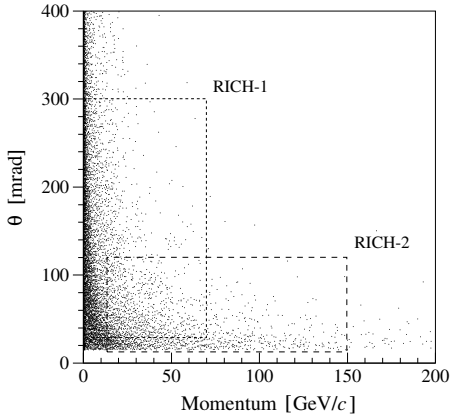

Figure 3.1: *Polar angle distribution as a function of momentum for all tracks in simulated* $B_d^0 \to \pi^+\pi^-$ *decays.*

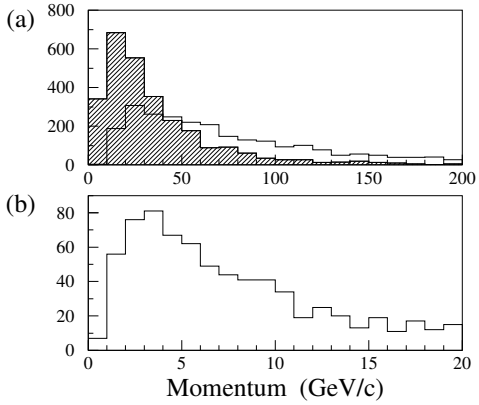

Figure 3.2: *Momentum distribution for (a) the highest momentum pion from* $B_d^0 \to \pi^+\pi^-$ *(unshaded) and* $B_s^0 \to D_s^-\pi^+\ \pi^-\pi^-$ *(shaded), (b) tagging kaons.*

for Ring Imaging detectors for particle identification was made in 1977 by Tom Ypsilantis and Jacques Seguinot [28]. RICH counters consist of one or several radiators containing a medium chosen for an appropriate Cherenkov light emission threshold. A set of mirrors focus the light into ring images in the focal plane where photodetectors collect the photons. Since their invention, the accuracy of RICH detectors keeps increasing as new technologies are put forward, notably in the field of photon detection.

3.2 LHCb RICH Counters

The LHCb RICH counters [40] have been designed to cover the momentum range $1 < p < 100\,\mathrm{GeV/c}$. This requirement has led to a system of two RICH detectors using three radiators. Figure 3.1 shows how the two RICHs cover the phase space. Figure 3.2 shows the momentum distribution of particle decays used to establish the limits of coverage. The upper limit in momentum has been chosen using the momentum distribution of the two body decay $B_d^0 \to \pi^+\pi^-$ as shown in Figure 3.2(a) where a cut at $100\,\mathrm{GeV/c}$ can be applied. The lower momentum limit was taken for slower tracks with high multiplicity such as $B_s^0 \to D_s^-\pi^+\pi^-\pi^-$. Figure 3.2(b) shows that there is no significant loss in tagging by requiring a lower bound at 1 GeV/c.

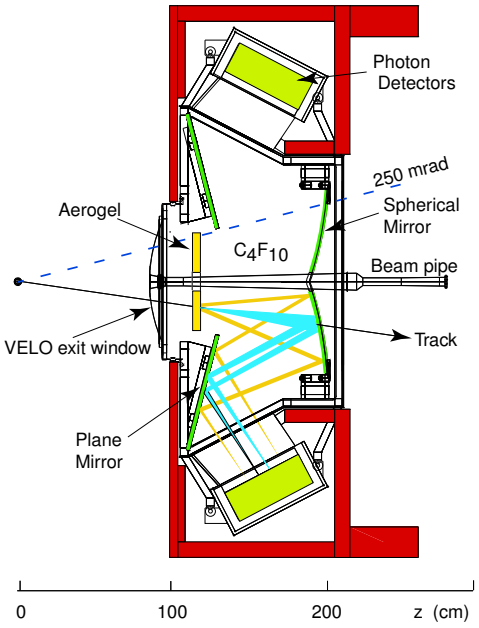

Figure 3.3: *Side view of RICH1 detector.*

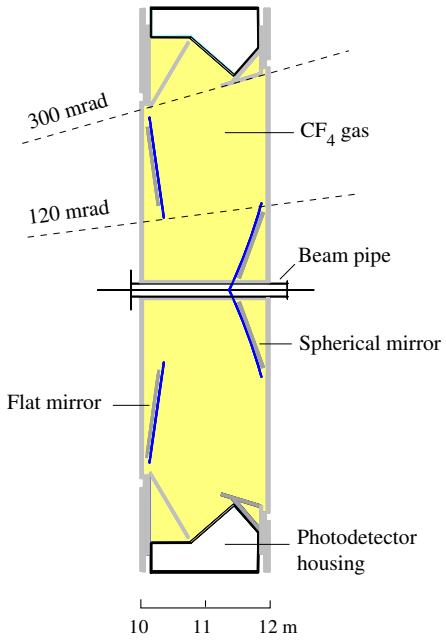

Figure 3.4: *Top view of RICH2 detector.*

3.2.1 RICH1 Detector

The RICH1 detector, shown in Figure 3.3, has been designed for low momentum tracks with large scattering angle requiring full angular coverage of the acceptance. The structure is therefore placed close to the interaction point to minimise the surface area. As a result, the RICH1 vessel has dimensions of $2\times3\times1\,\mathrm{m}^3$. RICH1 covers the momentum range 1-60 GeV/c using two radiators. A 5 cm thick aerogel radiator with refractive index 1.03 identifies kaons above 2 GeV/c and provides a π-K separation up to 10 GeV/c. A second larger gaseous radiator of 85 cm contains C_4F_{10} with refractive index 1.0014 and extends the π-K separation up to 60 GeV/c. The Cherenkov photons are focused by spherical mirrors with a radius of curvature of 240 cm and are then reflected by plane mirrors towards the photodetectors. Table 3.1 shows the Cherenkov angle for electron tracks which have $\beta = 1$ together with the expected number of photons and the momentum thresholds of the pions and kaons. Quartz windows of dimensions $130\times60\times0.5$ cm seal the top and the bottom of the vessel and transmit the Cherenkov light to the photodetectors.

	Aerogel	C_4F_{10}	CF_4
Refractive index	1.03	1.004	1.0005
θ_c (mrad)	242	53	32
N_γ	6.6	32.7	18.4
π_{th} (GeV/c)	0.6	2.6	4.4
K_{th} (GeV/c)	2.0	9.3	15.6

Table 3.1: *Radiator properties: θ_c is the Cherenkov angle for electrons, π_{th} and K_{th} are the momentum thresholds for pions and kaons, respectively. N_γ is the total number of photons for the Cherenkov ring produced by electron tracks.*

The RICH1 detector underwent big design changes as part of a re-optimisation of the LHCb experiment [18]. The main goals were: (1) to decrease the amount of secondary emitted particles by reducing the amount of material seen by the primary particles, (2) to improve the performance of the trigger. As a result the RICH1 detector will now be exposed to the fringe field of the magnet to improve track separation at the trigger level. New light materials have been tested to reduce the radiation length of the mirrors. The mirrors will now be made of 2 mm thick beryllium. There will be four mirror segments of size $820\times614\,\mathrm{mm}^2$ each. The magnetic shielding needed to be strongly re-enforced to provide sufficient protection for the photodetectors while at the same time drive enough magnetic field towards the Trigger Tracker for a maximum particle separation [45]. The task is rendered more complicated due to the small space available. The soft iron shield housing allows to reduce a 600 G magnetic field at the photodetector plane down to 25 G while at the same time keep the 134 kGm integral field required for the tracks reaching the trigger tracker [46].

3.2.2 RICH2 Detector

The RICH2 detector, shown in Figure 3.4, identifies high momentum particles with an outer acceptance of 120 mrad (100 mrad) in the horizontal (vertical) plane. It is placed further down-stream to allow for better separation of low angle tracks. There is a single 167 cm long radiator filled with gaseous CF_4 of refractive index 1.0005. Just as in RICH1, the Cherenkov photons are focused with spherical mirrors and deflected onto the photodetectors with flat mirrors. The focusing mirrors are made of 42 hexagonal segments and 14

half-hexagonal segments of size 520 mm across the diagonal and a radius of curvature of 860 cm. The plane mirrors are made of 40 rectangles of size $410\times380\,\mathrm{mm}^2$ with a 6 mm thick glass substrate. Unlike in RICH1 where the photodetectors are mounted vertically, over and under the structure, the photodetectors of RICH2 are placed horizontally on the left and the right, outside the acceptance of the spectrometer. While RICH1 is subject to high magnetic field constraints due to the vicinity of the magnet the RICH2 detector only sees 140 G. The soft iron housing designed can easily absorb the field. Thus the magnetic field at the plane of the photodetectors was not a concern for RICH2.

3.3 Particle Identification

The aim of the pattern recognition [17] is to assign a particle candidate to each track. As the focusing mirror has to be tilted the rings on the RICH detector planes are no longer perfect circles but elliptical. An example of fitted rings is given in Figure 3.5. The Cherenkov angles (ϕ_c, θ_c) defined in Figure 3.6 are directly reconstructed at the emission of each hit instead of a direct fit of the ring. In that method track information from other trackers is hence essential. All hits with similar emission angle are attributed to one track. There are two methods: 1) The standard "local" method which considers each track separately. The main advantage is its speed but it does not provide information about the background.

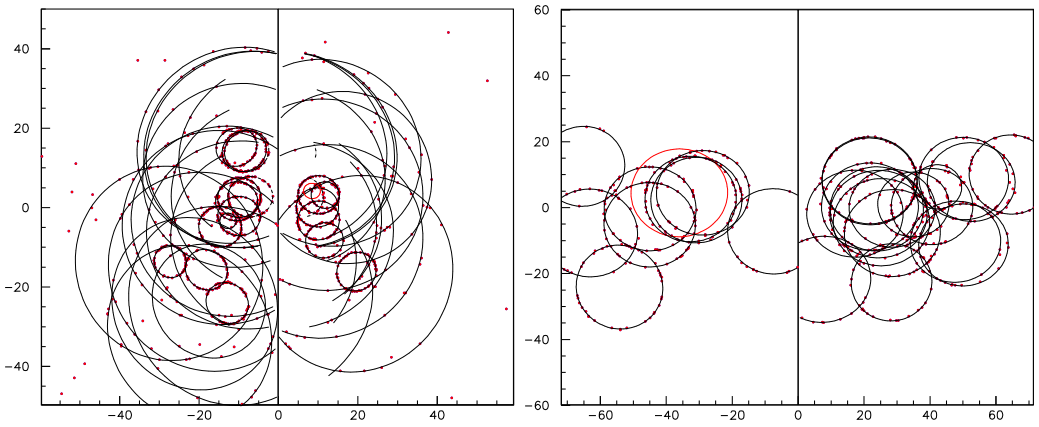

Figure 3.5: *Event display of $B_d^0 \to \pi^+\pi^-$, with the photodetector planes of each RICH drawn side by side (scale in cm). The fitted Cherenkov rings from the global method are superimposed. RICH1 is on the left and RICH2 is on the right.*

2) The "global method" is five times slower because it treats all hits and all tracks at the same time permitting the determination of background information. Table 3.2 compares the particle tracks that one would expect from the five usual charged particles (e, μ, π, K, p) under the form of a maximum likelihood. The total number of possible combinations for N tracks in an event is 5^N. A typical event consists of about 30 tracks and it hence quickly becomes a Gargantuan task. The number of combinations can be greatly reduced by first assuming that all tracks are pions as they are the most numerous. The log-likelihood for that set of particle mass-hypothesis is then recalculated for e, μ, K and p in turns. The procedure is then re-iterated changing hypothesis for all tracks to find the largest increase in likelihood. This way the number of determinations is reduced to $2N^2$.

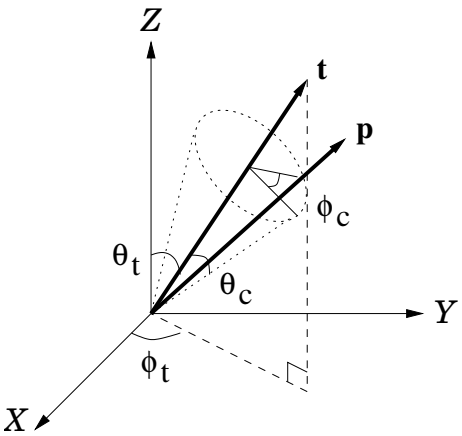

Figure 3.6: *Definitions of the angles describing the direction of the track* ***t*** *and the photon* ***p*** *emitted by the track.*

The nominal pixel size (granularity) for photodetectors has been estimated to $2\times2\,\mathrm{mm}^2$. A granularity of 2.5 mm has however revealed no significant loss in performance and it hence has been adopted as baseline criteria for the photodetector resolution.

	True particle type						
Rec	e	μ	π	K	p	X	$\mathcal{P}$
e	97.4	0.7	24.6	1.4	0.5	3.1	0.76
μ	4.0	8.7	69.5	2.0	0.5	4.9	0.10
π	2.5	1.3	545.7	3.3	0.7	5.1	0.98
K	0.3	0.1	12.7	70.6	4.8	4.3	0.76
p	0.2	0.0	1.7	4.3	35.9	0.0	0.85
X	9.9	0.8	19.8	3.2	0.0	55.6	0.62
ε	0.85	0.76	0.81	0.83	0.85	0.76	

Table 3.2: *Each track gives one entry in the table, and X denotes tracks below threshold in all radiators; the rows give the reconstructed particle type, $\mathcal{P}$ is the purity and ε the efficiency. The sample corresponds to 500 tracks, but has been renormalised to 1000.*

3.4 Photodetectors

The requirements for the photodetectors of the LHCb RICH are:

- single photon electron sensitivity with high quantum efficiency for visible light as imposed by the aerogel radiator. The photodetector should be sensitive in the wavelength range of 200 nm to 600 nm.
- a pixel size of $2.5 \times 2.5\,\mathrm{mm}^2$.
- fast read out compatible with the 25 ns bunch crossing period of the LHC.
- low electronic noise.
- suitability for large area coverage of about $1.2\,\mathrm{m}^2$ ($2.6\,\mathrm{m}^2$) for RICH1 (RICH2) with an active area larger than 73%.
- capacity to withstand 2.5 mT with or without individual shielding.
- radiation hardness to a dosage of 3 krad/year.
- affordable cost.

At the time of the LHCb conceptual design no commercially available photodetector could meet these requirements. A large program of R&D was thus launched on two options. The development of Hybrid PhotoDetector tubes (HPD) as baseline and the use of Multianode PhotoMultiplier Tubes (MaPMT) as backup solution.

3.4.1 Hybrid Photodetectors

The pixel Hybrid PhotoDetector (HPD) shown in Figure 3.7 uses a silicon detector anode inside a vacuum envelope. It was designed in collaboration with DEP[1]. The HPD design is Based on an image intensifier technology using a cross-focusing electric field to accelerate and image the photoelectrons emitted from a S20 photocathode onto the anode. The HPD has a diameter of 83 mm with a photocathode active input diameter of 75 mm. The demagnification factor, shown in the schematic of Figure 3.7 (right), is five. A high voltage

[1] Delft Electronic Products, Roden - Netherlands.

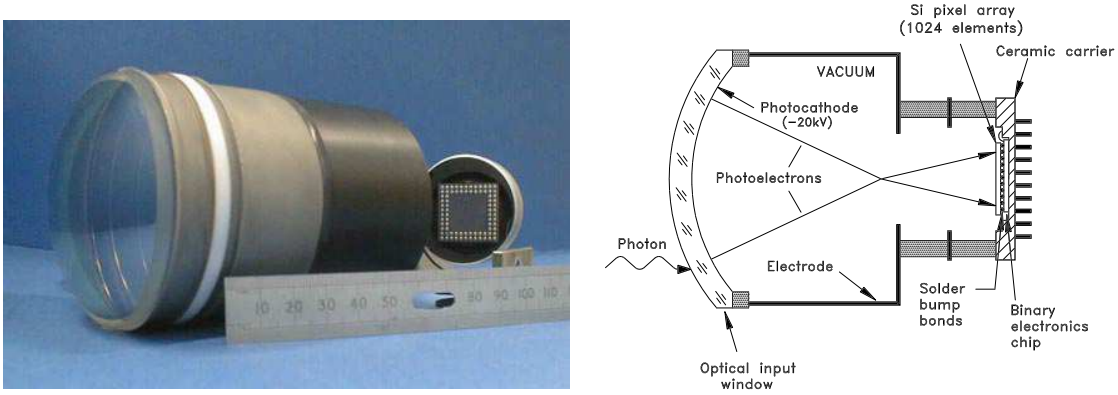

Figure 3.7: *Left: A photograph of the baseline photodetector HPD with the read-out silicon chip visible on the back. Right: A schematic of the pixel HPD illustrating the photoelectrons trajectories.*

of 20 kV is applied to accelerate the photoelectrons resulting in a signal of about 5000 e^- at the silicon chip. The quantum efficiency is 25% at 300 nm. The anode consists of a 32×32 array of silicon pixels of size 0.5×0.5 mm^2. Each pixel is segmented into eight subpixels of size 0.0625×0.5 mm^2 in order to reduce the noise originating from the sensor. The feasibility of using these detectors has been studied in a testbeam with a prototype reproducing the RICH1 geometry. The beam consisted of pions with a momentum of 120 GeV/c. Figure 3.8 shows the Cherenkov ring obtained using three HPDs prototypes with a coarser pixelisation (61 pixel HPD) [33] [34].

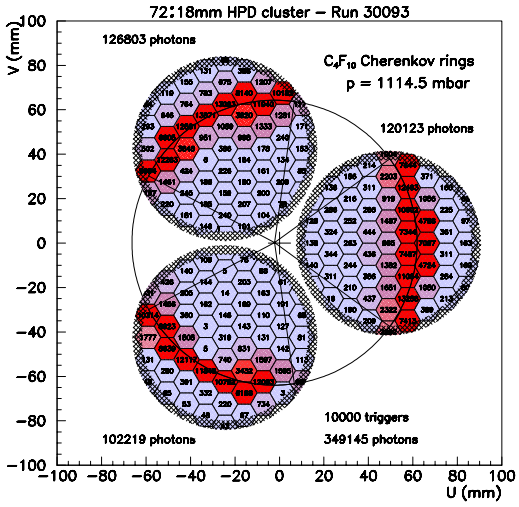

Figure 3.8: *Display of events in a RICH1 testbeam setup with a C_4F_{10} gas radiator. The shade of a pixel gets darker with the number of hits on the pixel. A fitted ring is drawn.*

A main concern for the HPDs is its sensitivity to magnetic fields [35]. Photoelectrons travel for a long distance before reaching the anode and hence HPDs are potentially more sensitive to magnetic fields than conventional photodetectors. Figure 3.9 shows the distortion of a signal when the tube is subjected to magnetic fields. The light source pattern on the sensor chip changes as the HPD undergoes magnetic fields of 0, 0.5 and 1 mT in strengths. When a longitudinal field is applied, Figure 3.9 (left), the image rotates and stretches. At 1 mT photoelectrons start falling outside the anode sensitive area and are lost. Transverse fields, Figure 3.9 (right), cause non-uniform shifts of the image across the anode. HPDs thus have to be shielded against large magnetic fields. It is planned to use a cylindrical μ-metal shield placed around the tube as an individual protection together with a global shield of the photodetector plane. The individual shield will be a 200 mm long, 0.9 mm thick cylinder and will protrude 20 mm beyond the front of the HPD entrance window. The shield provides adequate protection up to 3 mT. A static distortion pattern will nonetheless remain. An inside survey will be performed to provide a calibration which will be applied at the reconstruction level.

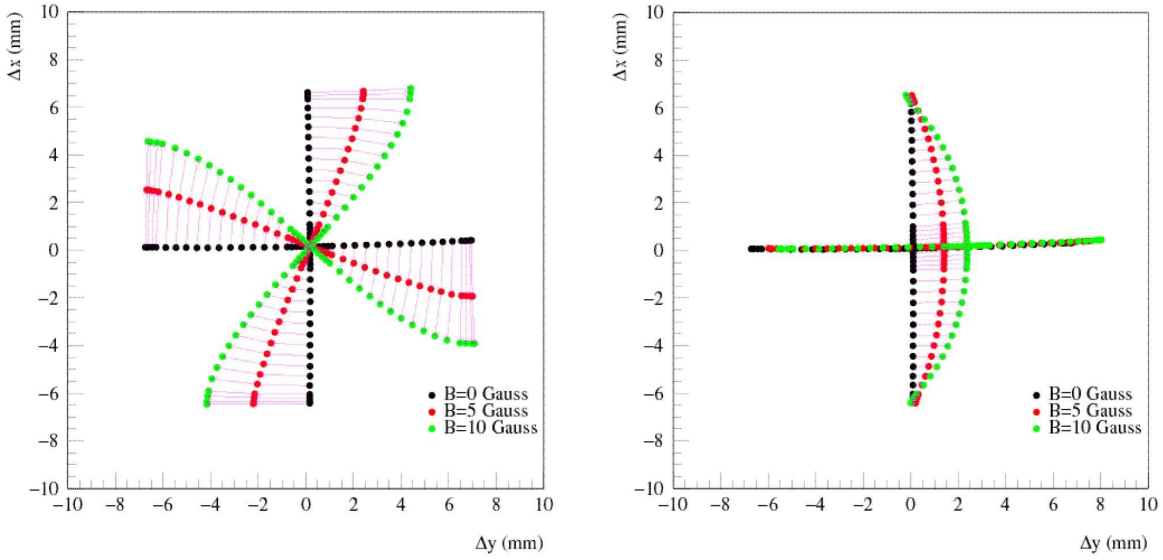

Figure 3.9: *Cross shape image distortions of the HPD signal when exposed to magnetic fields of 0.1, 0.5 and 1 mT, for a longitudinal field, defined as the axis perpendicular to the photocathode (left) and a transverse field (right) [36].*

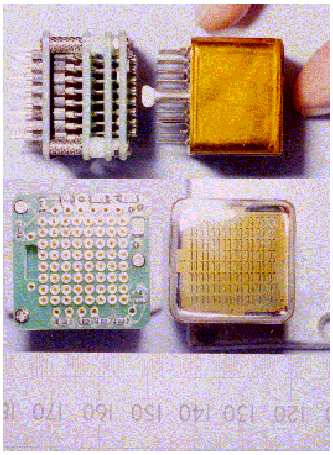

Figure 3.10: *Side view (top) and top view (bottom) of an MaPMT with its carrier.*

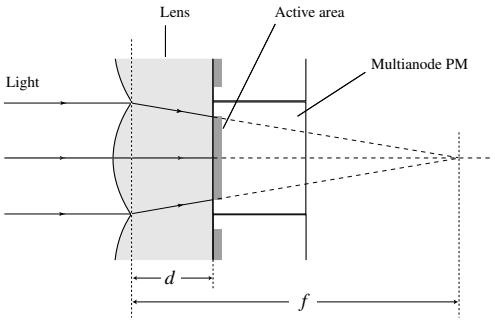

Figure 3.11: *Diagram illustrating an MaPMT mounted with a lens.*

3.4.2 Multianode Photomultiplier Tubes as Back Up Solution

Multianode PhotoMultiplier Tubes (MaPMT) consist of an array of square anodes close-packed in a single vacuum tube of size $25\times25\times20\,\mathrm{mm}^3$. While HPDs had still to be developed at the early stages of the LHCb design, MaPMTs have been successfully used by the HERA-B collaboration at DESY[2] for their RICH detector [19]. It hence was a logical backup option for LHCb detector.

The HERA-B detector used 4×4 channel tubes with a 4 mm cell granularity. This is not suitable for the LHCb experiment which needs the higher pixel resolution of $\sim 2\times2$ mm for RICH1. However, meanwhile the manufacturer Hamamatsu (Japan) had developed a 8×8 anode array with a 2×2 mm cell granularity. A photograph of the MaPMT is shown in Figure 3.10. The R7600-03-M64 model was originally equipped with a borosilicate window. On request of LHCb, Hamamatsu mounted a UV glass window instead. This improvement leads to an increase of 50 % in the number of photoelectrons detected. The pitch of the channels is 2.3 mm with 0.2 mm gaps between the pixels reducing the active area to only 38 %. A quartz lens has thus to be placed in front of the tube as shown in Figure 3.11 to restore a full active area of 85 %. The fused silicia lens has one flat and one spherical surface with a radius of curvature of 25 mm and a demagnification of two-third in order to focus the photons onto the sensitive area of the MaPMT.

[2]Deutsches Elektronen Synchrotron in Hamburg - Germany

An array of 3×3 MaPMTs mounted with lenses has been studied under testbeam conditions. Results were similar to the expected performances from GEANT4 simulations and hence demonstrated the capability of MaPMT to identify Cherenkov rings for the LHCb experiment [20].

Unlike the HPDs, MaPMTs are small close packed devices with an amplification provided by dynode chains and hence the effect of magnetic fields is different. Chapter 5 gives more details on MaPMTs and presents the study establishing their behaviour in magnetic fields.

3.5 RICH Performances

The RICH contribution becomes evident when looking at two-body decays with the same topology. Taking the case of $B_d^0 \to \pi^+\pi^-$ decays, the reconstruction is polluted by other decays such as $B_d^0 \to K^+\pi^-$, $B_s^0 \to K^-\pi^+$ and $B_s^0 \to K^+K^-$. The mass spectrum of the various decays without using the RICH is shown in Figure 3.12 where the $B_d^0 \to \pi^+\pi^-$ decay is barely distinguishable from the $B_d^0 \to \pi K$ decay. The identification from the RICH system as shown in Figure 3.13, provides an obvious gain in purity. The RICH tags the flavour of the b hadron by identifying kaons from the $b \to c \to s$ cascade decays where the charge of the kaon depends on the charge of the initial b quark. It also complements

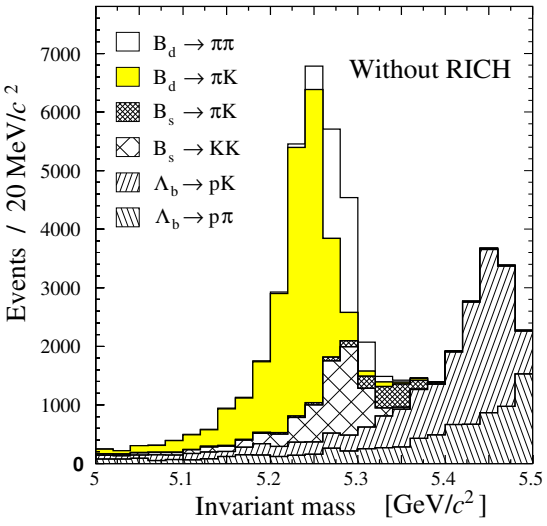

Figure 3.12: *Mass spectrum of* $B_d^0 \to \pi^+\pi^-$ *without RICH selection.*

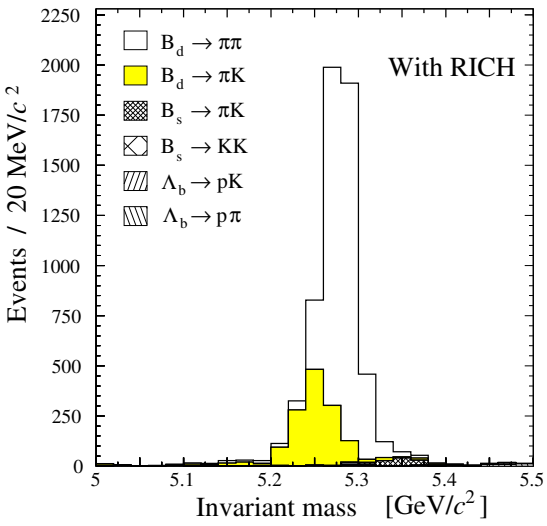

Figure 3.13: *Mass spectrum of* $B_d^0 \to \pi^+\pi^-$ *with RICH selection.*

the calorimeters and the muon chambers in order to reduce the misidentification rate of electrons and muons.

In terms of reconstruction efficiency, Figure 3.14 shows the Kaon identification efficiency $\epsilon(k)$ and the pion mis-identification $\epsilon(\pi \to k)$ for a sample $B_0 \to D_s^- K$. The Cherenkov light thresholds from the three radiators are visible at p=2, 9 and 16 GeV/c. The average $\epsilon(k)$ taken between 2 and 100 GeV/c is 88 % whilst the $\epsilon(\pi \to k)$ is 3 %. The remainder is made of protons, leptons and ghosts.

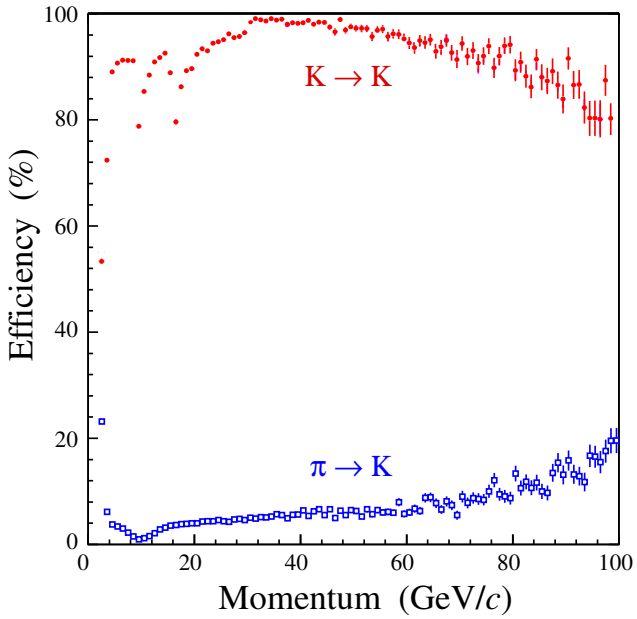

Figure 3.14: *Kaon identification efficiency (solid points) and pion misidentification rate (open points) as a function of momentum for a sample* $B_d^0 \to D_s^- K^+$.

Chapter 4

Photomultipliers

A typical photomultiplier tube, shown in Figure 4.1, consists of a photocathode where incoming photons are converted into electrons via the photoelectric effect. The photoelectrons are then focused and accelerated using electrodes. Secondary electrons are produced when the electrons hit the surface of a dynode. The amplification is performed by the mean of a cascading chain. The charge is finally collected by an anode at the end of the chain.

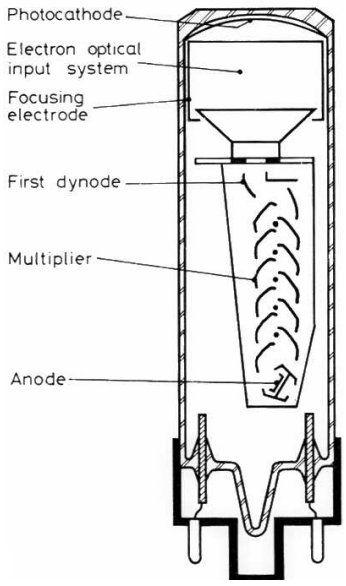

Figure 4.1: *Structure of a photomultiplier: model 56AVP, Philips 1956 [30].*

4.1 Photoelectron Emission

The photoelectric effect is a quantum interaction between a photon and a bound atomic electron. As a result of this interaction, the photon is absorbed and an atomic electron is ejected. The ejected electron energy is $E_\alpha - W$ where E_α is the energy of the photon. W is the work function i.e. the energy required to free electrons.

The photoelectric effect was discovered by Heinrich Hertz in 1887 [22]. While trying to demonstrate the existence of electromagnetic waves, he found that a negative electrode exposed to ultraviolet radiation had a better conduction. In 1888, Hallwachs [23] showed that light actually permits the escape of negative electricity (the electron had yet to be discovered) from a negative and neutral plate. It was established in 1889 by Elster and

Geitel [24] that a relation existed between the metal and the light wavelength to which they are photoelectrically sensitive. The problem remained puzzling until the discovery of the electron by J.J Thomson in 1897 [25]. The carrier of the charge had been identified. Finally in 1905, Einstein [26] based on Plank's quantum theory, formulated the theoretical ground work of the photoelectric process.

The first primitive photomultiplier tube was made in 1902 by Austin et al [31]. But the very first phototube, used as the basic structure for current tubes design, was only made in 1939 by Zworykin and Rajchman [27] who developed an electrostatic focusing type. Since then tubes have constantly been improved by research on the photocathode material and on new multiplication techniques to adapt them to the growing needs of experiments and industry.

4.1.1 Physics of the Photocathode

The purpose of the photocathode is to absorb photons and emit electrons via the photoelectric effect. Figure 4.2 shows the typical band structures of metals, semi conductors and insulators from which the electrons are freed into the vacuum.

In the case of metals, the conduction band is filled up to the Fermi level, E_f. The work required to free an electron is just the thermionic work, $W_{th} = E_o - E_f$ where E_o is the vacuum energy level. The additional energy can be provided by a photon with energy $h\nu \geq W_{th}$ called the photoemission threshold W_{ph} or also work function W. For metals W_{th}=W_{ph}. Except for alkali (Li, Na, K, Rb, Cs), metals have a potential barrier greater than 3 eV and photoemission does not occur in response to visible light. Metal cathodes are however not appropriate for photomultipliers. In travelling to the surface the excited electron suffers energy losses due to collisions with the atomic electrons in its path. The probability of reaching the surface with enough energy is greatly reduced because the atomic electrons are essentially free. The ratio of output electrons to incident photons is called Quantum Efficiency (QE), see Section 4.1.2, and in this case it is of the order of 0.1 %. This means that 1000 photons are required on average to produce one photoelectron. There is therefore a limited usable volume of material restricted to a thin layer of the surface. In metals this escape depth is of the order of a few atomic radii.

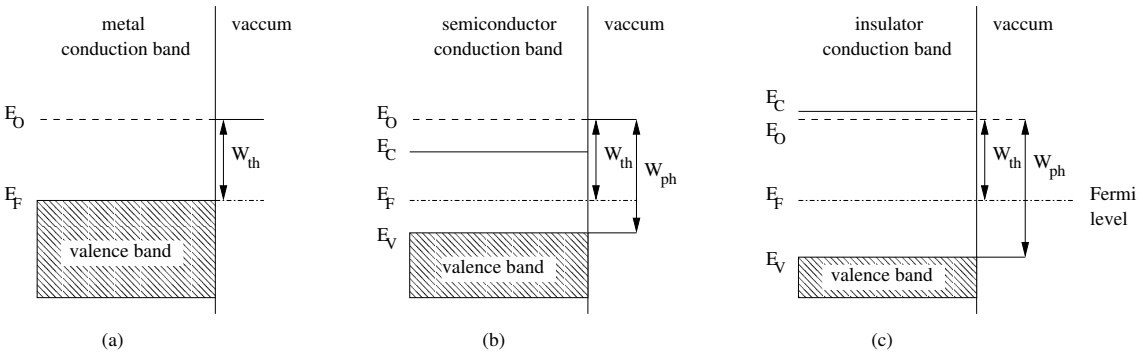

Figure 4.2: *Energy bands in (a) metal, (b) a semiconductor, (c) an insulator [30].*

Semi-conductors and insulators materials, see Figure 4.2 b) and c), differ in that they have a conduction band energy level E_c and a Fermi level lying in the forbidden band. To escape the metal, the electrons must overcome the Energy gap $E_g = E_c - E_v$ where E_v is the valence band energy level, to get to the conduction band and an additional so called electron affinity $E_a = E_o - E_c$. Typical work functions for semiconductors are of the order of 5-6 eV and are thus only sensitive to wavelengths of less than 250 nm. It is however possible to greatly reduce the surface barrier and extend the range of wavelength by doping techniques.

Photocathodes are hence made of a doped opaque or semi-transparent semi-conductor. For opaque photocathodes the photoelectrons are collected from the same surface on which the light is incident. For semi-transparent photocathodes the light first passes trough the transparent substrate layer and then travels in the semi-transparent photocathode so that photoelectrons are collected from the opposite surface.

4.1.2 Quantum Efficiency

The Quantum Efficiency (QE) is a major characteristic of photomultipliers. Defined as the ratio of the number of photoelectrons emitted over the number of incident photons it can also be refined further in a probabilistic manner as follows:

$$QE(\nu) = (1 - R) \cdot \frac{P_\nu}{k} \cdot \left(\frac{1}{1 + \frac{1}{kL}} \right) \cdot P_s \tag{4.1}$$

Where R is the reflection coefficient, k is the full absorption coefficient of photons. P_ν

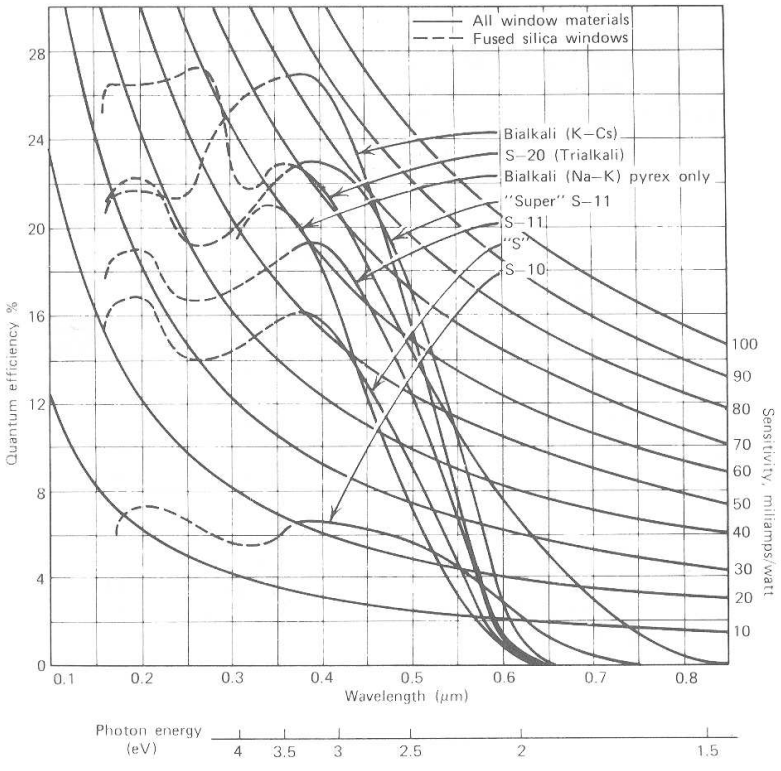

Figure 4.3: *Quantum Efficiency as a function of photon wavelength for different photocathode materials [31].*

is the probability that light absorption may excite electrons to a level greater than the surface barrier, L is the mean escape length of excited electrons, P_s is the probability that electrons reaching the photocathode surface may be released into the vacuum and ν is the frequency of light.

As shown in Figure 4.3, the QE varies with the photon wavelength. The drop in sensitivity for long wavelengths is due to the reduction of energy of the photons. Thus the probability to escape the photocathode lowers to a point where the emission stops. The behaviour of the side towards higher photon energy is dominated by the transparency of the window through which the light must enter to reach the photoemissive layer. For normal glass the cut off wavelength arises at around 350 nm. Extended regions can be covered with fused silica or quartz windows (dashed lines).

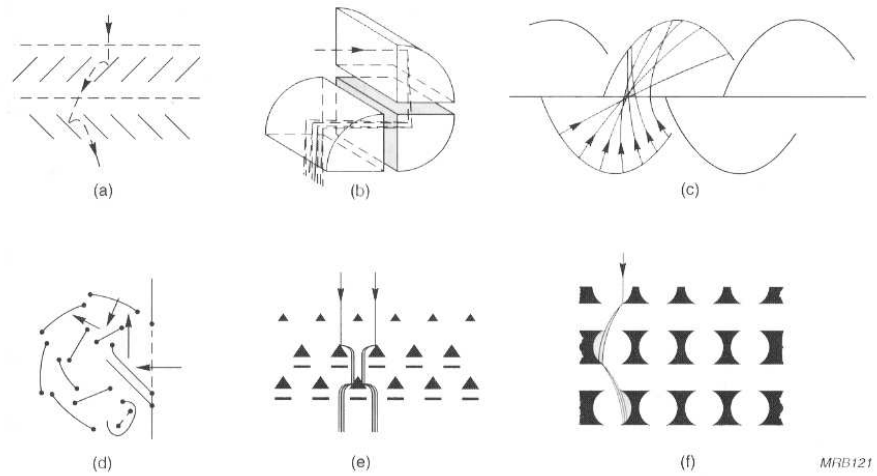

Figure 4.4: *Examples of dynode structures: (a) Venetian blind, (b) box, (c) linear focusing, (d) circular cage, (e) mesh, (f) foil [30].*

4.2 Photoelectron Multiplication

The converted photons do not produce enough electrons to be directly measurable. In order to get a useful signal the primary electrons are used to create secondary electrons in the same principle as the photoelectric effect except that the triggers are not photons but electrons.

4.2.1 Dynode Chains

Amplification is achieved through a set of dynode chains, where the dynodes are arranged such that the electric field in between them causes electrons emitted from a dynode to strike the next as shown in Figure 4.4. The free electrons from the first dynode cause the emission of more electrons at the next dynode stage. These are in turn used to produce more electrons on the next dynode and so on until the last dynode. The total gain from the dynode cascade is is given by:

$$G = \prod_{i=1}^{N} \cdot g_i \tag{4.2}$$

Where $g_i = \delta_i \cdot n_i$ is the gain at each dynode i with δ_i the secondary emission factor, n is the collection efficiency and N is the number of dynode stages. As shown in Figure 4.4 there

are different types of dynode chains arrangements (Venetian blind, box, linear focusing, circular, mesh..) all of which have their own characteristics [31]. The amplification layout should be carefully chosen according to the application the photomultiplier is employed for.

4.2.2 High Voltage Supply

The photoelectrons are accelerated using electric fields. The fields are caused by a set of levels of electric potential which are often supplied by a divider chain. This allows to control the gain ratios at the dynode from a single High Voltage (HV) source. For efficient photoelectrons collection, the potential difference between the cathode and the first dynode is usually several times greater than the dynode-to-dynode potential difference. To maintain a fixed gain, it is of primary importance to have stable potentials at all dynodes. Figure 4.5 shows the two principle ways of powering the photomultiplier.

In the positive polarity mode a), the photocathode is held at ground level and a positive HV is applied to the anode. The divider chain then supplies successive positive voltages steps between the dynodes to draw the electrons towards the anodes. As the anode is set to high potential the signal has to be coupled out via a capacity to allow the pulse

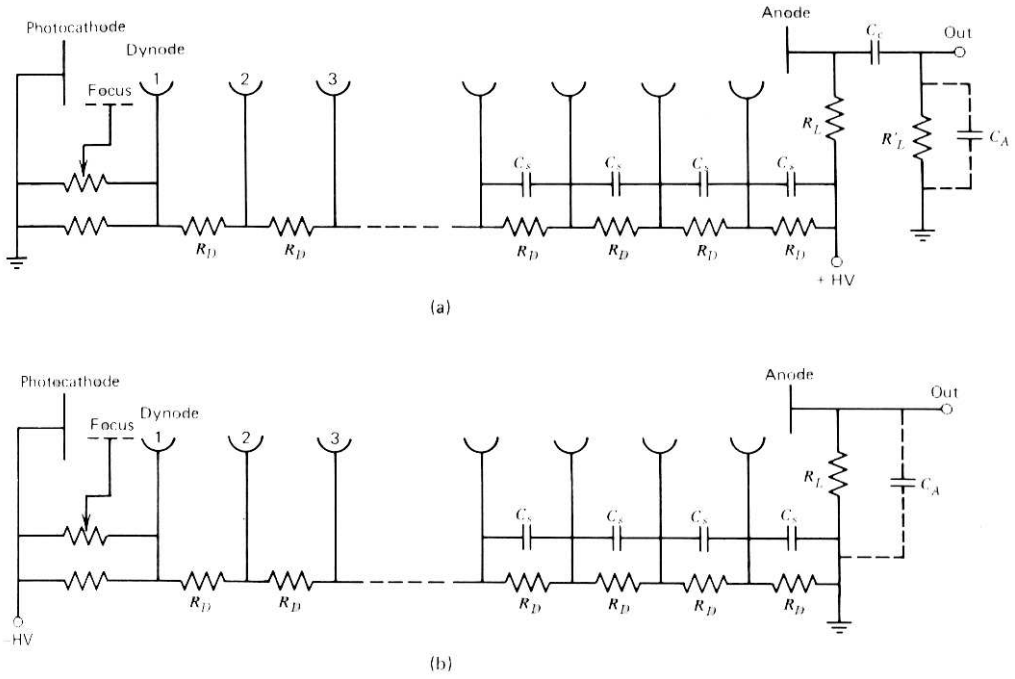

Figure 4.5: *Voltage power supply: (a) positive potential, (b) negative potential.*

component to be passed on at the ground potential. The coupling capacity C_c and the resistor R_L define the time constant of the circuit.
In the negative polarity option b), negative high voltage is applied directly to the cathode while the anode is at grounded potential. To avoid spurious pulses, care must be taken to prevent high voltage leakage through the glass tube to nearby grounded structure, for example a shield. The advantage of this setting is the elimination of the coupling capacitor C_c which allows for fast pulses.

In both cases a resistor chain allows for individual dynode gain control. Stabilising capacities, labelled C_s, are also used to prevent shifts in the potentials. An important requirement is to keep the current through the voltage divider chain large compared to the average DC signal current. This avoids any drift in the dynodes voltage equilibrium values. HV power supply must be kept as stable as possible to avoid any shift in the gains. Typical HV are of the order of a few kV.

4.3 Photomultiplier Basic Characteristics

4.3.1 Uniformity

The output sensitivity of a photomultiplier varies with respect to the position of the photon hit on the photocathode. This effect is a combination of subtle variations in the photocathode material and geometry affecting the photoelectron collection at the first dynode. A uniform signal response is desired but variations as big as 30-40 % may occur in the production of the photocathode as shown in Figure 4.6.

4.3.2 Linearity

Linearity is defined as the degree of proportionality between the amplitude of the pulse collected and the number of the photoelectrons produced at the photocathode. Nonlinearities can arise with very large pulses due to space charge effects between the last dynode and the anode. The build-up of charges affects the trajectories of electrons and causes some to be lost. An additional deviation in the dynode voltages from their equilibrium may result in nonlinearities.

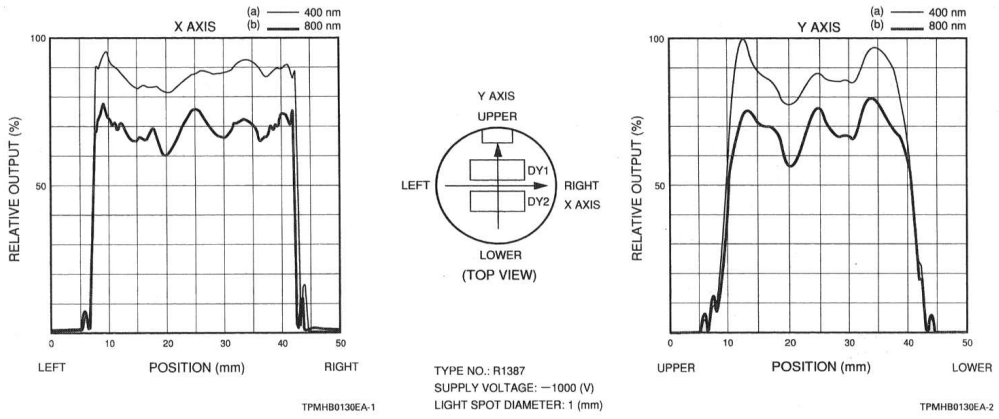

Figure 4.6: *Difference of uniformity with position and photon wavelength [31].*

A linear behaviour is also desired between the amount of light absorbed by the photocathode, the amount of charge collected and the anodes so that the signal can be directly measured. This linear regime is always limited towards high signal gains. The large electron densities between the last dynodes of a tube lead indeed to space charge effects. They shield and effectively change the set potentials between the dynodes. This causes a gradual saturation of the signal.

4.3.3 Stability

The output signal of a photomultiplier may vary as a function of time mainly due to fatigue. Suppliers often quote the drift, for short time instabilities and life characteristic for periods longer than a year. Stability depends on variations in the secondary emission ratio, i.e the gain variations over time. This is simply due to the fact that the cathode has an intrinsic stability. The drift can be stabilised by a ageing technique which consists of continuously operate the tube for a dozen hours after production and warming up for one or two hours before actual use.

4.3.4 Dark Current

The dark current consists of any unwanted current flow in the tube. It is a critical factor that governs the lower detection limit in low light level measurements. It can be categorised as follows: (see Figure 4.7)

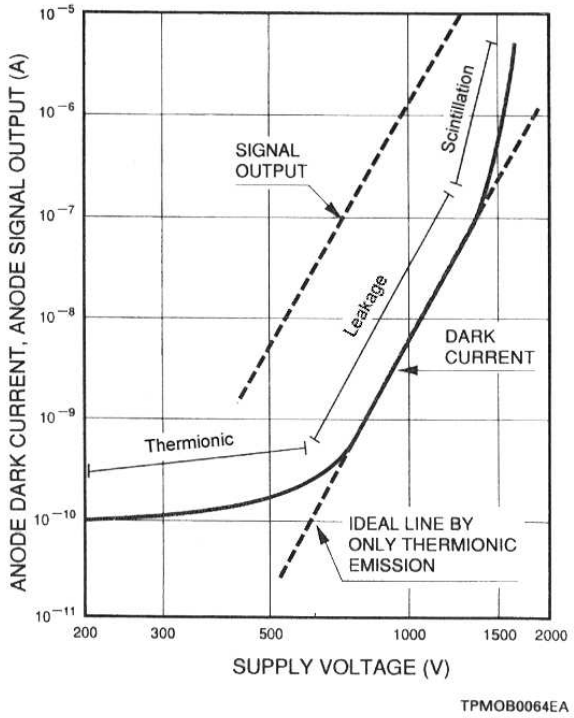

Figure 4.7: *Typical dark current with the main causes identified vs supplied voltage [31].*

- **Thermionic emission current from the photocathode and dynodes**: Thermionic emission is due to the very low work functions of the materials used. Consequently thermionic electrons can be emitted even at room temperature and current can therefore flow even without applied voltage. W. Richardson established that the thermionic current is given by:

$$i_s = A.T^2 e^{-eW/kT} \tag{4.3}$$

  where W is the work function, e the electron charge, k the Boltzmann constant, T the absolute temperature, and A is a constant. At room temperature, the current density of photocathodes with a maximum sensitivity in the range of 300 to 500 nm is between 10 and 1000 electrons/cm^{2}s.

- **Leakage current (ohmic leakage)** due to the high voltage and low currents operation. This can happen between the anode and other electrodes inside the tube.

- **Photocurrent produced by scintillation**: It is usually produced by scintillation from the glass envelope.

- **Cosmic rays, radiation from radio isotopes contained in the glass en-**

velopes and environmental gamma rays: They can lead to noise current too. Muons coming from cosmic rays can indeed become a problem when passing through the glass envelope. They can cause Cherenkov radiation hence releasing a large number of photons. Glass contains potassium oxide (K_2O) with minute amounts of radioactive element ^{40}K. Beta rays can be emitted from these isotopes adding a source of noise.

- **Field emission currents**: They arise when operating the photomultiplier at excessively high voltage.
- **Ionisation currents from residual gases (ion feedback)**: Even though a photomultiplier tube is kept in vacuum, residual molecules may be ionised by collisions with electrons. The positive ions striking the front stage dynode then produce secondary electrons resulting in a large noise pulse. The pulse appears slightly after the photocurrent and hence is called an afterpulse or ion feedback.

4.4 Signal Output Shape

The signal output shape of a photomultiplier tube is in the simplest case described by a Poisson distribution. Its statistical nature arises from the fact that each photoelectron is actually not subject to the exact same multiplication factor δ. As a result the output pulses coming from a single electron do not have the same amplitudes.

For a single photoelectron incident on the first dynode, the number of secondary electrons produced has a mean value δ and a standard deviation σ of $\sqrt{\delta}$. The relative variance defined by σ^2/δ^2 is then $1/\delta$. For N identical stages the mean number of secondary electrons becomes δ^N and the Poisson distribution variance can be written as:

$$\frac{1}{\delta} + \frac{1}{\delta^2} + ... + \frac{1}{\delta^N} = \frac{1}{(\delta - 1)} \tag{4.4}$$

The higher δ the more discreet the peaks are. Figure 4.8 shows signal peaks for a multiplication factor of 5.

While this is the simplest case, there exist however no general descriptions due to the fact that the signal shape highly depends on the structure of the tube. In some cases for example the signal is better described using a Polya or compound Poisson distribution.

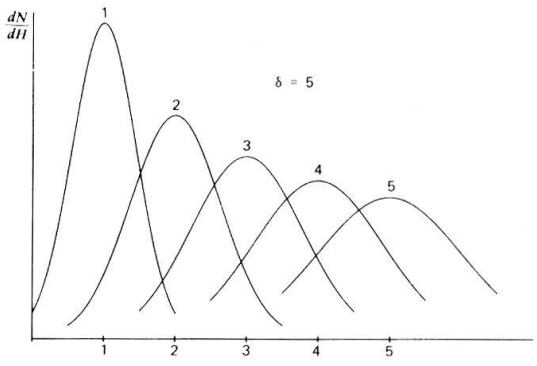

Figure 4.8: *Photomultiplier signal output shape contributions for a multiplication factor δ of 5.*

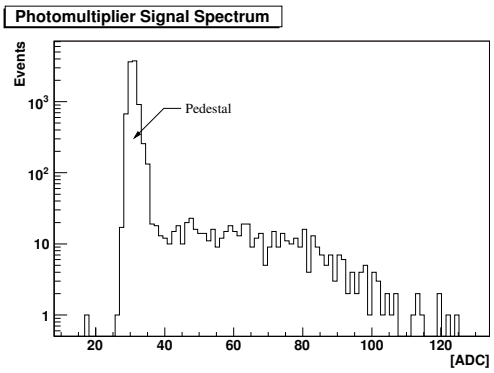

Figure 4.9: *A typical signal spectrum of a photodetector showing the pedestal and the signal.*

Noise has also a significant contribution to the signal spectrum. It is has two components: 1) the thermionic noise present even when there is no light input and 2) the induced dark current. This contribution is visible as a large peak preceding the signal spectrum as shown in Figure 4.9 and is referred to as the pedestal.

4.5 Effects of Magnetic Fields

Photomultiplier tubes are in general very sensitive to magnetic fields. They are even sensitive to the earth's magnetic field of 0.03 mT. The most sensitive part is the collection system where the trajectories are the longest. In the worst case an electron is deviated enough so that it does not reach the first dynode. Figure 4.10 shows the different effects of the magnetic field on the gain of a tube with (a) linear focusing dynodes and (b) Venetian-blind dynodes in which cases:

- The anode current decreases as the magnetic flux increases.
- The influence of the field is least when oriented along the axis of the tube.
- Long exposure can result in the magnetisation of some parts of the tube.

High permeability materials such as μ-metal, an 80% nickel-iron alloy specially designed for magnetic shielding applications, are commonly used to protect the tubes. In general, it

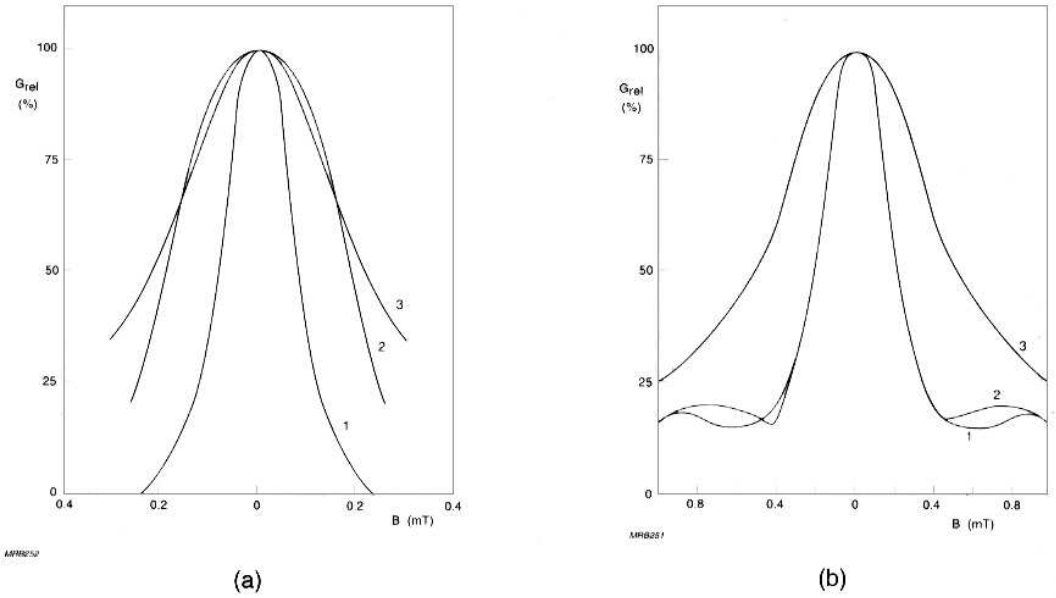

Figure 4.10: *Relative gain variation as a function of magnetic field for (a) a tube with linear focusing dynodes and (b) for a tube with Venetian-blind dynodes. Curve 1 and 2 are for an applied transverse field and curve 3 for a longitudinal field [30].*

should extend about one diameter beyond the cathode plane in order to avoid edge effects. If the tube is operated at negative polarity, the shielding must be completely insulated from the glass or connected to the cathode potential via a protective resistor.

4.6 Multianode Photomultiplier Tubes

4.6.1 Properties of the MaPMT

Multianode PhotoMultiplier Tubes (MaPMT) are built by the Japanese company Hamamatsu. The LHCb RICH detector considered the photomultiplier of the R7600-03-M64 series [53]. Its structure consists of an 8×8 array of 64 anodes with a cell granularity of $2\times2\,\mathrm{mm}^2$ and a 0.3 mm gap separation for a physical size of about $25\times25\times20\,\mathrm{mm}$, without connecting pins. A schematic is shown in Figure 4.11. Its bi-alkali photocathode is deposited on the inside of a 0.8 mm thick semi-transparent UV glass window. The quantum efficiency, shown in Figure 4.12, peaks at 22 % for a photon wavelength of 380 nm and has a photosensitive energy range of 2.1 to 6.2 eV.

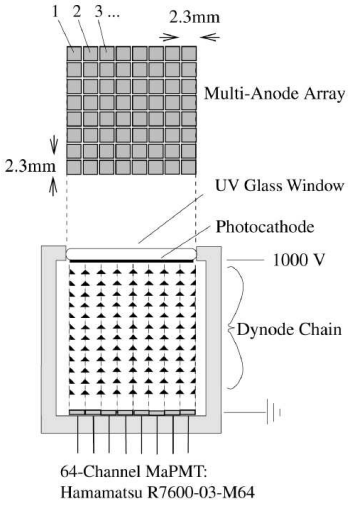

Figure 4.11: *Internal structure of an MaPMT with the top view of the multi-anode array.*

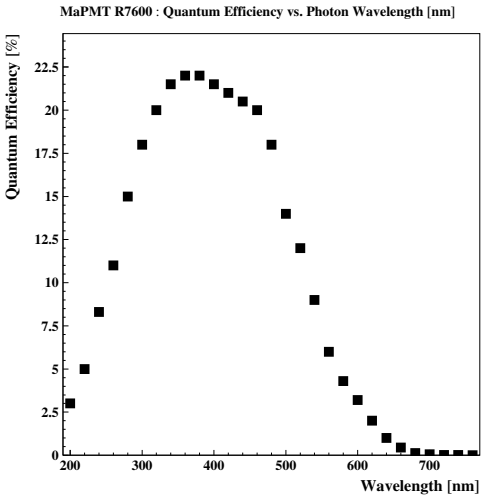

Figure 4.12: *Quantum efficiency distribution for an MaPMT tube, measured by Hamamatsu.*

Once the photons have been converted to photoelectrons they are focused towards the amplification stage using a mask of 75 μm thin wires kept at the same potential as the photocathode. Each pixel has two rectangular slit entry windows as sketched in Figure 4.13. They are approximately $1.8 \times 0.5\,\mathrm{mm}^2$ and are separated by a catwalk of 0.5 mm overlayed by the focusing wires. The electron amplification, as illustrated in Figure 4.11 consists of an array of 12-stage dynode chains, one for each pixel. The gain of the MaPMT is about $3 \times 10^5\, e^-$ at 800V and can be controlled via the dynode resistor chain. The amplification level of each dynode was set to the default values provided by the manufacturer as shown in table 4.1. The divider chain was used in the negative potential configuration as illustrated in Figure 4.5 b).

Dynode	PC	1	2	3	4	5	6	7	8	9	10	11	12	A
Resistor		R_1	R_2	R_3	R_4	R_5	R_6	R_7	R_8	R_9	R_{10}	R_{11}	R_{12}	R_A
R[$10^5 k\Omega$]		3	2	2	1	1	1	1	1	1	1	1	2	5

Table 4.1: *Values of the resistors R used for the divider chain. PC is the photocathode and A is the Anode.*

There is also a 8-dynode stage MaPMT with an amplification gain of 0.5×10^5. This version became available later and it was of interest for LHCb because the signal directly fitted

the range of the electronics developed for the read out. The 8-dynode stage were used along side the 12-dynode stage MaPMTs in the testbeam study described in Chapter 7.

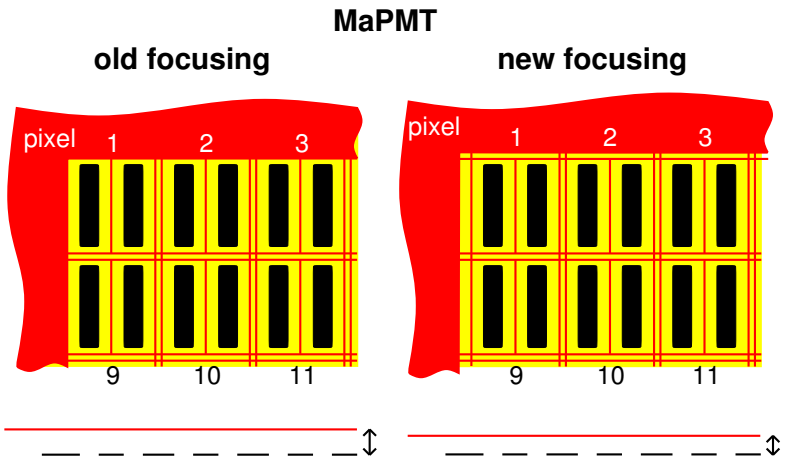

Figure 4.13: *The mask of focusing wires (red) and the mask entry windows (yellow) in front of the dynode chains (black) for the old and the new focusing types. Also sketched is the distance of the focusing grid brought closer to the entry windows.*

4.6.2 Models Used for the Magnetic Field Studies

Two types of MaPMTs have been used for the magnetic field studies of Chapter 5. The "old 9C" series used for the 1999 testbeam [20] and the "new" 9K series. The "new" tube differs in the layout of its focusing wires in order to improve the homogeneity at the edge pixel for a better pulse height and collection efficiency. As shown in Figure 4.13 the new focusing has indeed an additional wire running along the edge of the structure with also a mask brought closer to the dynode chain.

Chapter 5

Multianode Photomultiplier Tube Signal Response in Magnetic Fields

A major step in the development of the RICH system has been the re-optimisation of the LHCb detector. Tracking stations situated in the magnet have been discarded and additional magnetic field has been required between the VELO and the TT stations in order to improve the Level-1 trigger performance.

As a result the iron shielding plate, which was located between RICH1 and the magnet, was removed. This caused an increase of the magnetic field from an anticipated 1.5 mT to 60 mT in the region of RICH1. In these conditions, the photodetectors could not be operated and a magnetic shield box surrounding the structure was designed. Downstream of the magnet, the magnetic field in the region of RICH2 however remained the same at about 14 mT. No modification to the RICH2 protecting structure has been required. The challenge of the RICH1 shielding structure has been to provide adequate protection for the photodetector, targeting a magnetic field of less than 2.5 mT at the photomultiplier plane. The task had been made more complicated in that no decision had been made between which of the two competing types of photodetector to use: the Hybrid PhotoDetector prototype (HPD)[36] or the Multianode PhotoMultiplier Tubes (MaPMT).

While previous measurements in magnetic fields up to 3 mT [40] showed the capability of using shielded MaPMT as photodetectors, it became very important to obtain better

measurements on their sensitivity to magnetic fields and on the extend to which they could be shielded.

5.1 Measurement Setup

5.1.1 Apparatus

The behaviour of MaPMTs in magnetic fields has been tested with the setup shown in Figure 5.1. It consists of a magnet capable of producing an axial magnetic field of up to 900 mT in a 12 cm wide gap. The current needed to produce a given magnetic field was calibrated with a Hall probe and the measurements have been kept in the 0 to ± 35 mT range in which the hysteresis of the magnet could be neglected. The upper value of the range is dictated by the field value above which no signal is readable from the MaPMT. The opening is wide enough to place the MaPMT tube in any of the directions of the tubes coordinate system. The z-axis of the MaPMT is defined as the axis perpendicular to the photocathode. Unless otherwise stated the measurements were taken with the magnetic

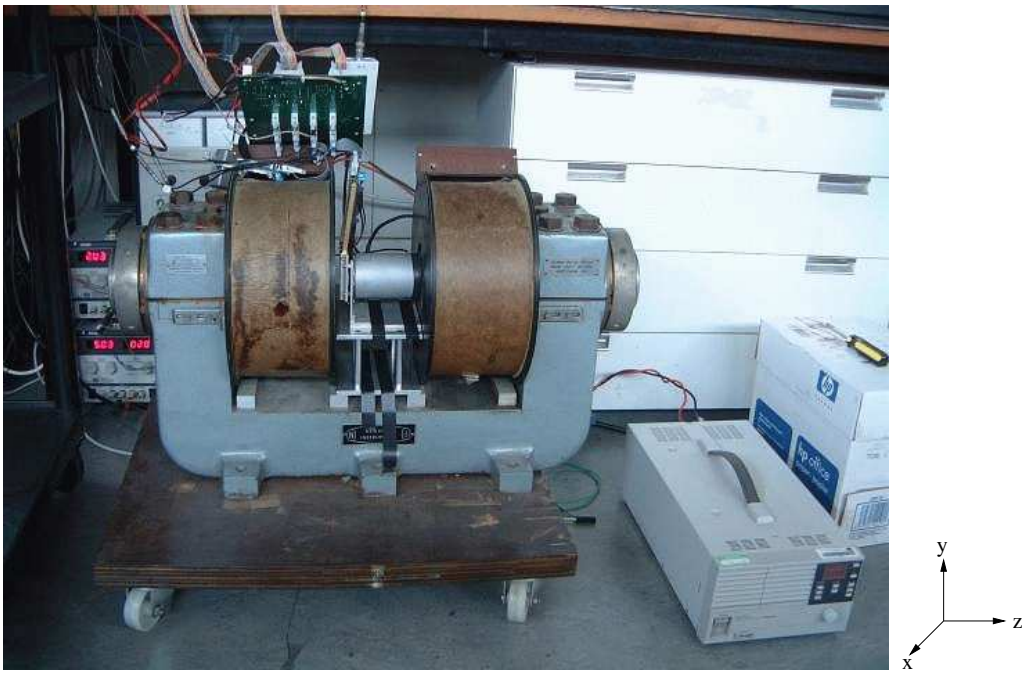

Figure 5.1: *Magnet and MaPMT housing (See Appendix A.1 for an enlarged view of the opened housing with the MaPMT). The z-axis is defined as perpendicular to the photocathode of the tube, x is the horizontal transverse axis and y the vertical transverse axis.*

field parallel to the MaPMT z-axis.

A separate housing was designed to accommodate the readout and to provide a light tight environment for the MaPMT. A ring of four blue LEDs with a wavelength of 430 nm was used as light source, see the housing inside view in Appendix A.1. The end of the aluminium box is fitted with white paper to diffuses the light. This provided a sufficiently homogeneous light distribution at the MaPMT window.

5.1.2 Front-end Electronics

The MaPMT was coupled to a Front-end board via kapton cables. The Front-end board multiplexes the analogue signal using an Analogue Pipeline Voltage application chip (APVm) [50] implemented as an Application Specific Integrated Circuit (ASIC). It is a radiation-hard front-end circuit from the APV series designed for the CMS inner detector [52]. The circuits deals with signals approximately 10 times smaller than those from an MaPMT which thus had to be attenuated using a AC coupler integrated on the Front-end board seen in the schematic of Figure 5.2.

The board can accommodate two MaPMTs at once and hence the ASIC receives 128 signals which, after digitisation, are multiplexed at 20 MHz into one interlaced analogue data output shown in Figure 5.3. A 12 bit control header containing the pipe line addresses

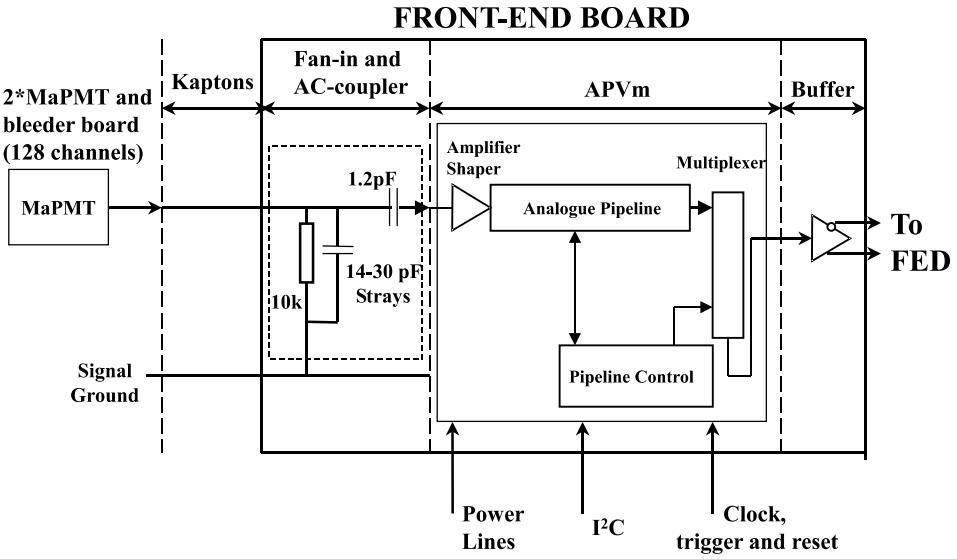

Figure 5.2: *A schematic of the Front-end board, the APVm ASIC and the AC-coupler [20].*

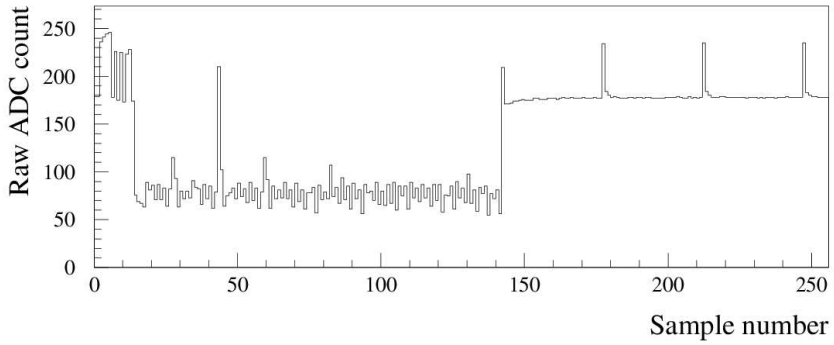

Figure 5.3: *Example of the APVm ASIC output after digitisation [20]. The header and pipe address bits appear on the left-hand side of the frame. A Photon signal is visible at sample number 45 .*

at which the data were stored and an ASIC error flag precede the data frame. Control voltages and currents can be set individually via an I^2C control link [51] fanned out by an interface board capable of driving eight front-end boards.

5.2 Data Acquisition

5.2.1 Data Acquisition Electronics

The data acquisition consists of a VME (Versa Module Europa) based system which drives the Front-end electronics. The different modules and their relationship are given in Figure 5.4.

An individual pulse generator synchronises the LED light and a SEQSI (Sequencer for use in Silicon readout Investigation). The SEQSI then generates a 40 MHz clock signal and triggers the APVm ASIC with a 25 ns LVDS pulse. The signal is used to trigger the Front End Digitiser (FED) to digitise the data frame. The FED is a PCI Mezzanine type card (PCM) which was designed as a prototype module for the CMS inner tracker. A separate level changer board performs a level shifting and amplifying to fit the PCM dynamic range. The level changer also differentiates and converts the trigger signal to LVDS. An APVm reset pattern is sent at the end of the data taking time through the SEQSI which empties the pipeline. The FED returns the data via a VME-PCI interface (ACAL:midas) and the memory mapping of the VME address can then be read with the data acquisition PC via

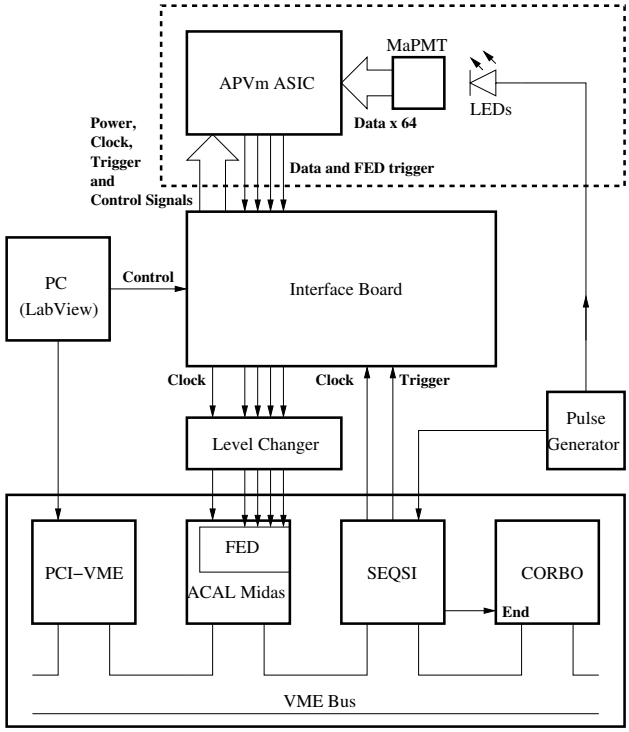

Figure 5.4: *A schematic of the APVm based read-out electronic and the data acquisition system. The components in the dashed box are placed in the magnetic field.*

the PCI-VME card. The data acquisition is controlled by a LabView interface on an NT windows PC machine.

5.2.2 Protocol

For the purpose of the data taking, the high voltage of the MaPMT was set to -1000 V. The trigger rate at the pulser was chosen to be 1 kHz and exactly 24558 events were taken per run. The magnetic field was varied in the range of 0 mT to ±35 mT: in steps of 1 mT up to ±10 mT and in steps of 5 mT thereafter. The procedure was as follows: First a pedestal run was taken for which the LEDs were switched off. Then a measurement at a magnetic field of 0 mT was taken with the amount of light adjusted to a level such that for each individual MaPMT channel a signal occurred in 20-30 % of the events. The sequence of measurements followed a hysteresis curve: first a series of data were taken by increasing the negative magnetic field from zero to its maximum value and decreasing it back to zero (15 values per direction). After switching the polarity of the magnet power supply another pedestal run was taken and the procedure was repeated for positive magnetic fields.

5.2.3 Experimental difficulties

The main issue met during data taking was the synchronisation of the APVm with the FED. The trigger signals were not as well defined as in an ideal setup and this became a problem at the level of the LVDS conversion. Figure 5.5 shows signals recorded with an oscilloscope.

The first trace 1) is the APVm data frame on which a photon signal from the MaPMT can been seen. The APVm sends two triggers shown in trace 2): the first to enable the FED before the 5^{th} header bit and the second to disable it after the 128^{th} data bit. Traces 3) and 4) show the negative and positive output of the LVDS signal. Trace 2 displays the differentiated signal and is phased zoomed at 20 ns/Div in B) with an additional level zoom at 0.50 V/Div. The signal is $\sim 1.6\,V$ large. The signal from the LVDS trigger was picked up with a 100 Ω terminator and displayed in D). This signal can be adjusted via

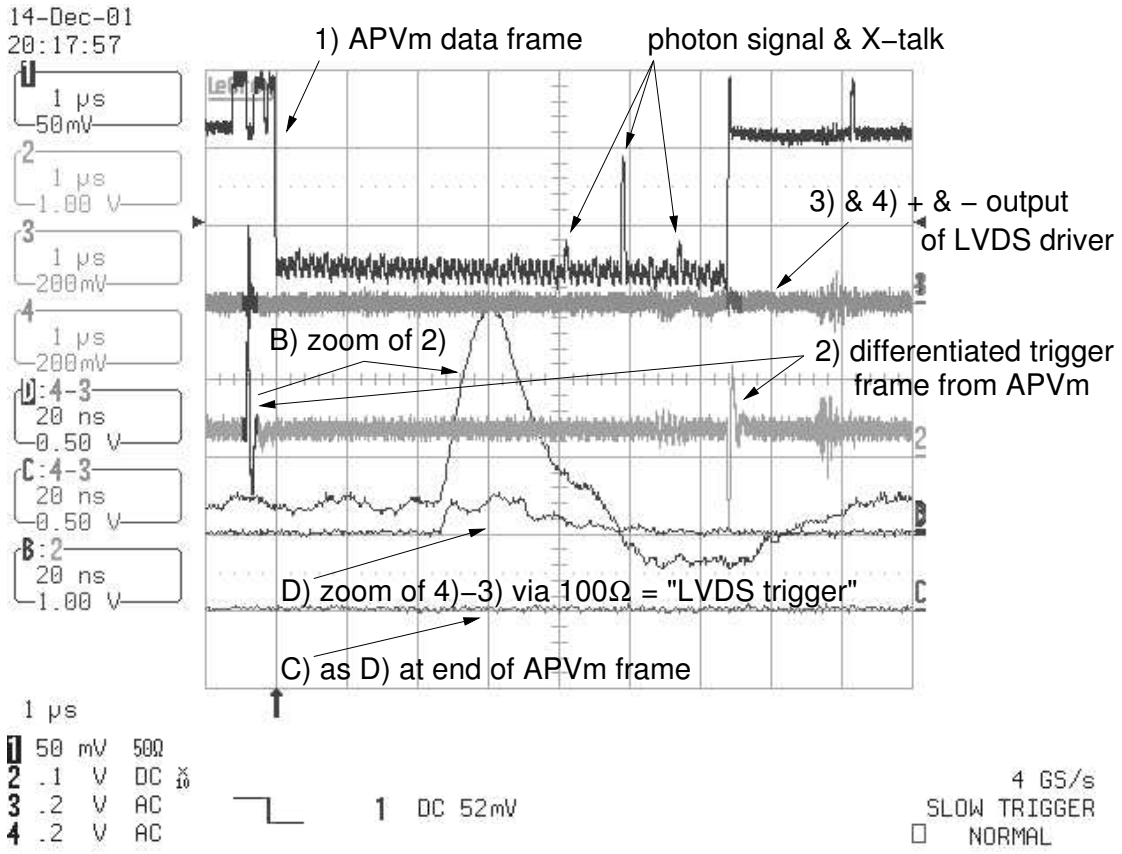

Figure 5.5: *Screen shot of the LVDS trigger setup synchronising the APVm data frame with the FED [54].*

two variable capacitors controlling the time delay and the offset. It had to be shaped so that the pulse would be 15 ns to 25 ns wide while at the same time no second pulse would be generated at the end of the data frame in trace C).

The difficulty arose in that the signal adjustment could not be maintained reliably over a long time, causing a loss of trigger during the sequence of data taking. The data would then have to be retaken from the beginning. This is notably due to a temperature dependence. A stable configuration would only be achieved after the warm up of the VME crate. A room temperature above 25°C was also a problem making the calibration almost impossible. The data taking went on despite this unsolved problem and not without frequent frustrations.

5.3 Data Analysis and Results

5.3.1 Data Processing

The recorded raw data were transferred and analysed on a computer cluster running a Linux operating system. After removing multiple consecutive copies of the event and overflowed channels that may occur, each run undergoes an event-by-event common mode correction described in [20] aimed at correcting for the signal jittering which caused time-dependent shifts in the pedestals of each channel. Afterwards, a Gaussian fit was applied around the pedestal region of each channel. Using the fit results for the pedestal position, Q_0, and width, σ, a threshold value $Q_0 + 5\sigma$ was defined for each channel. All entries above the threshold cut were regarded as signal from a photoelectron. The signal fraction, i.e. the ratio of signals to all events, was tuned to be within 20-30 % for the average of the 64 channels of a tube for no external field. Figure 5.6 shows the signal spectrum of a single channel at 0 mT with the signal area shaded. A "shoulder" is visible between the pedestal peak and the signal plateau, between about 35 and 60 ADC counts, which is attributed to electronic cross-talk as will be discussed in section 5.3.3. The right hand side of Figure 5.6 also shows a map of an MaPMT indicating the signal fraction (in percentages) measured for the 64 channels. Channels with problems were masked and were not used for the analysis. This was acceptable as only the average of all signal values added together was considered. This was always true for channel 48 which had a problem in the front-end

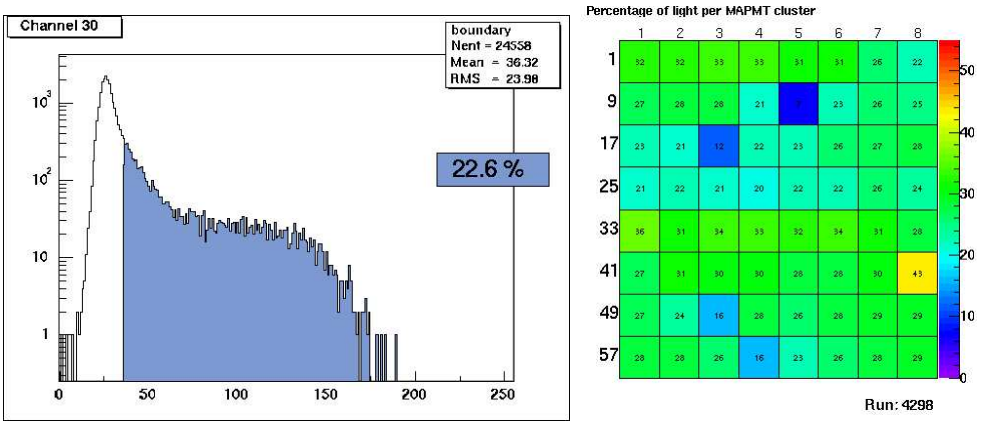

Figure 5.6: *Left: the spectrum of channel 30 with the signal fraction shaded; Right: the signal fractions (in percentages) measured for the 8×8 channels of an MaPMT.*

electronics resulting in a double pedestal peak. But channels which suffered from low gain (channels 13, 19, 51, 60 in Figure 5.6) were also excluded. A set of data is given in Appendix A.2 as an example.

5.3.2 Global Signal Fraction

The global signal fraction of the MaPMT is defined as the average of the individual signal fractions of all good channels of an MaPMT. To study the behaviour in the magnetic field the global signal fraction is then normalised to the value obtained for zero external field.

In the case of a longitudinal field, shown in Figure 5.7 (top), the global signal fraction starts to decrease as soon as a magnetic field is applied. The decrease is to a good approximation proportional to the magnetic field strength, and it is slightly stronger for positive fields up to 10 mT. The signal fraction drops to 90 % around 2 mT, and to 80 % between 3.5 mT and 4.0 mT.

In the case of transverse fields, shown in Figure 5.7 (bottom), only the x-direction has been tested. This confirms previous tests on lower magnetic fields made up to 3 mT [20] where it was shown that the y-direction does behave in a very similar manner. The MaPMT is almost insensitive to transverse magnetic fields up to ±20 mT where the global signal fraction decreases only by less than 10 %. At higher fields the signal starts to drop sharply.

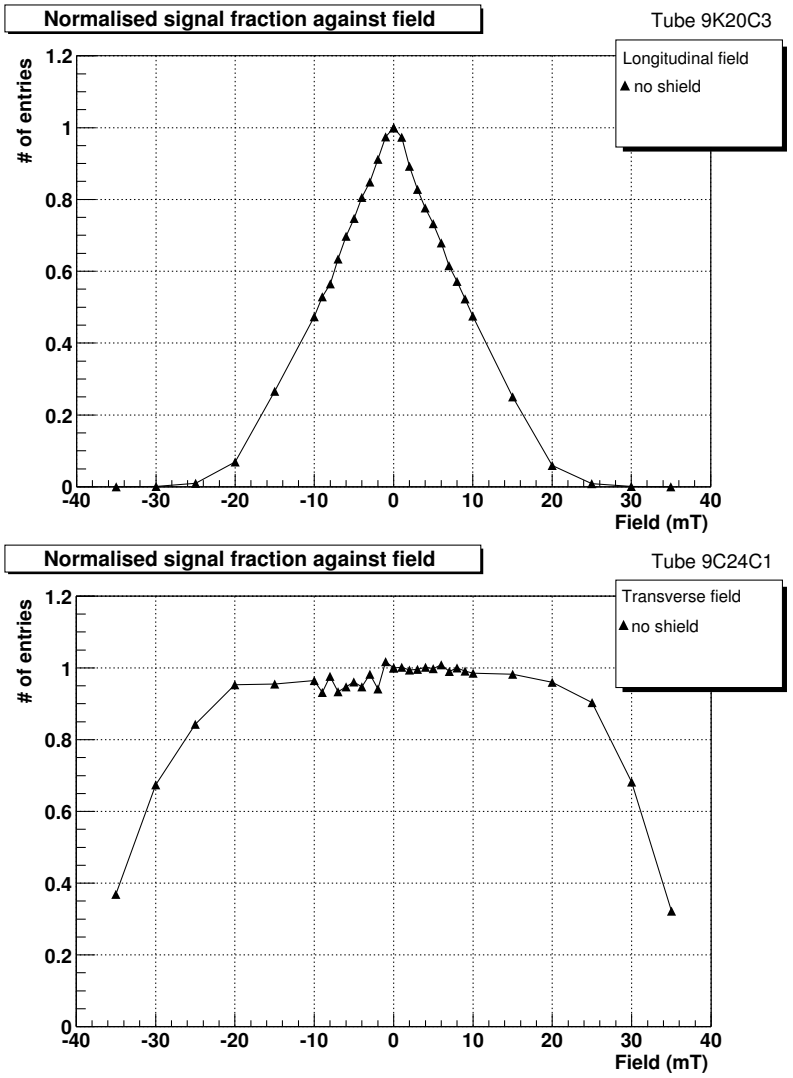

Figure 5.7: *The global signal fraction of a unprotected MaPMT for (top) fields in the longitudinal axis (tube 9K20C3) and for (bottom) fields in the transversal axis (tube 9C24C1).*

5.3.3 Signal Fraction Groups of Rows and Columns

To learn about the pattern of signal response in different regions of the MaPMT the signal fraction has been studied for rows and columns of channels. A row of an MaPMT is defined by eight adjacent channels in the horizontal (x-axis), using the channel map of Figure 5.6. For example, row 2 is formed by channels 9 to 16. The signal fraction is averaged over the channels of a row or a column, respectively, and then normalised to the measurements without field. Results for longitudinal negative magnetic fields are displayed in Figure 5.8. To guide the eye the measurements for eight columns or rows taken at the same magnetic field are connected by a line. In the case of columns a progressive loss of the signal fraction

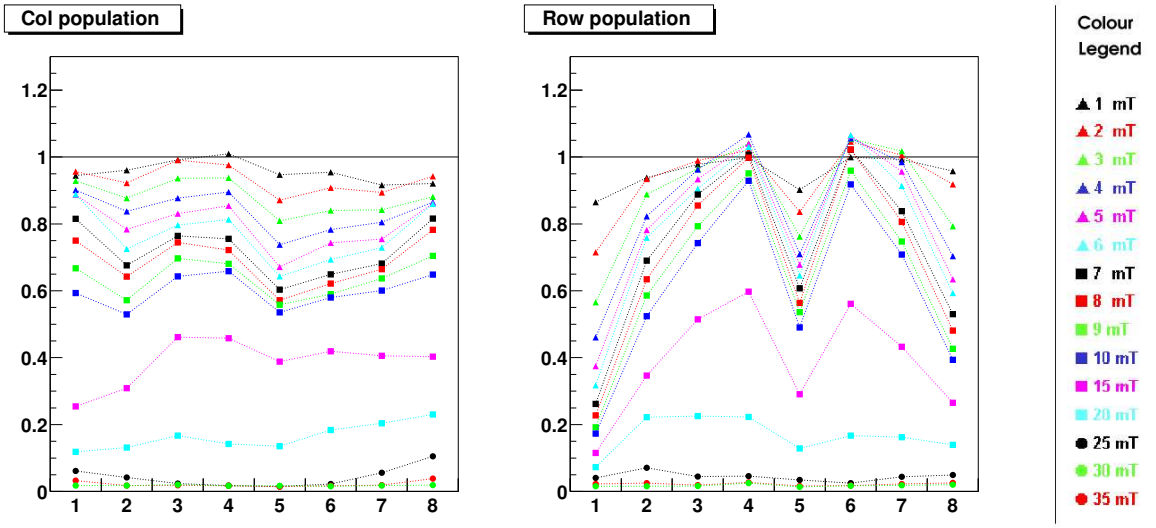

Figure 5.8: *Normalised signal fraction for columns and rows versus column and row number, respectively. Points taken at the same field are joined by a dashed line to guide the eye.*

is observed which is roughly proportional to the field strength until virtually no signal is measured anymore at 25 mT. The behaviour is very similar for all columns, and it matches the dependence of the global signal fraction plotted in Figure 5.7. For rows of MaPMT channels, a different behaviour of the signal fraction versus magnetic field is observed. The rows on top (row 1) and the bottom of the tube (row 8) exhibit a decrease of the signal fraction which is much stronger than for the rows in the centre of the tube. This rapid loss of signal in the top and bottom rows of the MaPMT has been identified as a feature of the tube itself [20].

The signals in row 5 are subject to a strong asymmetric, i.e. one-way, cross-talk from signals of row 1. This behaviour was identified in the APVm readout in [20] and it is attributed to cross-talk internal to the APVm chip. This effect was verified by the application of a mask in front of the MaPMT which covered all but the channels of row 1. As shown in Figure 5.9, a cross-talk in excess of 50% from the channels of row 1 to row 5 is observed. In the other direction no significant cross-talk is observed. This means that a loss of signal in row 1 will appear as loss in row 5 as seen in Figure 5.8.

To better illustrate the results of Figure 5.8, the normalised signal fraction against the applied magnetic field has been plotted in Figure 5.10 for a set of selected rows of pixels of tube 9C20A2. The signal fraction of row 3 (squares) decreases by less than 10% up to longitudinal fields of 5 mT. A very similar behaviour is observed for all other non-edge rows (2 to 7). This implies that three quarters of the MaPMT channels are rather insensitive to longitudinal fields up to 5 mT. However, the top (triangles) and bottom rows (filled bullets) lose up to 50% of the signal at 3 mT. The top and bottom rows of the MaPMT are sensitive to fields above 1 mT. Also shown is the averaged global signal fraction (open bullets) which stays above 90% up to fields of about 2 mT.

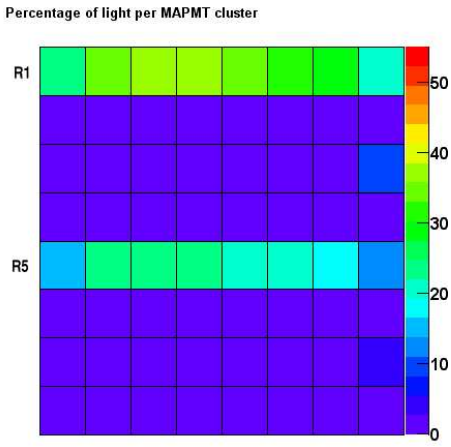

Figure 5.9: *Cross-talk between row 1 and row 5.*

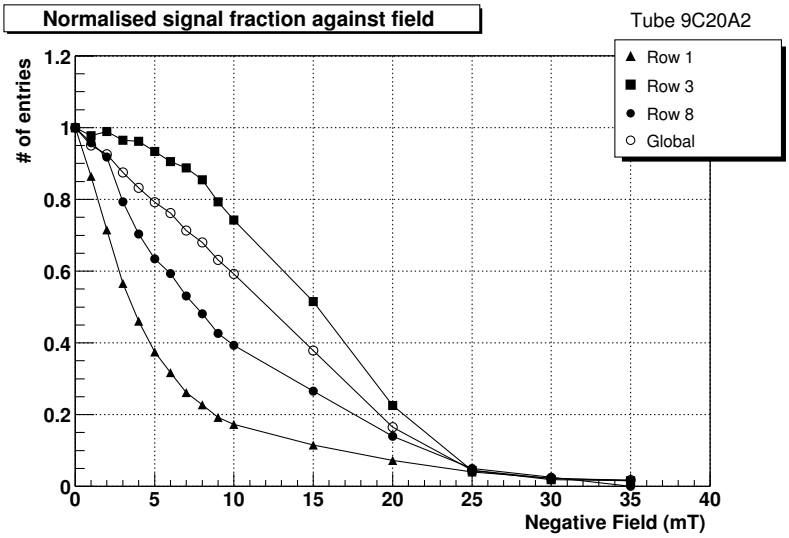

Figure 5.10: *Normalised signal fraction against the longitudinal negative magnetic field for rows 1, 3, 8 and for the global average.*

5.3.4 Nature of the Losses

In order to investigate the nature of the loss in the MaPMT, the gain of the tube has been estimated by calculating the centre of gravity (COG), also called the first moment of the

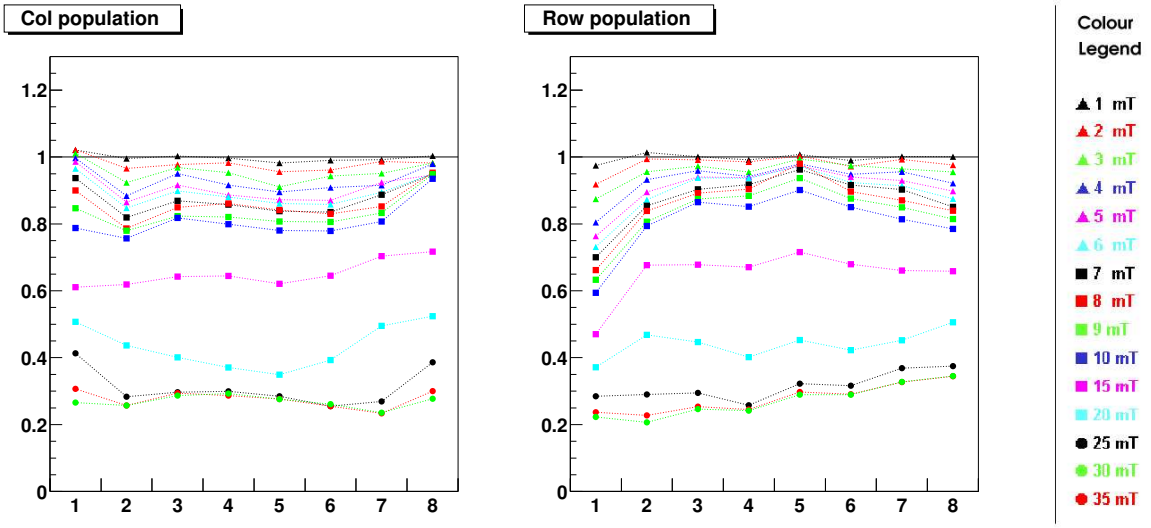

Figure 5.11: *Centre of gravity of signal hits for columns and rows versus column and row number, respectively. Points taken at the same field are joined by a dashed line to guide the eye.*

signal spectrum, for each channel according to the following equation :

$$COG = \frac{\sum_{i=a}^{i=256}(i-a) \times Ei}{N} \tag{5.1}$$

where a is the position of the threshold, i is the channel number, E_i is the value of the channel and N is the total number of entries above the five sigma cut. The average of all COGs is calculated for the channels of a row or column, respectively. Again the results are normalised using the measurement for no external magnetic field as reference.

The results in Figure 5.11 show that the COG decreases significantly less than the signal fraction displayed in Figure 5.8. The average loss of gain is less than 10% for longitudinal fields up to 5 mT. This suggests that the decline of the signal fraction with increased magnetic field has to be predominantly attributed to primary photoelectrons being lost before the entry to the dynode structure. A smaller fraction of the signal is lost due to a reduction in gain, i.e. electrons lost within the dynode structure.

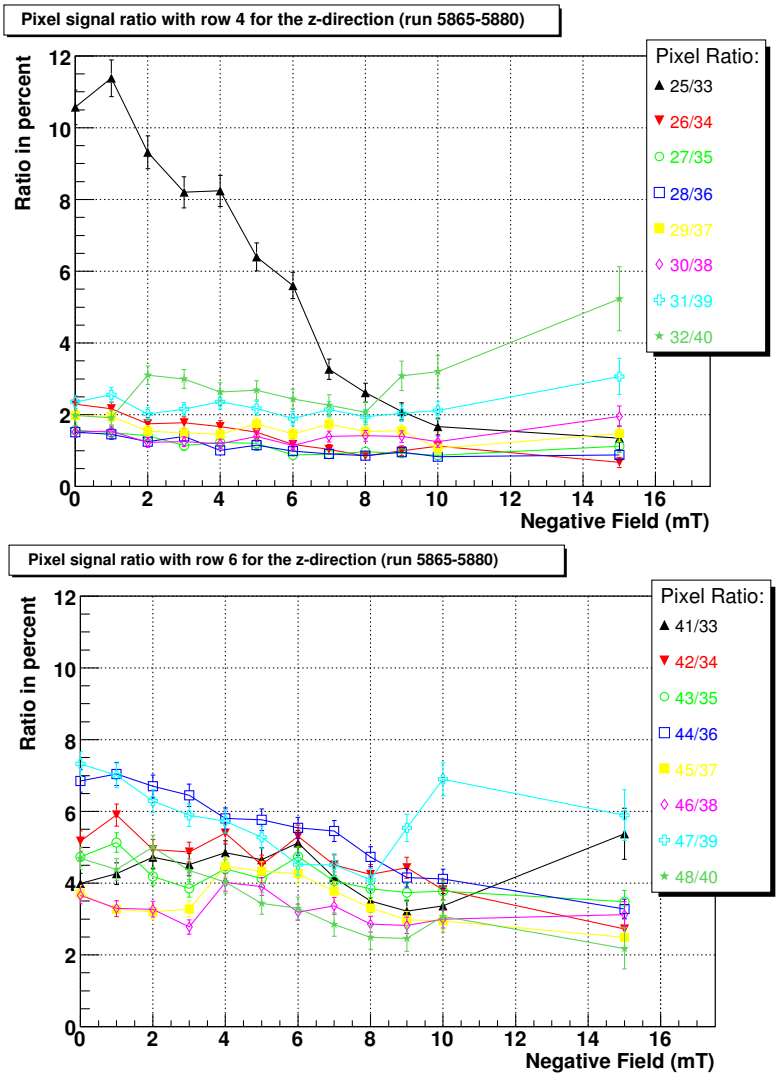

Figure 5.12: *Signal spill-over for longitudinal fields for channels adjacent to row 5 (of tube 9K20C3); Top: channels of row 4, Bottom: channels of row 6; lines connect the results for each pixel to guide the eye.*

5.3.5 Transverse Spill-Over

The spill-over of signal into neighbouring channels due to the external magnetic field was also studied. A pinhole mask was placed in front of the MaPMT leaving only the pixels in row 5 exposed to LED light. Then the signal fraction of the channels adjacent to the top and bottom of an illuminated channel was regarded. It was normalised by the signal fraction of the illuminated channel and displayed as a function of the magnetic field in longitudinal and transverse direction. An increase of this ratio to one side of the illuminated channel would indicate a spill-over of signal to the neighbour. This could

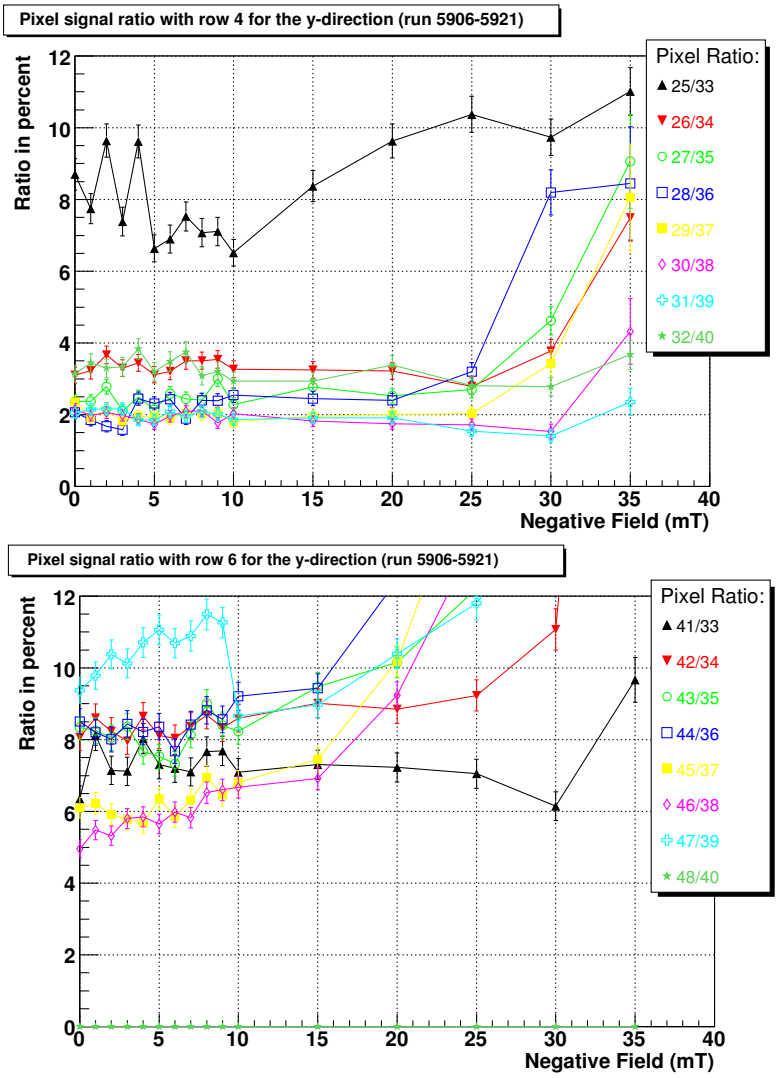

Figure 5.13: *Signal spill-over for transverse fields for channels adjacent to row 5 (of tube 9K20C3); Top: channels of row 4, Bottom: channels of row 6; lines connect the results for each pixel to guide the eye.)*

happen by photoelectrons emitted from the cathode being diverted to the entry window of the neighbouring channel or by the distortion of the electron trajectories between the dynodes resulting in a charge sharing of the two adjacent channels.

Figure 5.12 shows the spill-over values for longitudinal magnetic fields where values for the same pixels are connected by a line to guide the eye. The signal fraction map from the set of data taking can be found in Appendix A.3. At least up to 10 mT the ratio of signal fractions stays stable, i.e. no signal spill-over is found. Beyond 15 mT the absolute number of signals in the spectra becomes so low that the statistical error becomes to big to draw a conclusion

in that region. The behaviour of channel 25 differs from the other channels for which no explanation can be given, but it is likely that the pinhole was not well centred on this pixel.

Values for the transverse magnetic fields are shown in Figure 5.13 where again the values for each pixel are connected by a line to guide the eye. The signal fraction map from the set of data taking can be found in Appendix A.4. In this case the region of a stable ratio of the signal fractions extends up to 25-30 mT for the upper row or 15-20 mT for the lower row. This is consistent with the extended region of small signal loss for the transverse fields as shown in Figure 5.7. In conclusion again no sign of a signal spill-over is seen for the region where the measurement is not dominated by small signal fractions and thus large statistical fluctuations. As in the case for longitudinal magnetic fields the behaviour of channel 25 is different than for the other channels.

5.4 Effect of Shielding

The loss of photoelectrons due to a magnetic field has to be below a critical level of operation set for the photodetectors of the LHCb RICH detectors. An efficiency of 90 % with respect to the case of zero field is required for the recognition of a signal above the threshold cut. As demonstrated in Figures 5.7 and 5.10 this limit is already reached with a longitudinal field of about 2 to 3 mT.

The conclusion of Section 5.3.4 confirms the expectation that the MaPMT is most sensitive to magnetic fields in the region between the photocathode and the first dynode. Therefore the strength of shielding in this region dominates the overall effect of the shields.

5.4.1 The μ-metal Shield Prototype

A solution to protect the tube with a μ-metal shield has been studied. The prototype for the individual shielding of the MaPMTs consisted of a 30 mm wide and 60 mm long square tube with a wall thickness of 0.9 mm. The shield was placed around the MaPMT and the base, as illustrated in Figure 5.14. To test whether the single shield would possibly start to saturate, measurements were carried out with a second shield of the same thickness placed around the first.

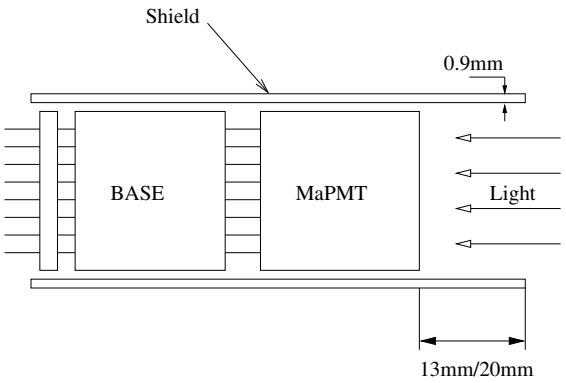

Figure 5.14: *The μ-metal shield around the MaPMT and base.*

The influence of the photocathode position within the shield has been studied for a recess of 20 and 13 mm with respect to the end of the shield. The measurements taken with a recess of only 13 mm were directly comparable with the measurements taken in [20] and are closer to a preferred solution for a final system. In that system the single base will be replaced by a bleeder board serving several MaPMTs so that the individual shields around the MaPMTs have to end at the rear side of the MaPMT.

5.4.2 Global Signal Fraction

Measurements have been made for the "old" (9C20A2) as well as the "new" (9K20C3) focusing type. Data were taken for the most critical case of longitudinal magnetic fields.

The measurements are summarised in Figures 5.15 and 5.16 for the "old" and "new" tube respectively in the case of an unshielded MaPMT as a reference, in the case of the application of a single shield and finally for the additional application of a second shield. The MaPMT with the new focusing layout (9K20C3) is slightly more sensitive than the old type (9C20A2), e.g. at ± 10 mT the signal fraction for the old and new type is reduced to $\approx 60\%$ and $\approx 50\%$, respectively. The difference in sensitivity also vanishes when an individual μ-metal shield is applied. In both cases, a signal fraction of $\approx 60\%$ is found for magnetic fields of ± 20 mT and the two types behave similarly up to ± 10 mT. For the case of a 13 mm recess, the limit of a 10% drop in the signal fraction is reached at about ± 8 mT. For the case of a 20 mm recess this limit is reached beyond ± 10 mT. At ± 10 mT the signal fraction drops by about 5%.

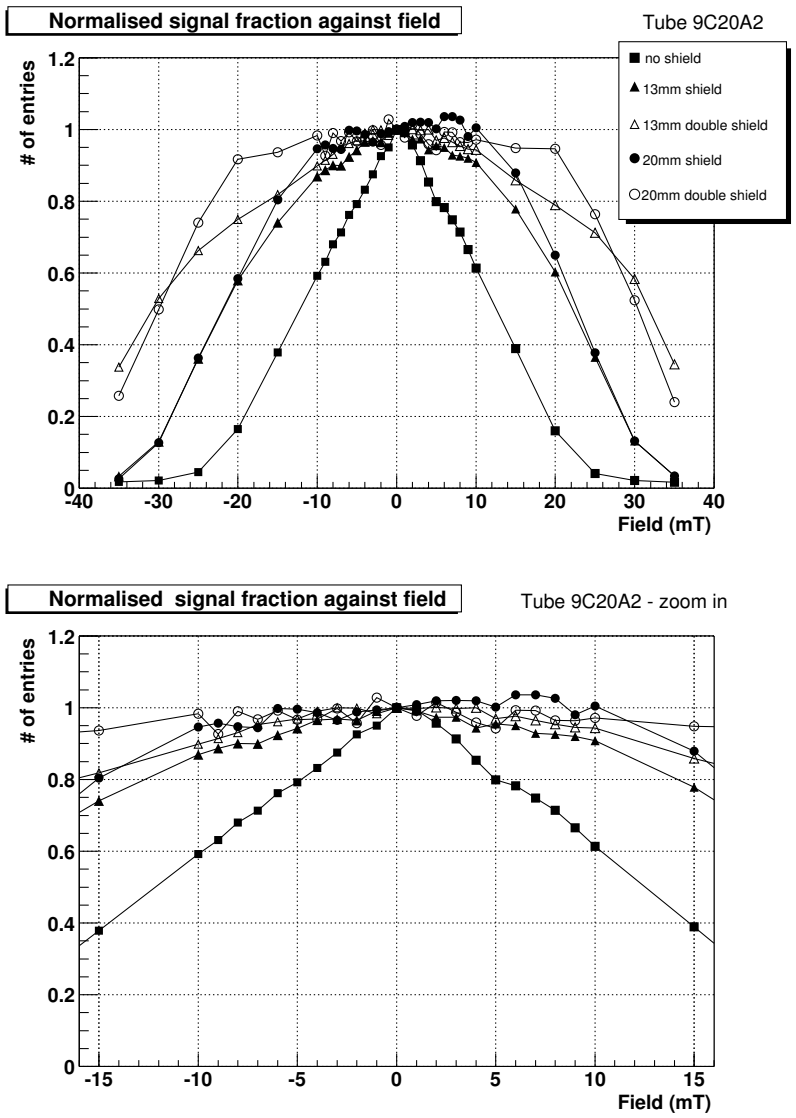

Figure 5.15: *Normalised signal fraction for tube 9C20A2 with and without shielding as a function of the magnetic field, for the full range (top) and zoomed into the $\pm 15\,mT$ range (bottom).*

By applying a second sheath of μ-metal one increases the magnetic flux which can be drawn away from the position of the MaPMT and thus one extends the range of fields under which it can be operated. As the second shield has a larger diameter it should be less efficient than the first shield. This is visible in Figure 5.15. No significant difference is found in the range $\pm 10\,\mathrm{mT}$ where the first sheath already provides efficient shielding. Beyond that the second sheath improves the total shielding power but it does not double the range for which a certain level of signal fraction can be achieved.

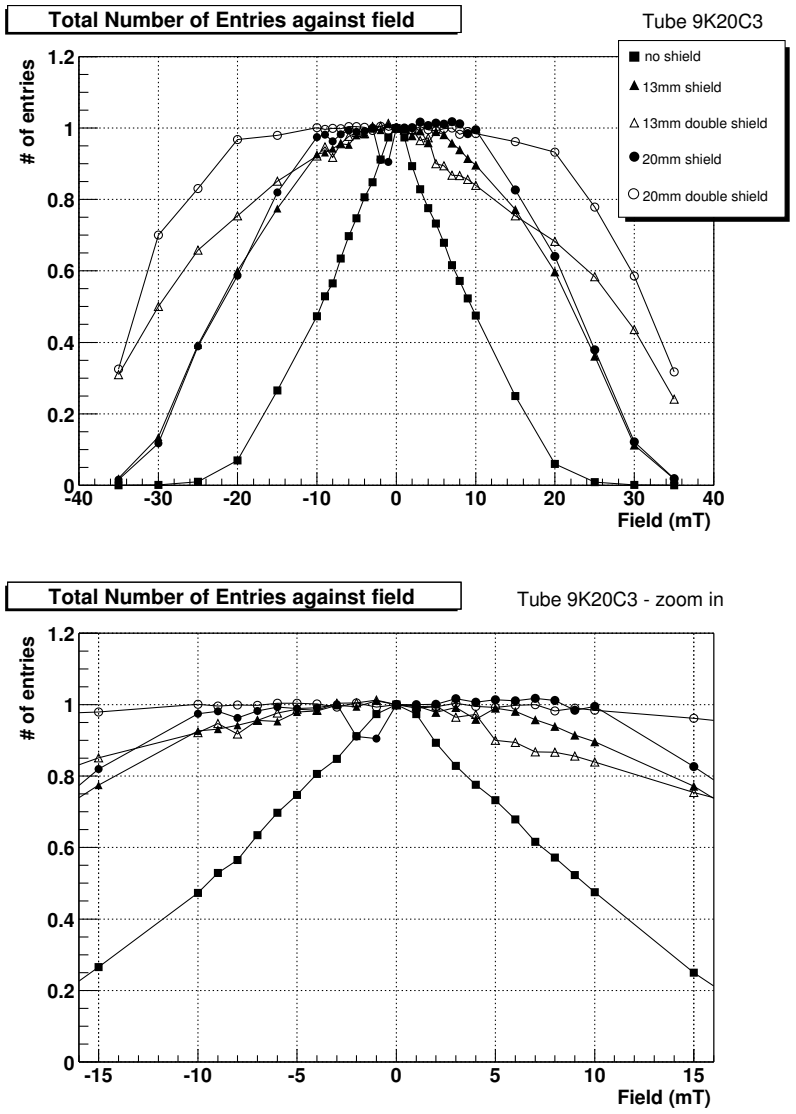

Figure 5.16: *Normalised signal fraction for tube 9K20C3 with and without shielding as a function of the magnetic field, for the full range (top) and zoomed into the ±15 mT range (bottom).*

In the interesting region of fields within ±10 mT the positive effect of a recess of 20 mm in comparison with a recess of 13 mm is much more favourable than the addition of extra shielding material. Only if the environment provides fields beyond ±10 mT would thicker shields have to be incorporated to the design of the RICH photodetectors.

5.5 Conclusions

MaPMTs are most sensitive to external magnetic fields perpendicular to the entry window. Compared to that the sensitivity to magnetic fields along the perpendicular axes is small. The loss of signal fraction is below 10% for magnetic fields up to 20 mT (200 G) and can be neglected. The loss of signal in the longitudinal field is predominantly due to electrons lost between the photocathode and the entry window of the dynode structure. A smaller fraction is lost due to a reduction in signal gain, i.e. electrons lost further down the dynode chain. The signal loss is not uniform over the sensitive area of the tube. The most affected channels are the top and the bottom rows of the tube (Hamamatsu channel labelling). No signs were found for spill-over induced by the magnetic field.

By requiring a maximum average signal loss of 10 % MaPMTs need shielding for longitudinal magnetic fields equal or larger than 2.0 mT. However, the centre rows are quite insensitive to magnetic fields up to 5.0 mT and most of the losses are in the top and bottom rows which are already sensitive to magnetic fields of 1.0 mT. The magnetic field integral at the photodetector plane of RICH1 is expected to be 2.5 mT and MaPMTs hence need μ-metal shielding to stay below the average 10% required loss. Efficient shielding of the MaPMT can be provided with a 0.9 mm individual μ-metal shield and the operational range of the tubes can be extended to higher magnetic fields. With a recess of the MaPMT window of 13 mm the average signal loss stays below 10% up to about $\pm$8 mT. With a recess of 20 mm the operational range can be extended even more to about $\pm$12 mT, and the signal loss is significantly reduced compared to the case of a 13 mm recess. If the MaPMTs needs to be operated in an environment beyond $\pm$10 mT additional μ-metal should be foreseen to draw away more of the magnetic flux, e.g. twice the wall thickness for magnetic fields up to about $\pm$20 mT.

Chapter 6

MaPMT shielding Optimisation Using Finite Element Analysis

The study detailed in Chapter 5 demonstrated the feasibility of protecting Multianode PhotoMultipliers Tubes (MaPMTs) using shielding for magnetic fields up to 2 mT. The μ-metal shield was 60 mm long and 0.9 mm thick using a 13 mm and 20 mm extrusion from which the 13 mm was shown to be sufficient. It was foreseen to mount the photodetectors on the RICH system in arrays of 4×4 MaPMTs as shown in Figure 6.1, in which a grid of μ-metal sheets will be made an integral part of the structure. A Finite Element Analysis (FEA) is attempted to optimise the length of the shield and to establish the behaviour of the shielding when mounted in arrays. After a brief introduction to FEA, the validity of the simulation is verified. The optimum single shield length is studied before investigating two solutions for the case of a wider shield for the 4×4 MaPMT array.

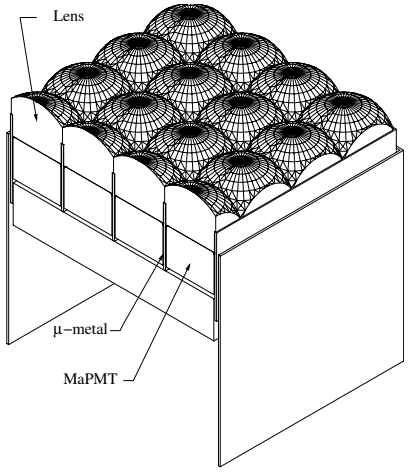

Figure 6.1: *A 4×4 MaPMT module mounted with lenses and showing the shielding separations in a cut.*

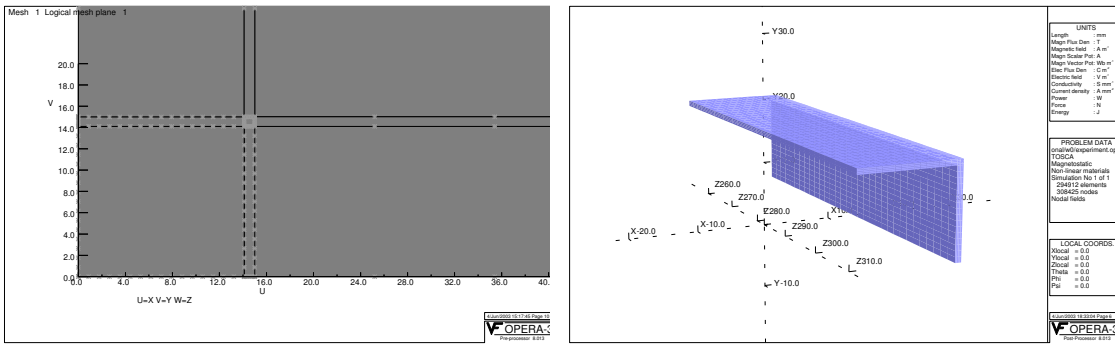

Figure 6.2: *One quarter OPERA simulation of the shield: Left: base plan cut with the sub-divisions from which the shield is extruded to form the one quarter 3D structural view shown on the right.*

6.1 About FEA and OPERA8

The Finite Element Analysis method (FEA) is based on the division of a model into smaller volumes (finite elements) in which the relevant phenomenon can be described in terms of simple equations. Conditions at nodes where elements meet are simplified using boundary conditions forming so called nodal shape functions usually expressed in terms of the local coordinate system of the element for further simplification. These functions are then used as a basis for alternative procedures such as least squares or variational methods which can be used to solve Maxwell's equations. The strength of the method is its flexibility as elements can have various shapes to adapt to any geometry.

The analysis has been conducted with the commercial software package OPERA8 [55] which includes a pre-processor and a post-processor to solve the equations.

The pre-processor is used to define the volumes of the geometry. The user first defines a base plane, Figure 6.2 (left), from which the volumes are extruded to create a mesh, Figure 6.2 (right). The smaller the volumes the better the accuracy but also the more computing time intensive the analysis is. Hence meshing is always a work of compromise in which the user decides where the accuracy can be traded. Boundary conditions defining the direction of the field are then applied in order to release the work of the post-processor. This is essential in order to easily link magnetic materials carrying source currents (the shield) and the other volumes (air). Another way to improve speed is to consider the symmetry of the system, hence the models treated here are one quarter simulations where

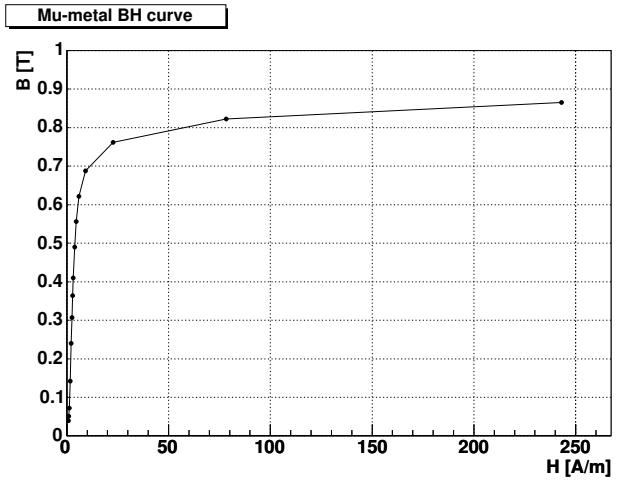

Figure 6.3: *Magnetisation (BH) curve of the μ-metal used for the simulation showing the change in the magnetic field as the field magnitude (flux density) inside the metal increases [36].*

the symmetry is applied at the level of the post-processor.

Once the model has been defined it is treated by the post-processor TOSCA, which solves Maxwell's equations according to the values of the external fields and symmetry conditions that have been set.

6.2 Experimental Validity

The validity of the simulation has been verified for a OPERA8 representation of an actual shield placed in a quasi-Helmholtz coil[1].

6.2.1 The Experiment

The experimental setup shown in Figure 6.4, consists of the quasi-Helmholtz coil in which the μ-metal shield is placed. The shield is the same as used in Chapter 5: the 0.9 mm thick sheath is 30 mm wide and 60 mm long. Although care has been taken for the alignment, the misalignments between the sliding bridge, the coil support, the holding arm and the shield can be estimated to be of the order of 2 mm at most.

[1]The separation between the two coils was not exactly one coil radius.

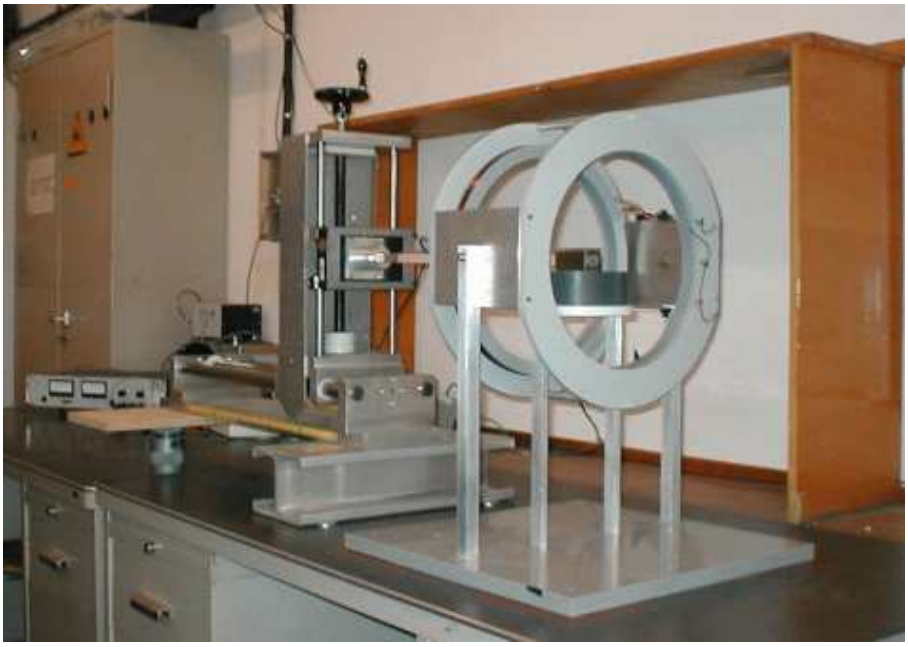

Figure 6.4: *The experiment with the shield placed at the centre.*

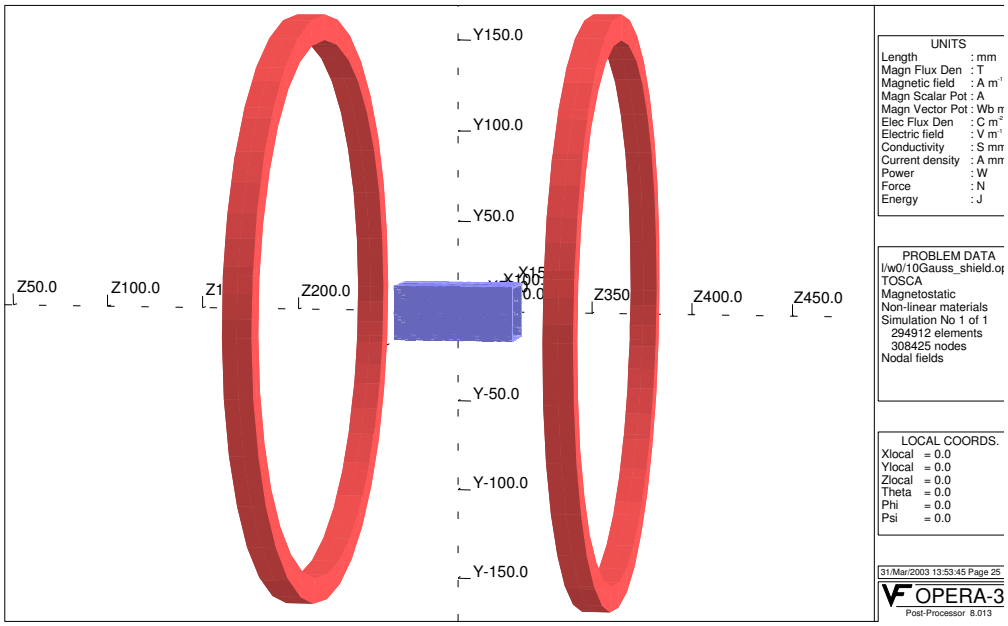

Figure 6.5: *The OPERA8 simulation showing the Helmholtz coil and the shield at the centre.*

6.2.2 OPERA Simulation of the Experiment

The simulation consists of two coils and a μ-metal shield. Only one quarter of the shield has been drawn to take advantage of the symmetry in order to minimise the computing time at the post-processor level.

At the pre-processor stage, the shield is extruded from a 464×464 mm base plane shown in Figure 6.2. The shield is made from three facets and the remaining defines the plane. The properties of the metal are set by the magnetisation curve, shown in Figure 6.3, which defines how much flux density, B, results from an increase in flux intensity, H. The sub-divisions were defined as follow: on the base plane the number of sub-divisions for the μ-metal facets have been set to 16 with the top corner defined to 4. The rest of the plane was set to 44. For the extrusion the first layer was divided into 20 divisions, the second containing the μ-metal shield into 32 and the third into 20.

Each coil was made with two demi-arcs. In OPERA the coils are made of one conductor instead of several loops. The induced magnetic field is defined by the current density applied. It has been determined using the approximate value for a Helmholtz coil's magnetic field B and the definition of the current density j for a coil carrying a current I around N circles of radius R and with a cross section (x,y,z) as defined in equation 6.1

$$B = \frac{8\mu_0 N * I}{R\sqrt{125}} \qquad j = \frac{N * I}{xy} \Longrightarrow \frac{B * R\sqrt{125}}{8\mu_0 x^2} \tag{6.1}$$

In our case, x and y are equal. The study has been carried out for three fields, 10 G, 20 G and 30 G being the maximum field allowed by the experiment. For a radius of 157 mm and a cross section of 2 mm the corresponding current densities and OPERA8 magnetic field values are summarised in Table 6.1.

B field	j (OPERA8)	B Field (OPERA8)
10 G	0.4365 A.mm^{-2}	10.06 G
20 G	0.8729 A.mm^{-2}	20.11 G
30 G	1.3090 A.mm^{-2}	30.17G

Table 6.1: *Current density (j) values used for the definition of the OPERA8 coils for a given magnetic field.*

Figure 6.7 shows the resulting magnetic field map for a cross section along the side of the shield and through the middle along the longitudinal plane of the z-axis, as defined in Figure 6.5. The B field decreases as it is absorbed in the shield metal until it passes the middle of the sheath. After that point the field increases again as it escapes the shield.

6.2.3 Comparison of the Experiment vs the Simulation

In the case of the experiment, measurements of the axial magnetic field have been taken every 2 mm along the central axis (z-axis) for magnetic fields of 10 G, 20 G and 30 G at the centre of the coils. The result for a 20 G magnetic field is shown in Figure 6.8. Without shield the simulation agrees very well showing that the calculation of the current density was accurate enough to determine the magnetic field distribution. Once the shield is placed, there is still a good agreement inside the shield. One can see a slight misalignment of the μ-metal shield. However, there is a difference in amplitude outside the shield but the shapes between data and simulation agree. This can be caused by the difference between the perfect coils and the one in the experiment and hence is not a cause of concern. Comparative results for 10 G and 30 G are shown in Appendix B.

6.3 Single Shield Length Optimisation

Two single shields of different lengths have been experimentally tested with an MaPMT: a 40 mm long and a 33 mm long shield. As illustrated in Figure 6.6, the lengths have been chosen so that the MaPMT glass window is situated at the centre of the shield: 20 mm for the 40 mm long and 13 mm for the 33 mm long shield. The aim of the following study was to determine what the optimum size of the shield was in order to allow for a protection similar to the 60 mm long shield. Single shields of 60, 40 and 33 mm lengths in an ambient longitudinal (z-axis) magnetic field of 20 G have been simulated. The simulations are all very similar.

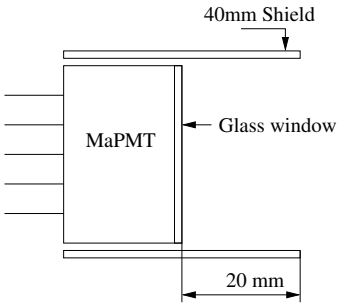

Figure 6.6: *Sketch of the MaPMT within a 40mm long shield.*

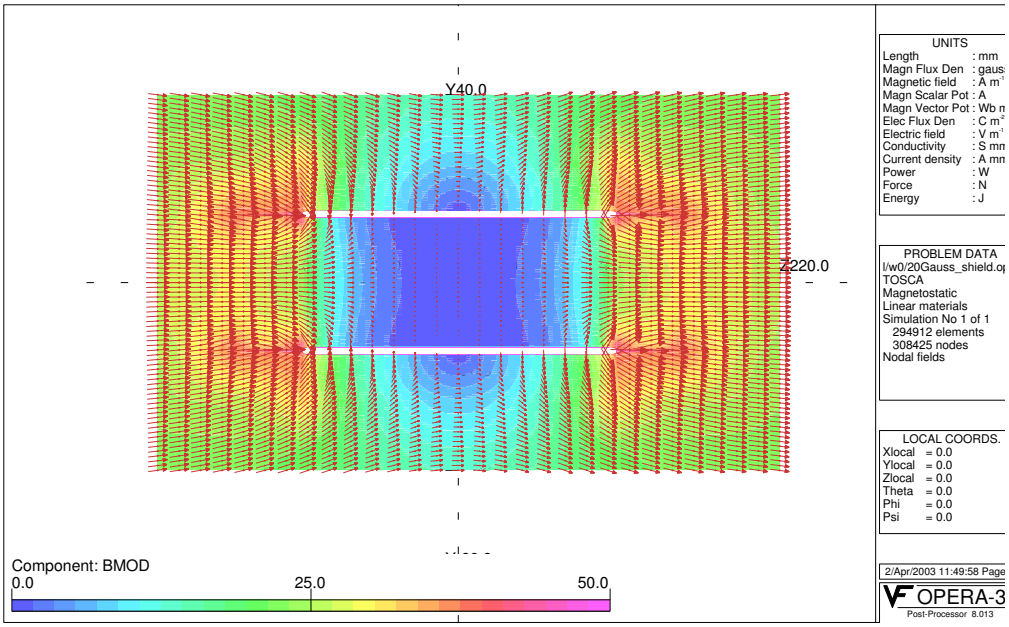

Figure 6.7: *Field map of the z-component of the magnetic field for a cross section of the μ-metal shield along the side and through the middle for the longitudinal plane of the z-axis. The ambient magnetic field is 20 G,*

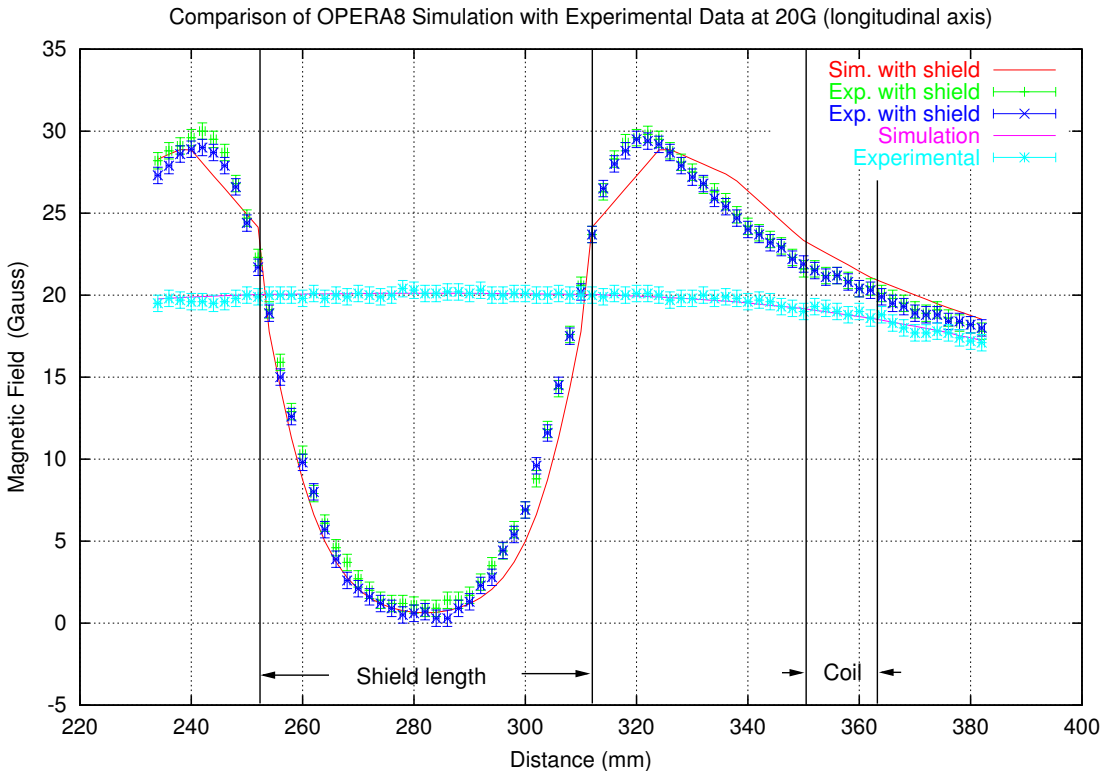

Figure 6.8: *Comparison of OPERA8 results with the experiment for 20 G.*

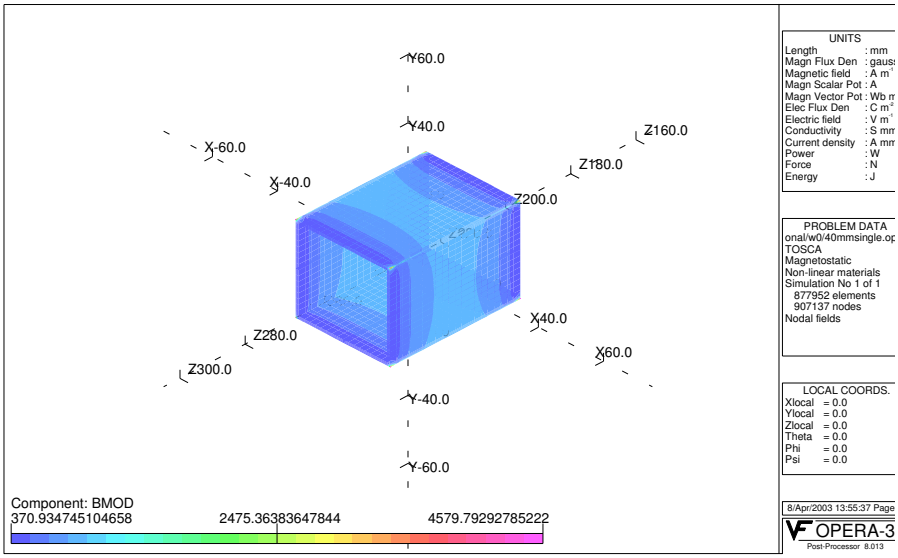

Figure 6.9: *OPERA8 3D view of a 40 mm long μ-metal shield in a longitudinal (z-axis) magnetic field of 20 G showing the magnetic field in the material.*

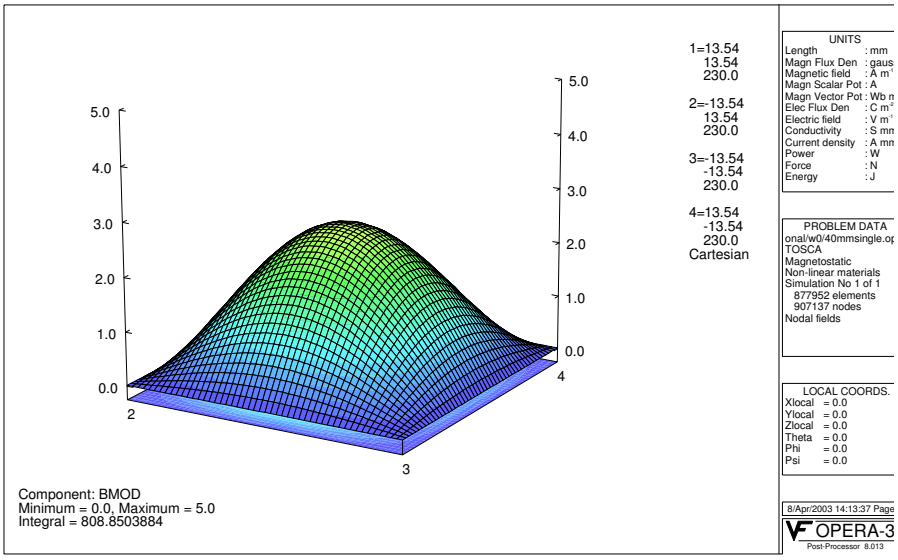

Figure 6.10: *Field shape inside the 40 mm shield at the 13 mm recess for a ambient magnetic field of 20 G.*

They use the symmetry of the shield to compute only one quarter of the geometry in the volume. The model is then extruded according to the length of the shield keeping the air volume which forms the boundaries identical. The three simulations have been compared for several positions away from the front of the shield where the glass window would be. These are 13 mm, 20 mm and in the middle of the shield in the z direction. The field has been taken for a slice inside the shield forming a square surface across the x-axis as illustrated in Figure 6.10 for the 40 mm shield shown in Figure 6.9.

Shield length	13 mm cut	20 mm cut	Middle cut
60 mm at 20 G	4.9 G	1.7 G	0.6 G
60 mm at 150 G	40.8 G	24.7 G	25.1 G
40 mm at 20 G	4.5 G	2.65 G	
40 mm at 150 G	33.8 G	19.9 G	
33 mm at 20 G	5.0 G	N.A.	4.3 G
33 mm at 150 G	37.6 G	N.A	32.3 G

Table 6.2: *Maximum simulated magnetic field values inside an individual single shield.*

The maximum values obtained for different configurations are listed in table 6.2 and allow us to draw the following conclusions:

- The 33 mm shield performance is comparable to the 13 mm cut on the 60 mm shield.
- The 40 mm shield in the middle is worse than the 60 mm long shield but it is better than the 13 mm cut on the 33 mm shield.
- The 40 mm shield at 13 mm is comparable to the 13 mm cut on the 60 mm shield.

6.4 4×4 MaPMT with a Wide Shield

A solution to shield a 4×4 MaPMT array is to use a shield as wide as the array as illustrated in Figure 6.11. The FEA analysis has been carried out by varying the length and the width of the shield for a ambient longitudinal (z-axis) magnetic field of 20 G. The maximum magnetic field values were then analysed at the middle and at the MaPMT plane, 20 mm inside the shield as if mounted with the lenses.

Shield (length/thickness)	Centre plane	MaPMT plane
40 mm / 0.9 mm	16.6 G	
40 mm / 1.8 mm	16.5 G	
75 mm / 1.8 mm	11.3 G	12.8 G
100 mm / 1.8 mm	8.0 G	12.0 G
150 mm / 1.8 mm	3.7 G	14.0 G
200 mm / 1.8 mm	1.6 G	16.4 G

Table 6.3: *Maximum magnetic field values inside a 4×4 MaPMT array wide shield in an ambient longitudinal magnetic field of 20 G.*

As shown in Table 6.3 displaying the results, a 40 mm long and 0.9 mm thick shield is not viable anymore. Doubling the thickness does not make any significant difference and the length of the shield has to be of the order of 150 mm before reaching values similar to the small individual shield solution.

6.5 4×4 MaPMT with a 4×4 Shield Array

The feasibility of using an array of μ-metal instead of a wide shield covering all MaPMTs has been simulated for a 40 mm and a 33 mm length with a 0.9 mm thickness for the case of a longitudinal field. The simulation is shown in Figure 6.12. Table 6.4 shows the magnetic field strengths obtained for the three positions defined in Figure 6.12. For a longitudinal field of 20 G, the central values are similar to the case of a single individual shield while the values at 150 G are smaller. An ambient transverse field of 20 G has also been simulated and values do not exceed 2 G. Hence one concludes that the 4×4 shield array is as capable as the single individual shield with the same lengths and provides adequate protection.

Shield	Position 1	Position 2	Position 3
40 mm at 20 G	2.25 G	2.11 G	1.97 G
33 mm at 20 G	3.75 G	3.55 G	3.37 G
40 mm at 150 G	16.90 G	15.85 G	14.80 G
33 mm at 150 G	17.87 G	26.63 G	25.08 G

Table 6.4: *Maximum magnetic field values at the centre of a 4×4 shield array in a longitudinal field for positions defined in Figure 6.12*

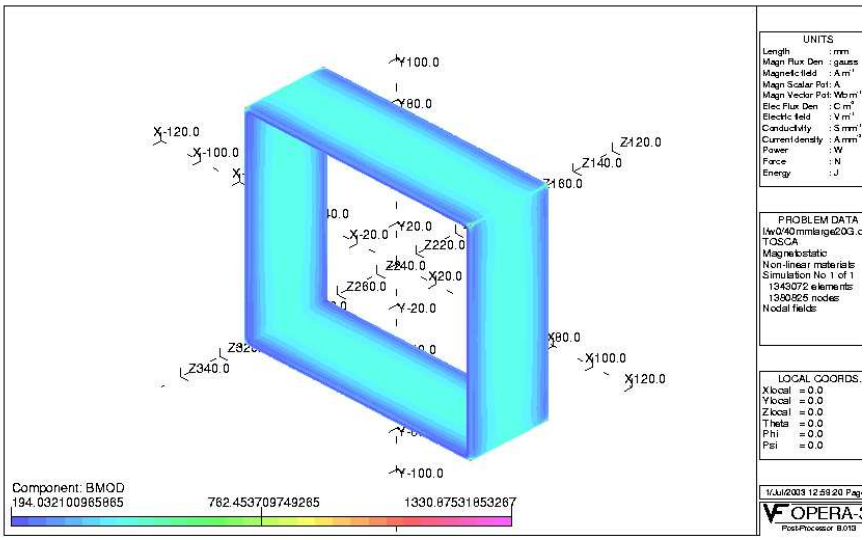

Figure 6.11: *OPERA8 3D view of a 40 mm long and 1.8 mm thick wide shield in a 20 G longitudinal (z-axis) magnetic field showing the magnetic field inside the material.*

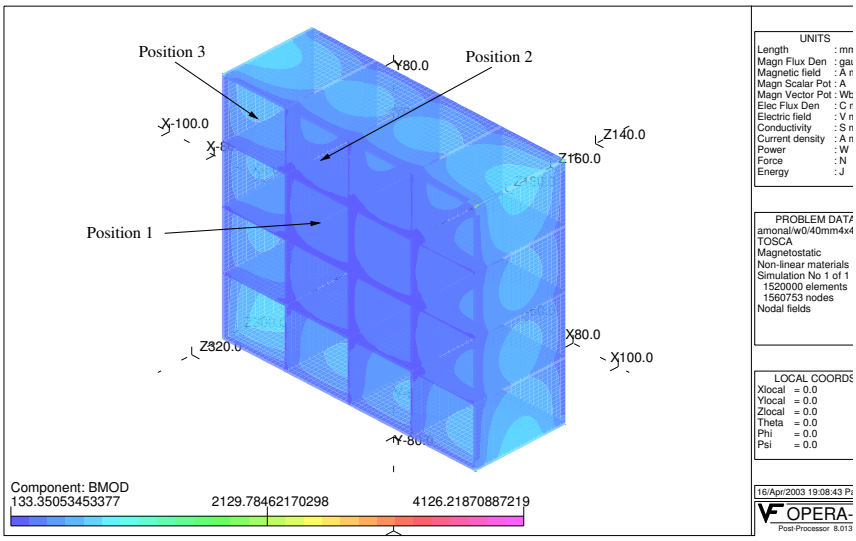

Figure 6.12: *OPERA8 3D view of a 40 mm long shield array in a 20 G longitudinal (z-axis) magnetic field showing the magnetic field inside the material.*

6.6 Conclusions

The requirement to protect the MaPMTs from magnetic fields of 2 mT (20 G) implies that the field on the MaPMT window should not exceed 0.5 mT (5 G) within the shield as shown by table 6.2.

The FEA simulation showed that a 33 mm long single shield provides adequate protection. However, the 40 mm long shield is preferred as the MaPMT would be placed further away from edges effects visible in Figure 6.4. The use of a wider shield for a 4×4 array of MaPMT would be viable with a length over 100 mm. The shield array is better than the wide sheath as it is directly comparable to a single individual shield. As a result two shield array prototypes of 33 mm and 44 mm have been built to be experimentally tested. At this time, the decision to go with the HPD solution as photodetectors for the LHCb experiment, instead of the MaPMT, meant the closure of the project and no further tests have been carried out.

Chapter 7

MaPMTs Testbeam Performances

The performances of MaPMTs were measured in a testbeam which showed their viability as photodetector for the LHCb experiment [20]. However at the time the MaPMTs were read out using the custom electronics described in Chapter 5 which did not fulfil the LHCb requirements for standardisation. In the previous chapter we showed that the MaPMT passed the magnetic constraints. The next step was to study the MaPMT response using the actual electronics specially developed to accommodate the 40 MHz read out in the high radiation environment of the LHCb experiment.

The following analysis presents the performance of a 3×3 array of 8-dynode stage MaPMTs equipped with lenses in a testbeam at CERN. In a first step the detected number of photons per event is determined from a testbeam simulation. The simulation is then compared to the testbeam results.

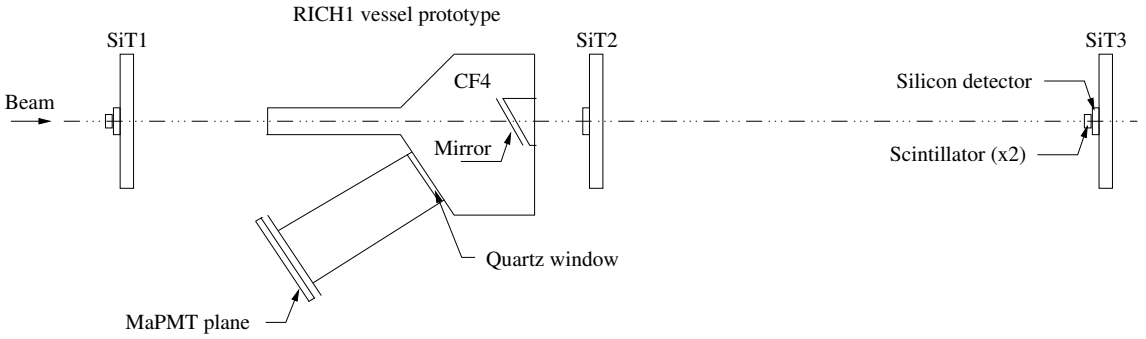

Figure 7.1: *Sketch of the testbeam layout showing the three Silicon Telescopes (SiT1, SiT2, SiT3) and the RICH1 prototype with the MaPMT array plane.*

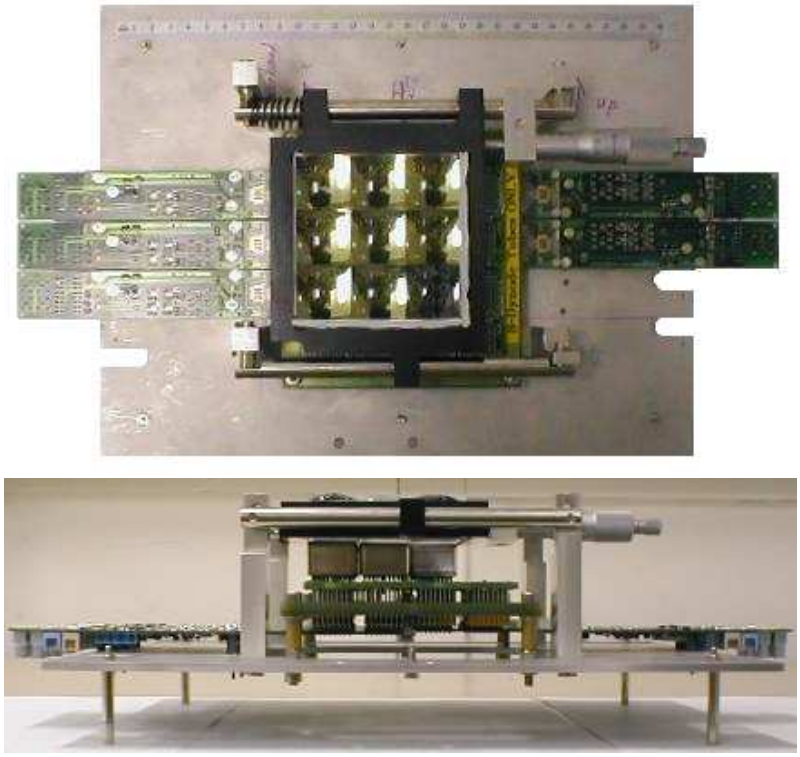

Figure 7.2: *The 3×3 array of MaPMTs mounted with lenses and equipped with five Board Beetle readouts. The MaPMT plane is visible on the top picture. One of the MaPMTs (bottom right) was missing. A side view is shown on the bottom picture.*

7.1 Testbeam Description

7.1.1 Experimental Setup

The MaPMTs have been experimentally tested at the T9 PS beam facility of CERN. The pion particle beam had a momentum of 10 GeV/c with an electron contamination of about 5%. The experimental setup is shown in Figure 7.1. The beam trajectory was monitored using three silicon detector telescopes segmented into a 22×22 matrix of square pixels with a pitch of 1.3 mm. The read out was provided by twelve (four per telescope plane) 128-channel amplifier-shaper-multiplexer chips (Viking VA2 ASIC) [58]. The RICH1 prototype [20] consists of a CF4 gas vessel with a 1 m long and a 90 mm cross section forward arm from which the particles enter. The radiated Cherenkov photons are then diverted out of the acceptance towards the photodetector using a spherical mirror tilted by 18° with respect to the beam axis. The aluminised-glass mirror has a reflectivity of 90% at 600 nm, a diameter of 112 mm and a focal length of 1117 mm. Adjustments to the mirrors position

can be made using micrometer screws. The photons are transmitted through a quartz window sealing the vessel and out onto the MaPMT plane situated 1143 mm away.

A close packed 3×3 array of 8-dynode stage MaPMTs equipped with lenses has been tested. The array is shown in Figure 7.2. The MaPMTs are mounted on a bleeder board which provides the mechanical support, the HV and the dynode-chain resistor network together with a feed through pitch to the readout electronics boards. The MaPMTs are readout in pairs using a specially designed "Board Beetle" which provides all the electronics required for the operation of the Beetle chip as shown in Figure 7.3.

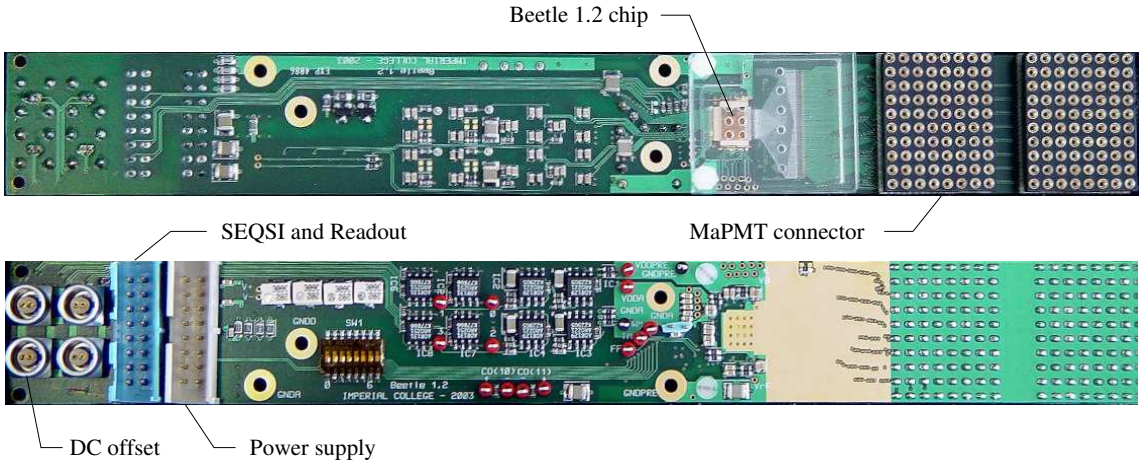

Figure 7.3: *Top and bottom view of the Board Beetle.*

7.1.2 Beetle 1.2 Chip

The Beetle 1.2 chip [59] is a 128 channel pipelined Application Specific Integrated Circuit (ASIC) designed to the LHCb experiment specifications: it is fast and can be operated at 40 MHz, it is radiation tolerant up to 10 Mrad by the use of CMOS sub-micron technology with triple redundant logic. The chip has been designed for several LHCb sub-systems: the Vertex Detector, the Inner Tracker and the RICH. A block diagram of the chip is shown in Figure 7.4. Each channel is amplified with a low-noise charge sensitive amplifier with a optimum signal of 22 000 e^- or one Minimum Ionising Particle (MIP)[1] for a total dynamic range of 10 MIPs.

[1] A MIP is the standard reference for the signal of silicon detectors

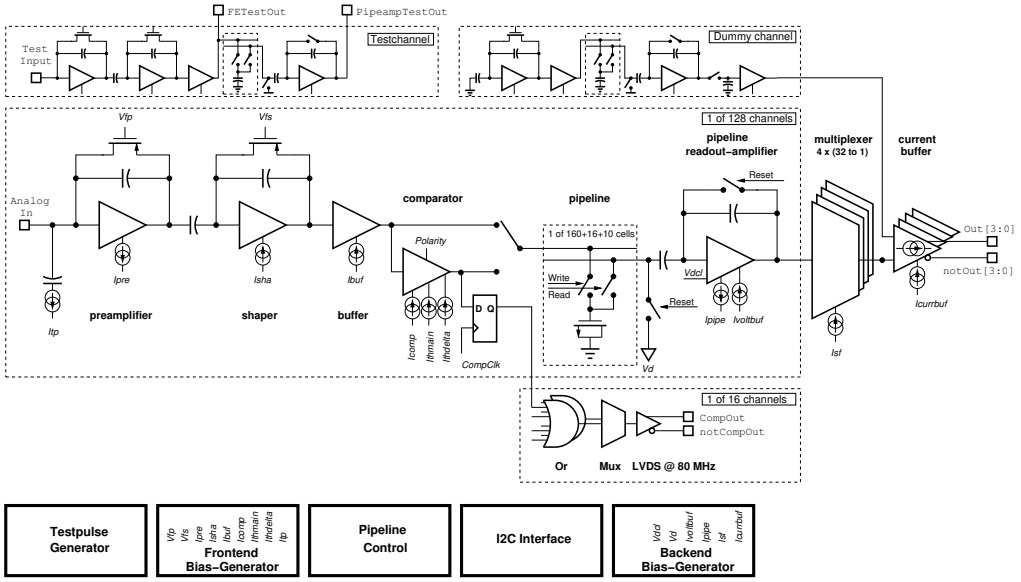

Figure 7.4: *A block diagram of the Beetle 1.2 chip [59].*

The 8-dynode stage MaPMT has an amplification of $50\,000\,e^-$ at 800 V which fits the dynamic range without the need of any level adjuster. The chip can either be used as an analogue pipeline chip or in a binary mode in which case it can operate at up to 80 MHz allowing to extend its use to other potential experiments. Here it is only used in analogue mode. All digital controls and data signals are low voltage differential signals (LVDS) and the chip is programmable via a standard I2C interface. The chip is mounted on the Board Beetle.

The Beetle1.2 chip can not directly read 12-dynode stage MaPMTs. The additional dynode-stages provide a high amplification which requires level adjustment within the Beetle1.2 chip itself. Hence a modified chip, the Beetle1.2MA0, for the use of 12-dynode stage MaPMTs has been designed.

7.1.3 Data Acquisition Setup

The data acquisition and control is a VME based system, shown in Figure 7.5. Most of its major components have been described in Chapter 4. The nine MaPMTs are mounted on the Bleeder board which distributes the high voltage. The six Board Beetle are connected to the back end, each reading out two MaPMTs. The controls and data are interfaced with a single board which distributes the trigger signal and the data frame to the appropriate

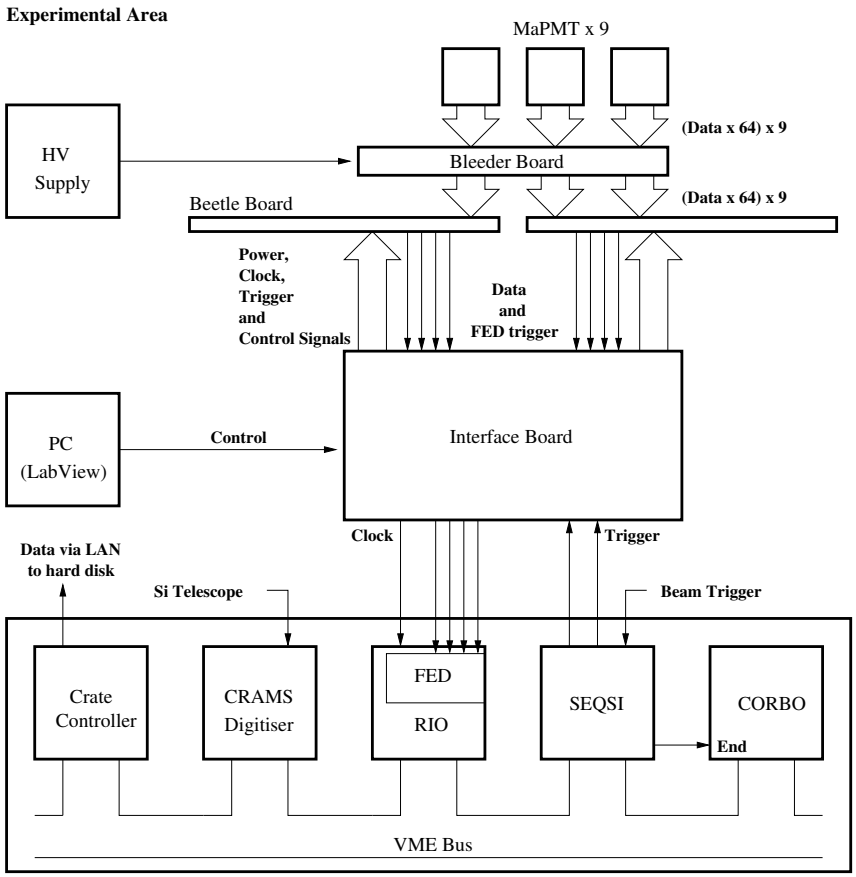

Figure 7.5: *A block diagram of the electronics readout and data acquisition systems.*

hardware. Note that the interface board was not ready on time for the testbeam and a customised interface had to be made. The interface board is driven via a LabView PC interface. In the testbeam the trigger is provided by a particle beam as it goes through two overlaying scintillators plates mounted on the silicon telescopes. A Cherenkov counter placed upstream of the first silicon telescope is used to reject electrons. When the SEQSI receives the signal it sends clock cycled triggers to the Board Beetle and the FED. The FED returns the Board Beetle data and the SEQSI notifies the CORBO. The CORBO then sends an interrupt signal to the RIO, which is basically a embedded PC, that reads out the data and empties the FED pipeline. Finally data from the Board Beetle and the silicon telescopes are saved to disk via the Crate Controller.

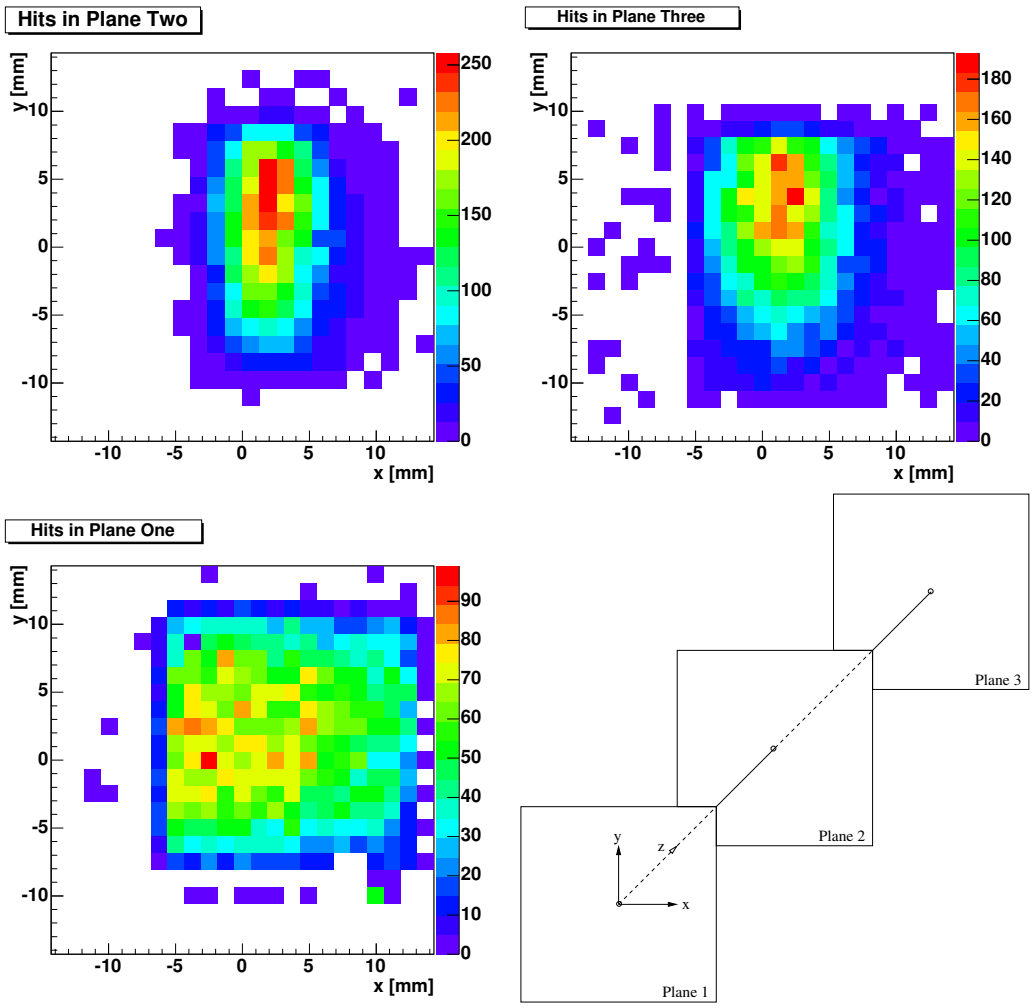

Figure 7.6: *Cumulated hits events in the silicon telescope planes as the beam passes through. Bottom left corner is the first plane (SiTel1) as defined in Figure 7.1, top left is SiTel2 and top right is SiTel3. Bottom right shows the coordinate system where the beam is going along the z-direction.*

7.2 Beam Divergence

The particle beam does not arrive perfectly aligned to the axis of the radiator. It traverses at a small angle with respect to the reference axis. The beam trajectory varies from event to event and this divergence has to be accounted for. Trajectories can be monitored using the data registered by the silicon telescope and by fitting a straight line to each hit in the three silicon planes. The divergence from the reference point can then be evaluated. A code developed for the HPD testbeam [34] has been adapted to the configuration of the MaPMT testbeam. In a first step, clusters of four pixels are identified. Events in which

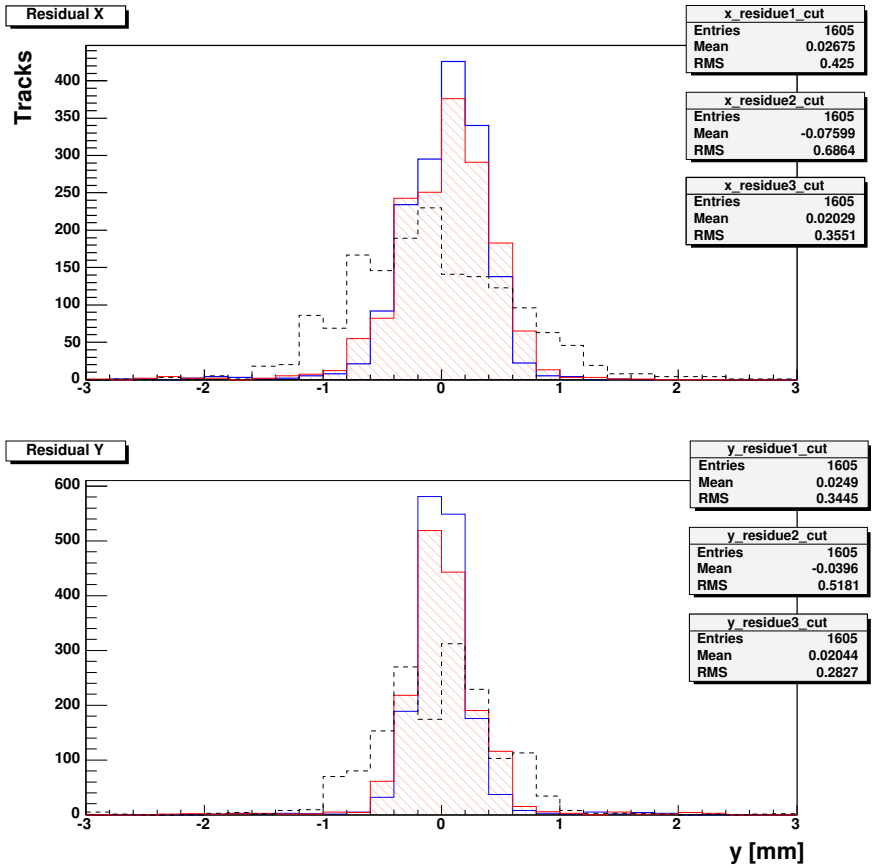

Figure 7.7: *Residuals to the fitted beam trajectory to silicon hits per clusters. Residual1 corresponds to plane 1 (blue), residual2 to the second plane (red dashed area) and residual3 to the third (dashed line).*

clusters are greater than four pixels are rejected. Events are only kept when a single cluster is found with a hit in each of the three silicon planes. An actual hit position is obtained from the ADC weighted centre of gravity of the cluster. It is then converted into a metric position using the pixel pitch of 1.3 mm. Figure 7.6 shows the hit positions passing the cluster cut in each silicon telescope plane according to the number labelling of Figure 7.1.

Each event is fitted using a least square method to obtain the best beam trajectory going through each plane. This is done independently for xz and yz according to the coordinate system defined in Figure 7.6. The mean residual to the line going through the three planes, shown in Figure 7.7, is obtained by subtracting the actual hit coordinate to the fitted coordinate. The residual is manually minimised to re-align the hit spectrum for all planes. Finally the divergence is the angle of the tracks with respect to the *z-axis* for x and y. A final cut can be applied by considering only the hits within the central

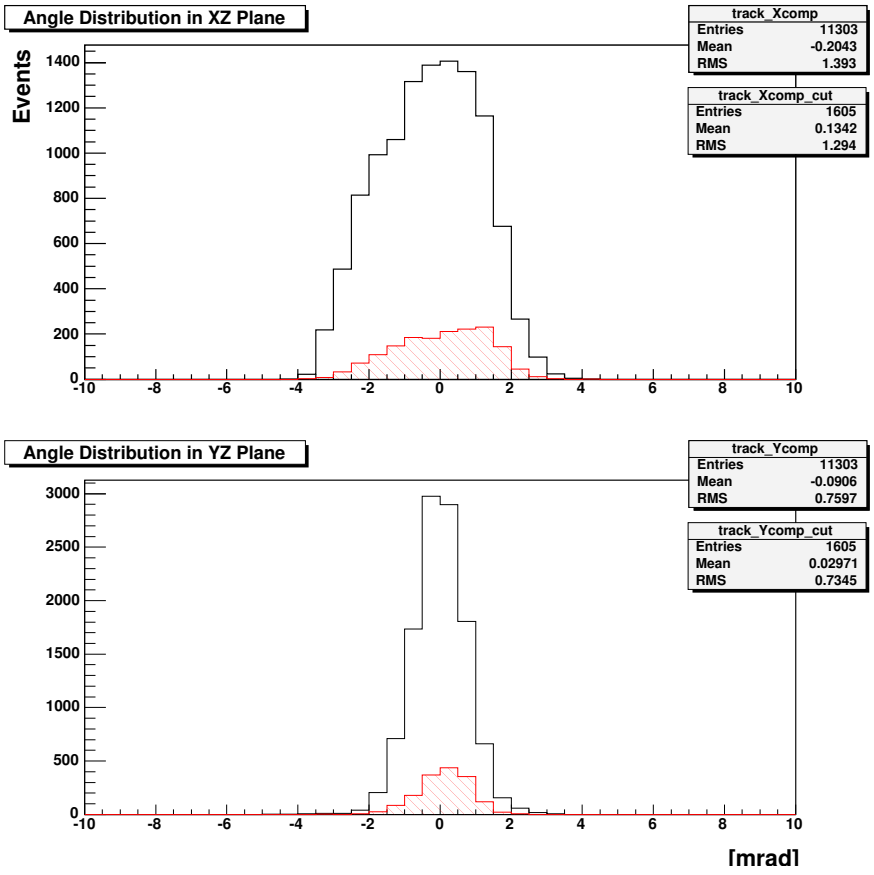

Figure 7.8: *Divergence angles: the dashed regions corresponds to tracks only passing through the centre of plane SiTel2 (within 2 mm).*

region where most of the hits are. As the beam is most focused in plane SiTel2, see Figure 7.6, the cut is applied on that plane, requiring hits within 2 mm around the central region. Figure 7.8 shows the divergence distribution with and without the above cut. The following conclusions can be drawn: 1) using the central region only, the divergence in the x-direction is reduced from 1.39 mrad to 1.29 mrad while it is reduced from 0.76 mrad to 0.73 mrad in the y-direction and 2) the beam divergence is two times bigger in the x-direction.

7.3 Testbeam Simulation

A GEANT4 simulation of the testbeam [56] was implemented. Cherenkov photons are emitted in the radiator arm for a 800 mbar CF_4 gas at a temperature of 300 K. Figure 7.9 shows a single pion event travelling upwards. The emitted Cherenkov photons are

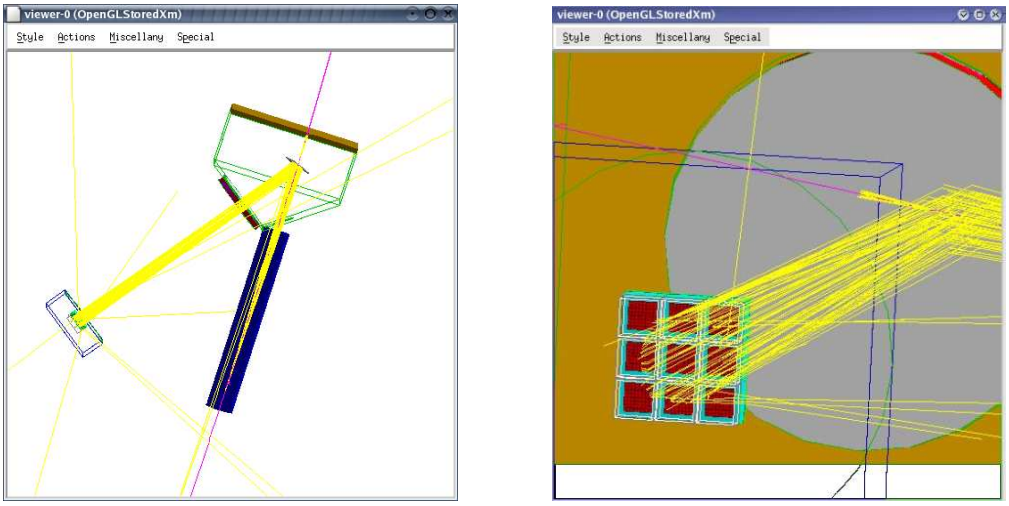

Figure 7.9: *Left: top view of the RICH1 vessel prototype simulated in GEANT4 for a single pion event coming from the bottom of the picture. Right: zoom in showing the Cherenkov photons reflecting of the mirror onto the MaPMT plane.*

then reflected by the mirror towards the MaPMT plane. The MaPMTs are mounted with spherical lenses and hits are registered on the inside of the MaPMT quartz window. The quantum efficiency is assumed for normal incidence and the surface reflection is corrected. There is no simulation of the gain variation from pixel to pixel. Parameters such as the beam divergence can be adjusted.

The results obtained for the beam divergence were used in this simulation. The average number of photon produced for each event was then calculated. Figure 7.10 shows that the photon yield, i.e. the number of expected photoelectrons per event is 6.2. In Figure 7.11 we show the ring for 10 000 cumulated events. The beam divergence is apparent in the thickness of the produced Cherenkov ring. As expected from the previous Section 7.2 the ring is wider at the sides, by a factor two, compared to the thinner top and bottom.

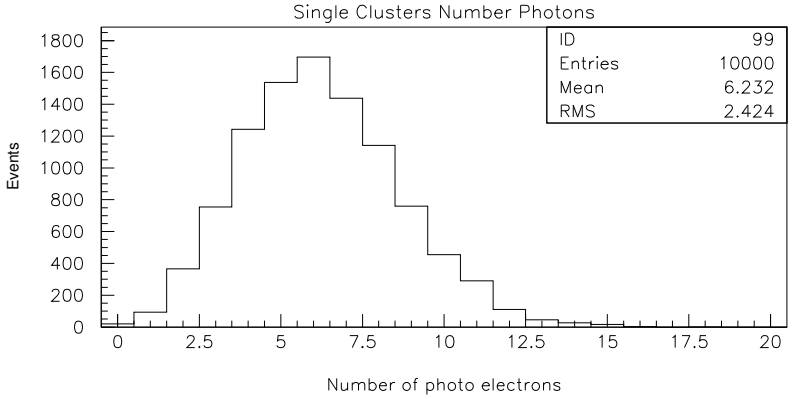

Figure 7.10: *Photon yield distribution for 10 000 events.*

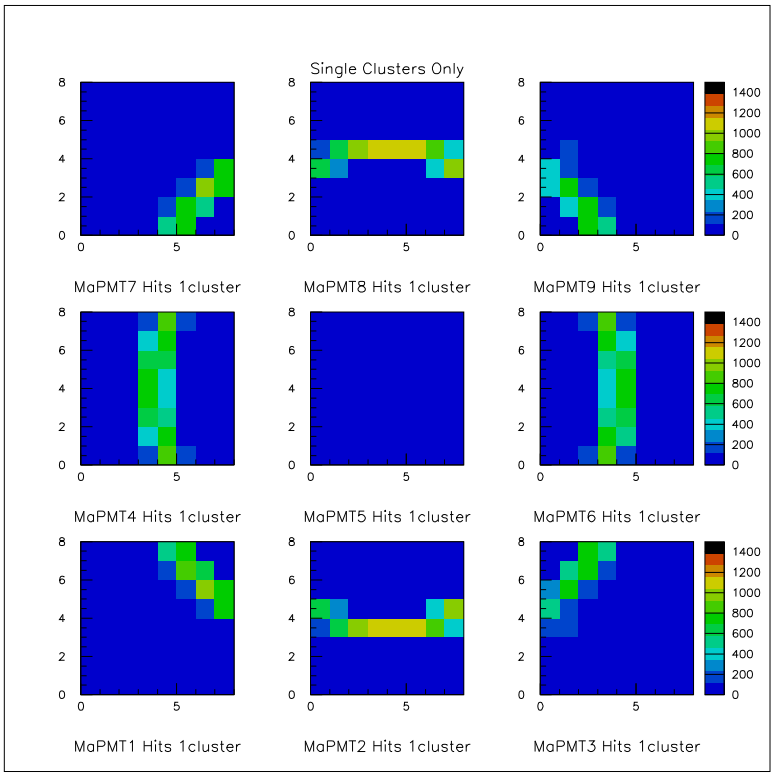

Figure 7.11: *Cherenkov ring obtained for 10 000 events in a CF_4 gas radiator. The divergence of the beam is visible in the sides with a double column of hits.*

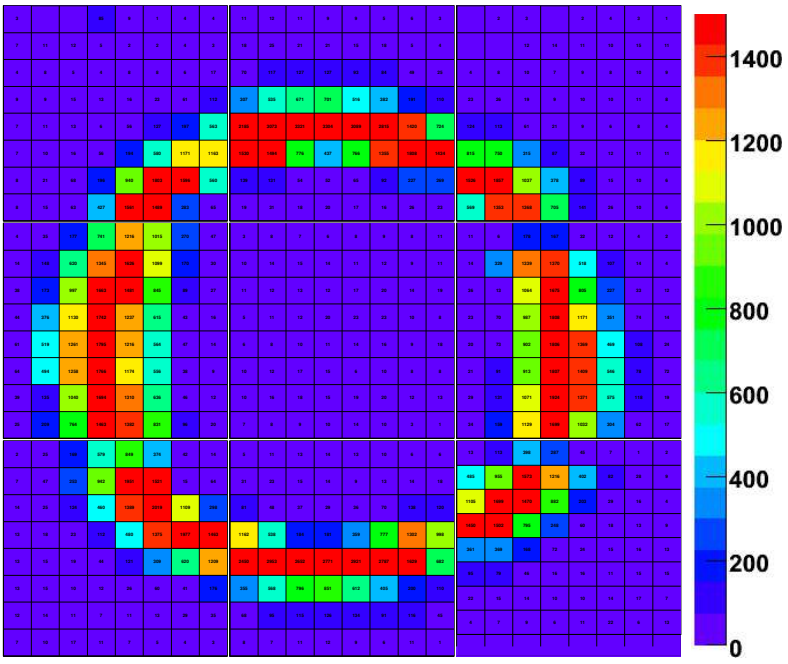

Figure 7.12: *Cherenkov photons ring directly obtained from the testbeam at an MaPMT voltage of -900 V from 16 362 events. Large cross-talk is visible as a wide spread in the ring thickness.*

7.4 Testbeam Analysis

The MaPMTs were operated at different high voltages from -750 V to -1000 V in steps of 50 V for gain studies. Data were taken with beam particles but also with a LED light source shining on all the MaPMTs. The measured pulse height (ADC value) undergoes a common mode correction. A hit corresponds to a corrected pulse height exceeding a 5 sigma cut on the individually fitted pedestal distribution, see Chapter 5. In Figure 7.12 we show the Cherenkov photons recorded from 16 362 events with the MaPMT at -900 V. A Cherenkov ring is clearly visible but there is a major difference with the simulation, in that the Cherenkov ring is a lot wider, specially on the sides. This is due to cross-talk in the electronics of the Board Beetle. The following analysis is aimed at removing the cross-talk to obtain a direct measurement of the photon yield in order to compare it to the simulation.

7.4.1 Cross-talk Identification

The cross-talk was identified using LED runs which provide signals on all pixels. Runs taken with the MaPMT at -1000 V produce the largest cross-talk and hence were used for its identification. Cross-talk is identified by looking at how the pedestal corrected pulse heights H_x of a hit in pixel x and the pulse heights H_y of a hit in pixel y vary together from event to event. This is done by calculating the correlation coefficient C defined as:

$$C = \frac{cov(x,y)}{\sigma_x \sigma_y} = \frac{\overline{(H_x - \bar{H}_x)(H_y - \bar{H}_y)}}{\sigma_x \sigma_y} = \frac{\overline{H_x H_y} - \bar{H}_x \bar{H}_y}{\sigma_x \sigma_y} \tag{7.1}$$

where $\bar{H}_x$ and $\bar{H}_y$ are the mean pulse heights, σ_x and σ_y are the standard deviations. Pulse heights above pedestal in pixel x occurring together with pulse heights above pedestal in pixel y are a sign of cross-talk. As a consequence, C will be positive. Figure 7.13 shows the correlation coefficients between all 64 pixels of an MaPMT. The diagonal shows of course a 100% correlation for the same pixel. The scale of the picture has been set to a maximum of 0.25 in order to emphase cross-talk patterns. A clear pattern emerges: the cross-talk is mostly horizontal, in that pixel 1 talks to pixel 2, pixel 2 talks to pixel 1 and to pixel 3, and so forth. There is also a correlation in the vertical direction for neighbouring pixels. However the coefficient is only 0.05 on average as opposed to between 0.15 and more than 0.25 for horizontal cross-talk. It is also apparent that the horizontal correlation is clustered

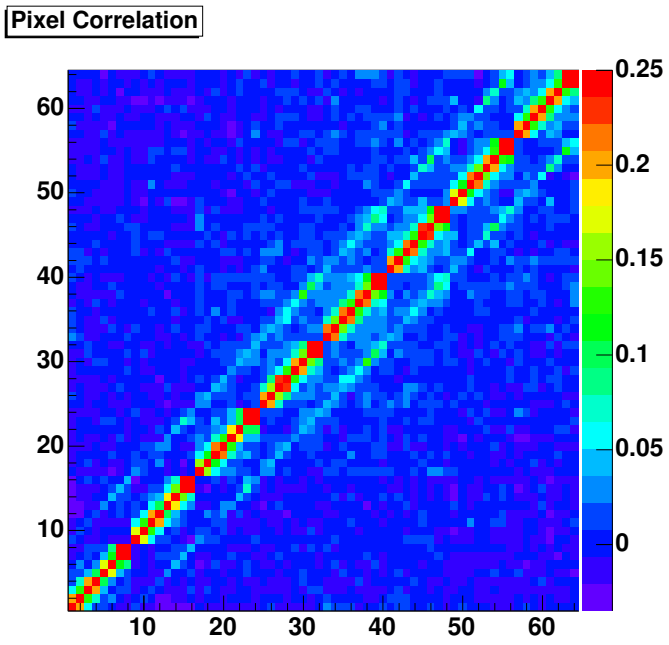

Figure 7.13: *Correlation coefficients between the pulse heights of pixels within one tube. For clarity the scale has been truncated to a maximum of 0.25. The diagonal has a correlation coefficient of C=1.*

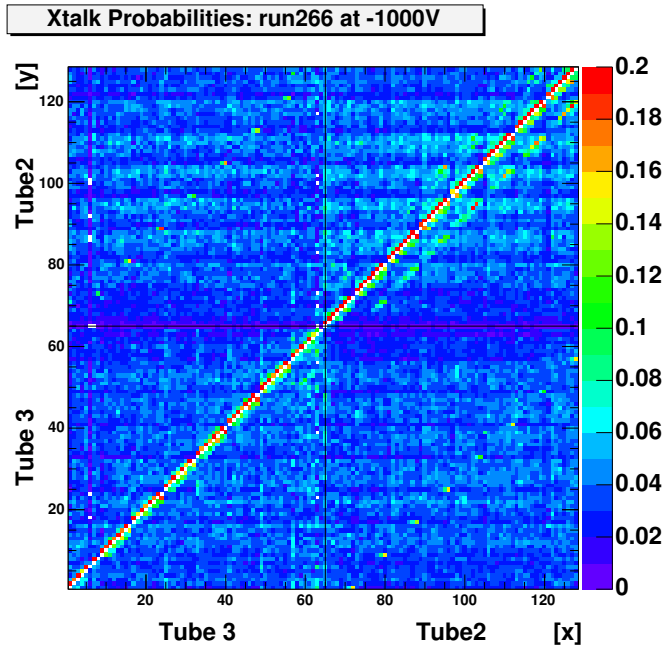

Figure 7.14: *Cross-talk probabilities for two MaPMTs read out by the same Board Beetle. The entries correspond to the probabilities that a signal in pixel* x *was induced by a hit in pixel* y*. The diagonal (in white) has a probability of P=1.*

in groups of 8 pixels. For example pixel 8 does not talk to pixel 9 or pixel 16 does not talk to pixel 17. The correlation coefficient gives the interdependence of the pixels but it does not inform upon the direction of the relationship. It does not say whether it is pixel x which induces cross-talk to pixel y or of if it is the other way round. This information can be obtained by measuring the following cross-talk probability. For a simultaneous hit in pixels x and y, the pixel with the largest pedestal corrected pulse height $H_{x,y}$ in that event is defined as the true hit and the other pixel is hence considered induced. One defines the cross-talk probability P as the ratio of the total number of hits induced in pixel x by pixel y to the total number of hits in pixel x:

$$P_{x \to y} = \frac{\text{Hits in x induced by y}}{\text{Total hits in x}} \tag{7.2}$$

Figure 7.14 shows the cross-talk probabilities for one Board Beetle reading out two MaPMTs. The centre diagonal shows the 100% cross-talk probability of a pixel x to talk to itself. The same pattern as in Figure 7.13 emerges but this time giving information on the direction of the cross-talk. It is mainly asymmetric and horizontal. This cross-talk extends across a full Board Beetle. This confirms that the cross-talk is caused by the electronics itself and not the MaPMT.

The cross-talk pattern fits the way the Board Beetle reads out the MaPMTs and feeds the signal to the Beetle1.2 chip. As can been seen in Figure 7.3, the space between the electrical lines at the connector of the Beetle1.2 chip is narrowed. The same order is used for the multiplexed readout of the Beetle1.2 chip. Charge sharing can then occur between neighbouring lines. Figure 7.15 schematically shows the line ordering for two MaPMTs A and B on one Board Beetle. The lines are interlaced in groups of eight so that pixels 1 to 8 of MaPMT A are fed first and then are connected pixels 1 to 8 from MaPMT B. Then pixels 9 to 16 of A and then 9 to 16 of B and so forth. The cross-talk will occur between 1A-2A, 2A-3A-4A etc. This is the horizontal symmetric cross-talk where pixels induce signal to their neighbours. The interlacing is clearly visible in the clustering in groups of 8

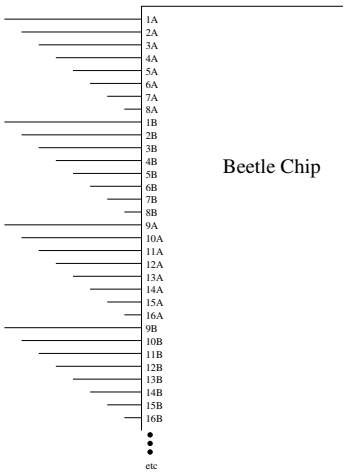

Figure 7.15: *First 16 connectors readout sent to the beetle chip from MaPMT A and B of the same board.*

pixels in Figure 7.13 and 7.14. Cross-talk will also occurs between lines where the readout switches to the other MaPMT. So one should expect cross-talk for 8A-1B, 8B-9A, 16A-9B and on the other hand no cross-talk for 8A-9A or 8B-9B. This is reflected in Figure 7.14 (top left corner and bottom right corner) by the high cross-talk probability for pixels from different MaPMTs. The asymmetric cross-talk is believed to be due to spillover in the pipelines when the data are serialised.

7.4.2 Cross-talk Correction

The cross-talk is corrected by first establishing a map of cross-talk partners from the cross-talk probability. Partners are selected for a P$\geqslant$0.2. This was arbitrary selected so that the map conserved the basic features of the cross-talk. The maps are produced for the cross-talk probabilities computed for each individual Board Beetle. The last bottom right board, see Figure 7.2, was missing for the LED run and hence the top right board map was used instead. Figure 7.16 shows an example of cross-talk map partners used. The pixel pulse height spectra were then corrected in the beam data by rejecting hits for a cross-talk partner with a larger pulse height. In this method the gain for individual pixels is assumed to be the same for all pixels. Figure 7.17 shows the signal spectrum

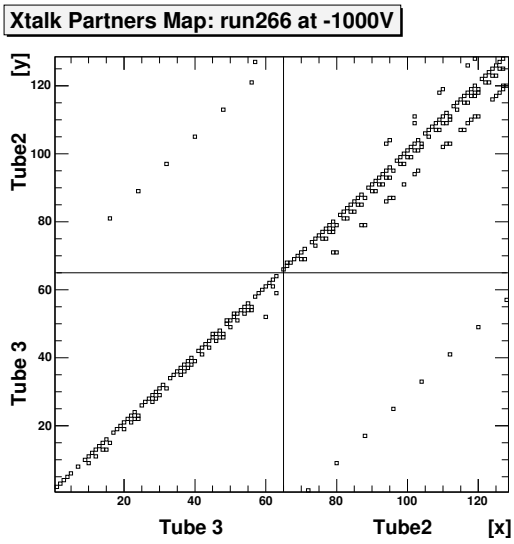

Figure 7.16: *Cross-talk pixel partners map for a cross-talk probability of at least two.*

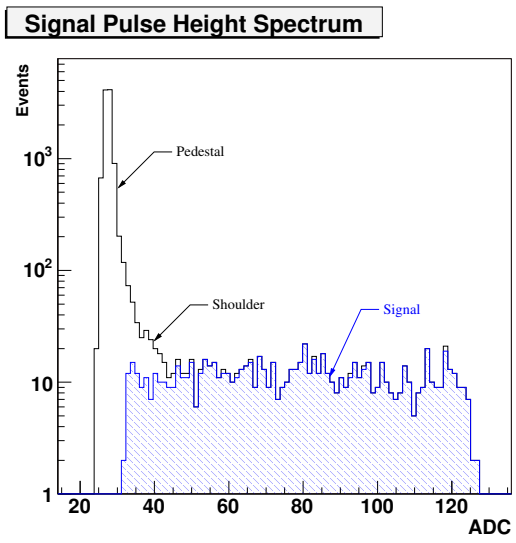

Figure 7.17: *Signal pulse height spectrum before and after cross-talk and pedestal correction (dashed).*

of a pixel before and after cross-talk and pedestal correction (dashed). The pedestal and the "shoulder" have been removed. This bump was suspected to be an effect from first dynode conversions. This turns out to be a negligible effect and is clearly mainly due to cross-talk.

However this method over-corrects. Hits in pixel x induced by pixel y are removed whilst there could have been a genuine hit in both pixel partners. A correction can be applied by defining the fraction of hits in pixel x (f_x) and pixel y (f_y) as the ratio of hits in that pixel over the total number of events. The fraction of corrected hits for pixel x, $f_{cor,x}$, will then be:

$$f_{cor,x} = f_x - f_{crosstalk} \tag{7.3}$$

where $f_{crosstalk}$ is the fraction of hits due to the cross-talk correction. $f_{cor,x} \times f_{cor,y}$ will then be proportional to the number of simultaneous true hits removed. If, let us say, the number of true hits in x, $f_{true,x}$, is small and $f_{true,y}$ is big then it means that x has fewer hits and hence the likelihood of removing simultaneous hits is small. On the other hand a large $f_{true,y}$ means that $f_{true,x}$ is more likely to be induced (remember that they are cross-talk partners) and then the product will be small. However if both $f_{true,x}$ and $f_{true,y}$ are large then the product will be bigger reflecting the fact that the simultaneous hits are more likely to occur. The total over corrected fraction of signal hits is restored by adding this coefficient product:

$$f_{true,x} = f_{cor,x} + \frac{1}{2}(f_{cor,y} . f_{cor,x}) \tag{7.4}$$

where the factor one-half arises from the fact than we correct in only one direction of the cross-talk. There is however no way to know the fraction or real hits from the start. Hence for a first iteration one uses the cross-talk corrected value $f_{cor,x}$ and then re-iterates with the result to obtain a better estimate.

Figure 7.18 shows the Cherenkov ring image for the same data as in Figure 7.12, but after cross-talk correction.This demonstrates that the method used removes most of the cross-talk. The Cherenkov ring agrees with the simulation of Figure 7.11. We observe the beam divergence as the Cherenkov ring is made of two columns of pixel hits on the sides and one row for the top and bottom. A likely mis-alignment of the lenses is visible on the bottom right MaPMT where there is a drop in signal on the top row. The same occurs on the above MaPMT

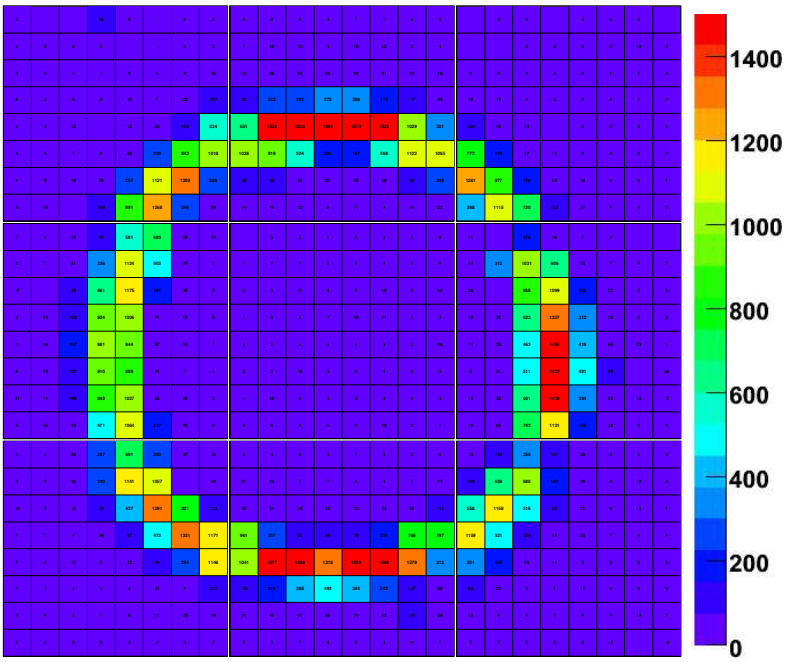

Figure 7.18: *Testbeam Cherenkov photon ring at -900 V after cross-talk correction.*

7.4.3 Photon Yield

The average number of photons per event was calculated from the cumulated corrected hits for each pixel for all MaPMTs. The genuine hit correction was then applied and restored on average 4% of the total hits. Finally, background hits were removed assuming a uniform contribution from scattered Cherenkov light, electronic and detector noise. The background could be assumed uniform over the array so that the correponding hits could be averaged, MaPMT by MaPMT, over all pixels not lying on the Cherenkov ring. The non-ring zone was determined by eye leaving a buffer of one pixel. The same procedure was used over all voltage scans in the range of -750 V to -1000 V.

Figure 7.19 shows the resulting photon yield variation versus the applied MaPMT high voltage before and after cross-talk correction. The raw data show that the cross-talk increases with the voltage. After correction the curve matches the simulation. Nonetheless a slight slope remains. As the high voltage increases, the yield increases from 5.06 ± 0.022 to 7.32 ± 0.027. This is attributed to the fact that a) at large high voltage, cross-talk correction is much larger and a possible inefficiency in the procedure will have a larger effect b) true signal is lost at lower gain. Due to the large number of events varying from 10 000 to 16 000 depending on the runs, the statistical errors are very small and are

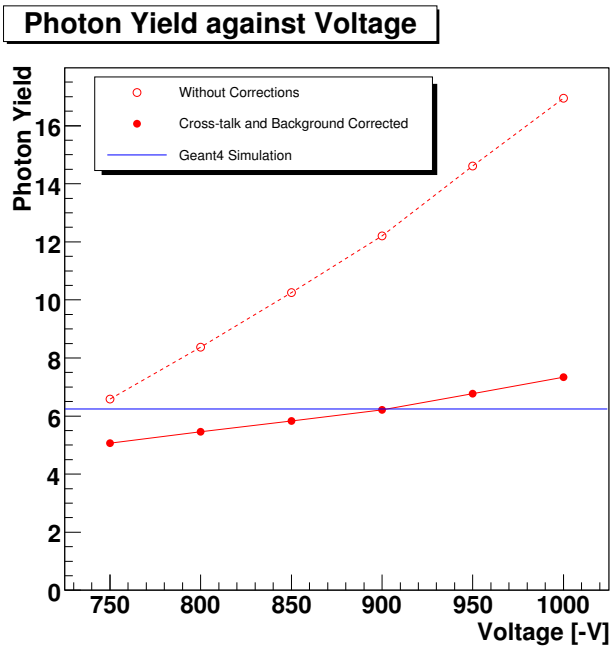

Figure 7.19: *Photon yield per event as a function of hight voltage for the uncorrected (raw) and corrected spectra.*

hence neglected. Table 7.1 shows the photon yield of each tube for the experiment and the simulation. The experimental value of 6.19 photoelectrons per event at the nominal voltage of -900 V is in good agreement with the 6.24 value predicted by the simulation. Hence the 8-dynode stage MaPMTs are a viable solution for the LHCb RICH detectors provided cross-talk corrections are applied.

	Simulation			Testbeam -750 V			Testbeam -800 V			Testbeam -850 V		
Photon Yield	0.59	0.98	0.50	0.38	0.93	0.31	0.44	1.01	0.34	0.47	1.09	0.35
per	1.05	0.00	1.01	0.82	0.00	0.85	0.86	0.00	0.89	0.90	0.00	0.98
tube	0.62	0.97	0.51	0.51	0.84	0.42	0.58	0.91	0.42	0.65	0.96	0.43
Total Yield	6.24			5.06			5.45			5.83		
	Testbeam -900 V			Testbeam -950 V			Testbeam -1000 V					
Photon Yield	0.53	1.16	0.36	0.58	1.27	0.38	0.63	1.4	0.40			
per	0.97	0.00	1.02	1.12	0.00	1.11	1.22	0.00	1.19			
tube	0.70	1.00	0.45	0.76	1.02	0.52	0.83	1.08	0.57			
Total Yield	6.24			6.76			7.32					

Table 7.1: *Photons yields per event obtained from the simulation and the testbeam: for individual tubes and over the whole array. The order follows the layout of Figure 7.18.*

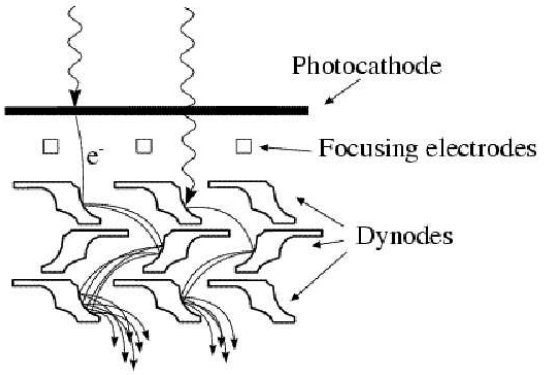

Figure 7.20: *Photoelectron creation at the photocathode and at the 1st dynode of a photomultiplier [60].*

7.4.4 Signal Spectrum fitting

To fit the spectrum of a pixel we assume it is dominated by Poissonnian statistics. One can distinguish two main physical processes taking place inside the phototube: 1) the emission of photoelectrons at the photocathode and 2) the emission of secondary electrons via the dynode chain. These processes are illustrated in Figure 7.20.

In the first case most of the incoming photons are converted to photoelectrons at the photocathode and are then focused towards the amplification dynode chain. In the second case, a small amount of photons pass through the photocathode without being converted. They then hit the first dynode of the amplification chain where they free electrons which in turn start the cascade. This phenomenon is independent of the photocathode conversion and the total probability of photoconversion can be expressed as follows:

$$\mathcal{N}'_{n,k}(\mu,\mu_1) = N \cdot \frac{\mu^n\ e^{-\mu}}{n!}\frac{\mu_1^k\ e^{-\mu_1}}{k!} \qquad \Rightarrow \qquad \sum_{n=0}^{\infty}\sum_{k=0}^{\infty}\mathcal{N}'_{n,k} = N \tag{7.5}$$

Where $\mathcal{N}'_{n,k}$ is the number of events with a signal from $n+k$ photoelectrons originating from the photocathode (n) and from the first dynode (k), N is the total number of events in the signal spectrum, μ and μ_1 are the parameters of the Poisson distributions, i.e. the average probabilities of producing a photoelectron at the photocathode (μ) or at the first dynode (μ_1).

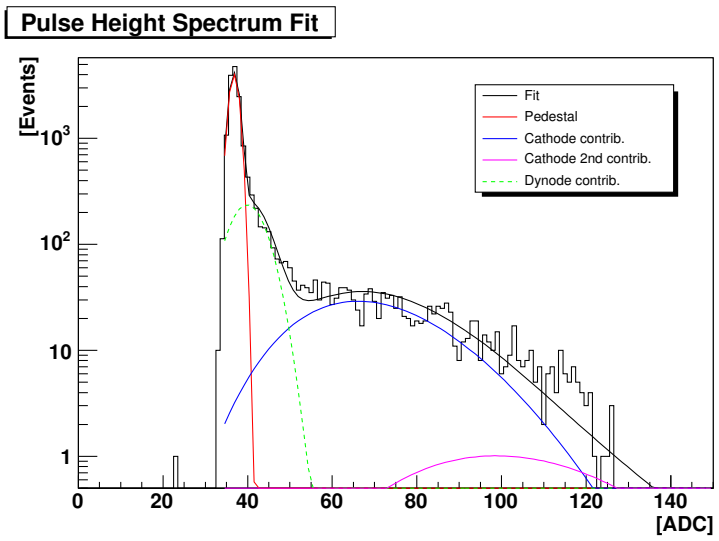

Figure 7.21: *MaPMT signal spectrum with a Poisson fit overlayed with the assumed photoproduction at the first dynode. All contributions to the global fit are shown separately.*

The photon distribution is then considered as a convolution of Gaussian and Poissonnian statistics as shown in Equation 7.6 [61] .

$$\mathcal{G}'_{n,k}(x) = \begin{cases} \mathcal{N}_{n,k} \sum_{m=0}^{\infty} \frac{(nK_1)^m \cdot e^{-nK_1}}{m!} G(x, Q_0 + (m+k)Q_2, \sigma_0^2 + (m+k)\sigma_2^2) & n = 1,2 \\ \mathcal{N}_{n,k} G(x, Q_0 + Q_{n,k}, \sigma_0^2 + \sigma_{n,k}^2) & n \geq 3 \end{cases} \tag{7.6}$$

Where $\mathcal{N}$ is the number of events, Q_n is the mean pulse height of all ADC counts offset by the pedestal Q_0, Q_2 is the total gain of an electron emerging from the 1^{st} dynode hitting the 2^{nd}, σ_n is the width of the signal distribution, σ_0 being the width of the electronic noise (the pedestal) and σ_2 the width of the sub-signal emerging from the 1st dynode, m is the number of electrons produced at the 1st dynode, $K_1 = Q_1/Q_2$ is the signal gain at the 1st dynode and finally k is the photoelectrons coming from the 1st dynode. When the number of photoelectrons n is greater than two, the gain at the first dynode is high enough to be approximated by a Gaussian distribution. If the photoelectron multiplicity is however smaller, with a weak gain at the first dynode, a Poisson distribution gives the best fit.

This algorithm has been implemented in FORTRAN in [61] and was converted into C for this work. The converted code is shown in appendix C.1. Figure 7.21 shows the fit obtained on a pixel together with the signal contributions. The signal is overall well fitted. Considering the first dynode effect allows to fit the cross-talk well, even if the dynode effect is in reality physically negligible.

7.4.5 Beetle1.2 Pulse Height

The MaPMT pulse is recorded and sampled by the Beetle1.2 chip every 25 ns. A time delay arises from the asynchronous trigger with respect to the 25 ns clock of the Beetle pipeline. This delay was recorded during the testbeam by a Time Delay Counter (TDC) as shown in Figure 7.22. Sampling on the TDC allows to reconstruct the Beetle pulse shape. The data is first selected for a 5 ns wide time interval on the TDC and then fitted using the previously defined Poisson based algorithm in order to extract the mean signal pulse height. The fit is run over one pre-selected pixel at a voltage of -800 V. Figure 7.23 shows the resulting distribution of the mean pulse height as a function of the time interval. The signal is consistent with the 25 ns width of the Beetle chip signal.

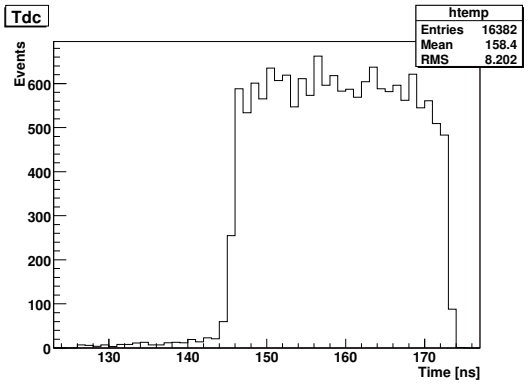

Figure 7.22: *Pipe line time delay interval between the trigger and the 25 ns clock-cycle as recorded by the Time Delay Counter (TDC).*

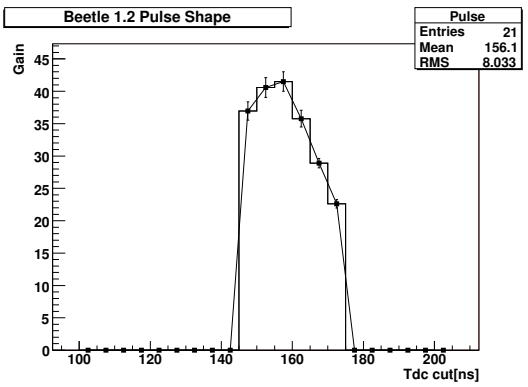

Figure 7.23: *Beetle1.2 Pulse height as a function of sampled time intervals on the TDC.*

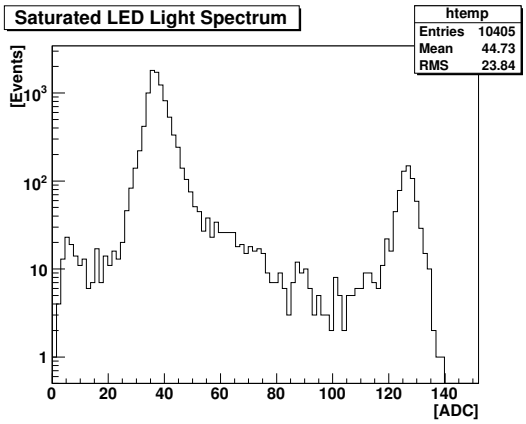

Figure 7.24: *Saturated LED signal spectrum.*

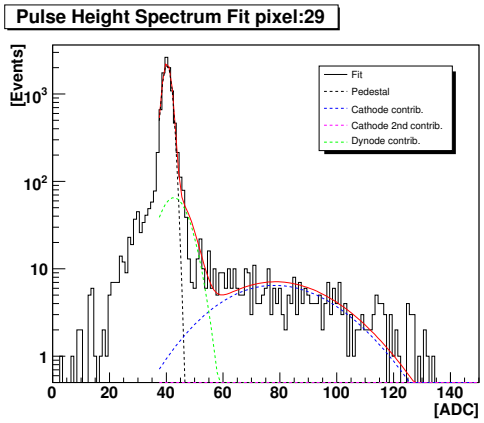

Figure 7.25: *Non-saturated LED fitted spectrum with cross-talk correction.*

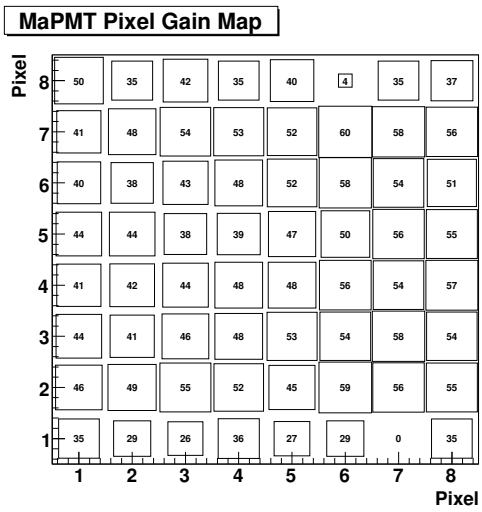

Figure 7.26: *Pixel gain over the whole MaPMT at -900 V.*

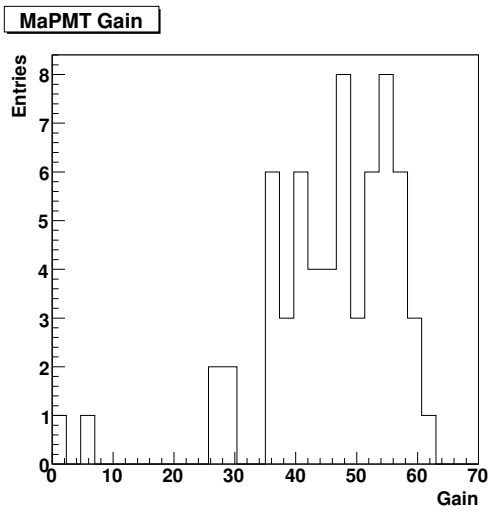

Figure 7.27: *Pixel gain distribution over the whole MaPMT at -900 V.*

7.4.6 MaPMT Gain Map

The gain for all the pixels of an MaPMT has been established using LED runs in which all pixels are illuminated. Signal spectra from LEDs are different from the beam data due to the timing of the LED light source. LED data were only taken to make sure that the MaPMTs were operational and that they did see light. Hence the delay times for the LED trigger were not precisely adjusted. A saturated LED spectrum is shown in Figure 7.24. Signal hits that are sampled too late due to the light delay appear as weak signal before

the pedestal. The LED light can also saturate the amplifier range. In that case the signals are amplified to the maximum range of the amplifier and they appear at the high end of the spectrum.

Fits were hence conducted on an MaPMT displaying little saturation. The data taken for -900 V for the top right corner tube (see Figure 7.2) were selected as suitable. We applied cross-talk corrections before the fitting. Figure 7.25 shows a fitted spectrum for a selected pixel. The 64 fitted spectra of all channels are shown in appendix C.2. The resulting gain map is shown as a box diagram in Figure 7.26. There are two dead channels, pixel 6 and 63 and weaker channels on the top and bottom row. Figure 7.27 shows the gain has a histogram in which one can see that the gain varies at most by a factor two. This is well within the factor three variation of individual pixels quoted by the manufacturer [31].

7.5 Conclusion

The 8-dynode stage MaPMTs have been tested as an array of 3×3 tubes in a testbeam at CERN. The signals have been read out using the Beetle1.2 chip which will be used in the final LHCb detector. Cherenkov rings coming from a 10 GeV pions beam have been successfully measured. However, the Beetle readout induces a cross-talk which can be accounted for. After the cross talk correction the data are in agreement with the simulation. A convolution of Gaussian and Poissonnien statistic algorithm allows a good fit of the signal. The pulse height after the pre-amplifier has been extracted using the fitting method by sampling. The variation of gain, overall pixels of an MaPMT, has been estimated to be at most two and is within the factor three variation quoted by the manufacturer [31]. The testbeam study showed that the 8-dynode stage MaPMT fulfilled the LHCb requirement for fast readout using the Beetle1.2 chip.

Chapter 8

Summary and Conclusion

The LHCb Experiment has been designed for CP violation precision measurements in the B-meson decays. The assembly of the detector is planned to coincide with the Large Hadron Collider completion in 2007. The 14 TeV centre of mass energy provided by the LHC will allow high precision measurements in the B-sector to be made in channels which current B-factories cannot access. Decays channels such as $B_s^0 \to D_s K$ and $B_s^0 \to \pi\pi$ suffer from high background requiring efficient charged particle identification. The LHCb will achieve this task using two Ring Imaging Cherenkov Detectors. The RICH detectors use photodetectors to identify the Cherenkov rings. Two types of photodetectors have been envisaged, (1) the Hybrid PhotoDetector as prime solution and (2) the Multianode PhotoMultipliers as backup solution. This thesis presented the work done in characterising the later. This work was critical to the re-optimisation of the LHCb experiment.

During the optimisation of the experiment, the first level trigger required more bending power to improve its precision. This resulted in an increase in the magnetic field seen at the photodetector plane to a total field of 2.5 mT inside the shielding box of RICH1. We carried out studies on the behaviour of MaPMTs in magnetic fields up to 35mT. It was established that the MaPMT could withstand up to 2 mT without any protection and any distortion. A 0.9 mm thick, 30 mm wide and 60 mm long sheath of μ-metal allows to extend its use to 20 mT. Optimisation studies of the shield have been simulated using Finite Element Analysis. They showed that the shield could be reduced to a length of 40 mm. The mounting on the detector arrays of 4×4 tubes as envisaged would require the use of interspaced sheet of μ-metal which has similar performances to the shield used for a

single MaPMT. Overall the study showed that MaPMT can be used in the new constraints meaning the project was still a viable solution for LHCb.

The readout out electronics used to that point were custom made and the next challenge for the project was to use the LHCb readout radiation hard Beetle1.2 chip. A three by three array of MaPMT was tested at a testbeam from the CERN PS. We established that the MaPMT Beetle readout board suffers cross-talk for which we developed a correction algorithm. When accounted for, MaPMTs in the testbeam detect photons according to the simulation with a photon yield of 6.2 at -900 V. The variation in individual pixel gain remains in the factor three margin quoted by the manufacturer.

Hence MaPMT have remained a viable solution for the two RICH detectors of the LHCb experiment. Finally a decision had to be made between the two photodetector choices. The HPD was retained based on cost requirements. The closure of the project meant no further tests were performed. A planned study of a whole MaPMT array in magnetic field with and without the shield array in place was hence not carried any further.

Appendix A

Signal Response to Magnetic Fields

A.1 MaPMT Support

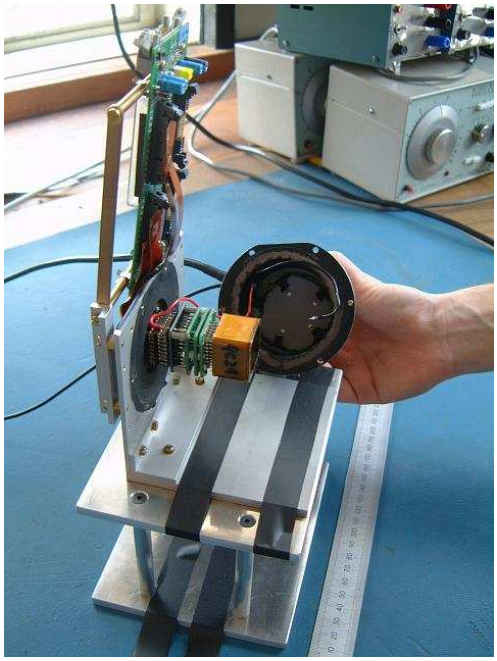

Figure A.1: *Opened MaPMT frame support showing the tube, the LED ring at the back of the light tight cylinder, the capton cable on the APVm board.*

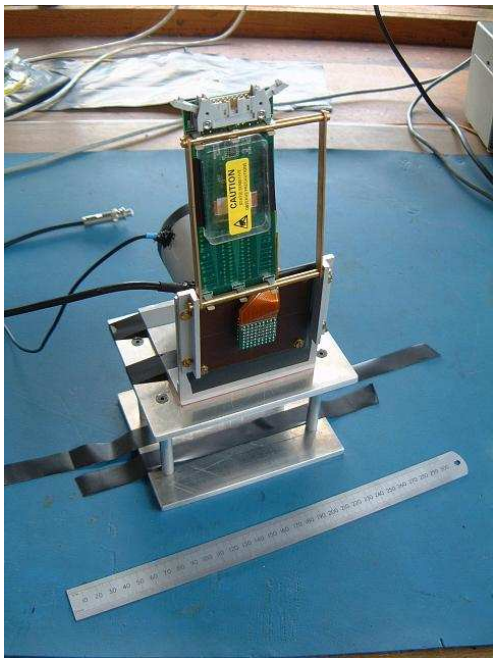

Figure A.2: *Back of the closed MaPMT frame support showing the capton cable connection to the APVm board.*

A.2 MaPMT Signal Map

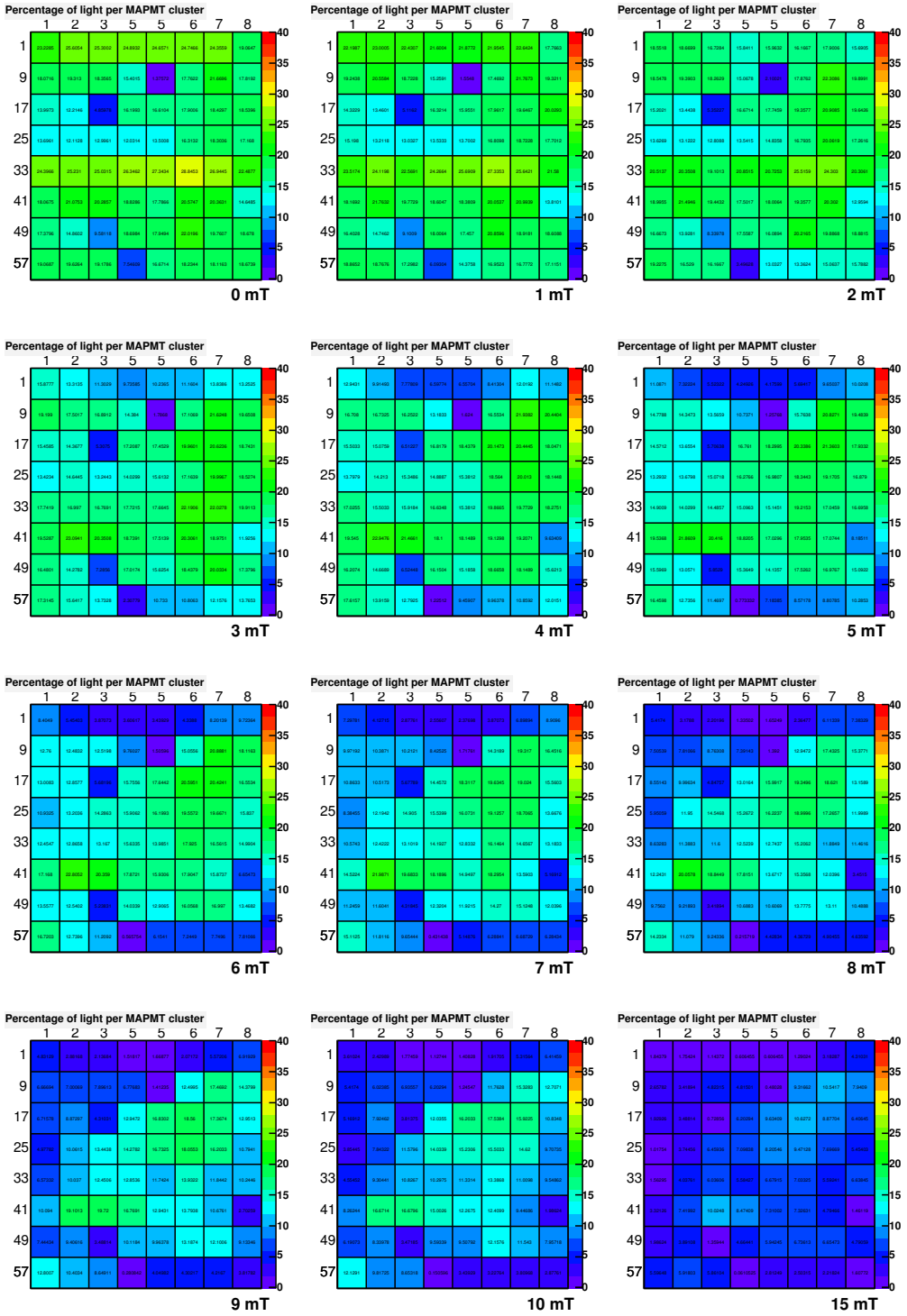

Figure A.3: *Signal response of tube 9K20C3, without shielding, to magnetic fields of 0, 1, 2, 3, 4, 5, 6, 7, 8, 9, 10, 15 mT, respectively (from left to right).*

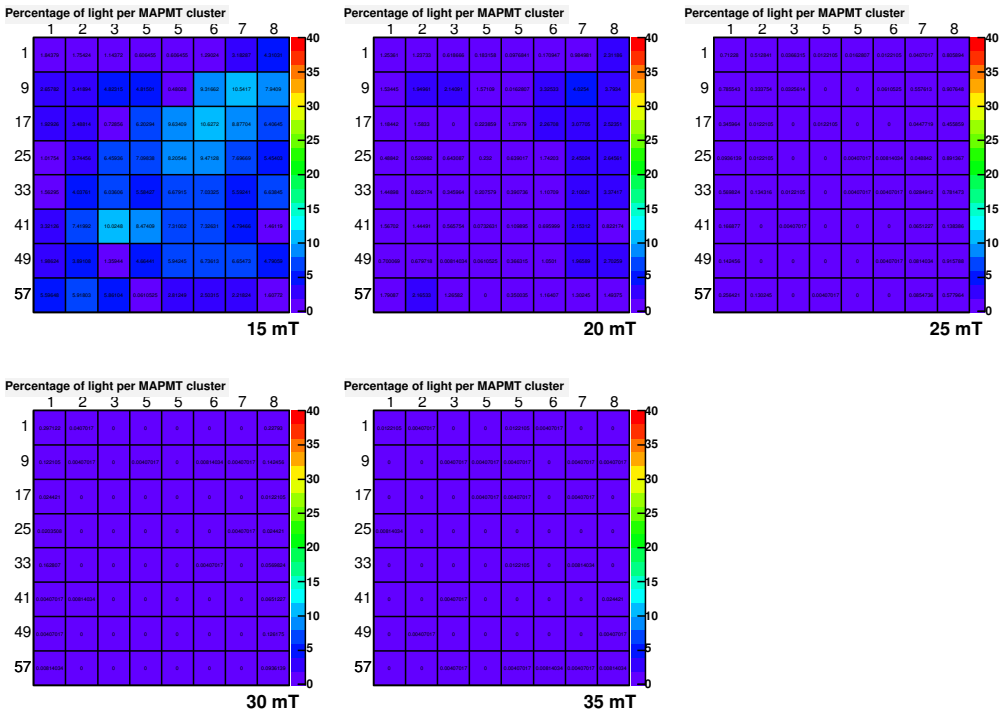

Figure A.4: *Signal response of tube 9K20C3, without shielding, to magnetic fields of 15, 20, 25, 30 and 35 mT, respectively (from left to right).*

A.3 MaPMT Signal Map with Mask leaving Row 5 exposed

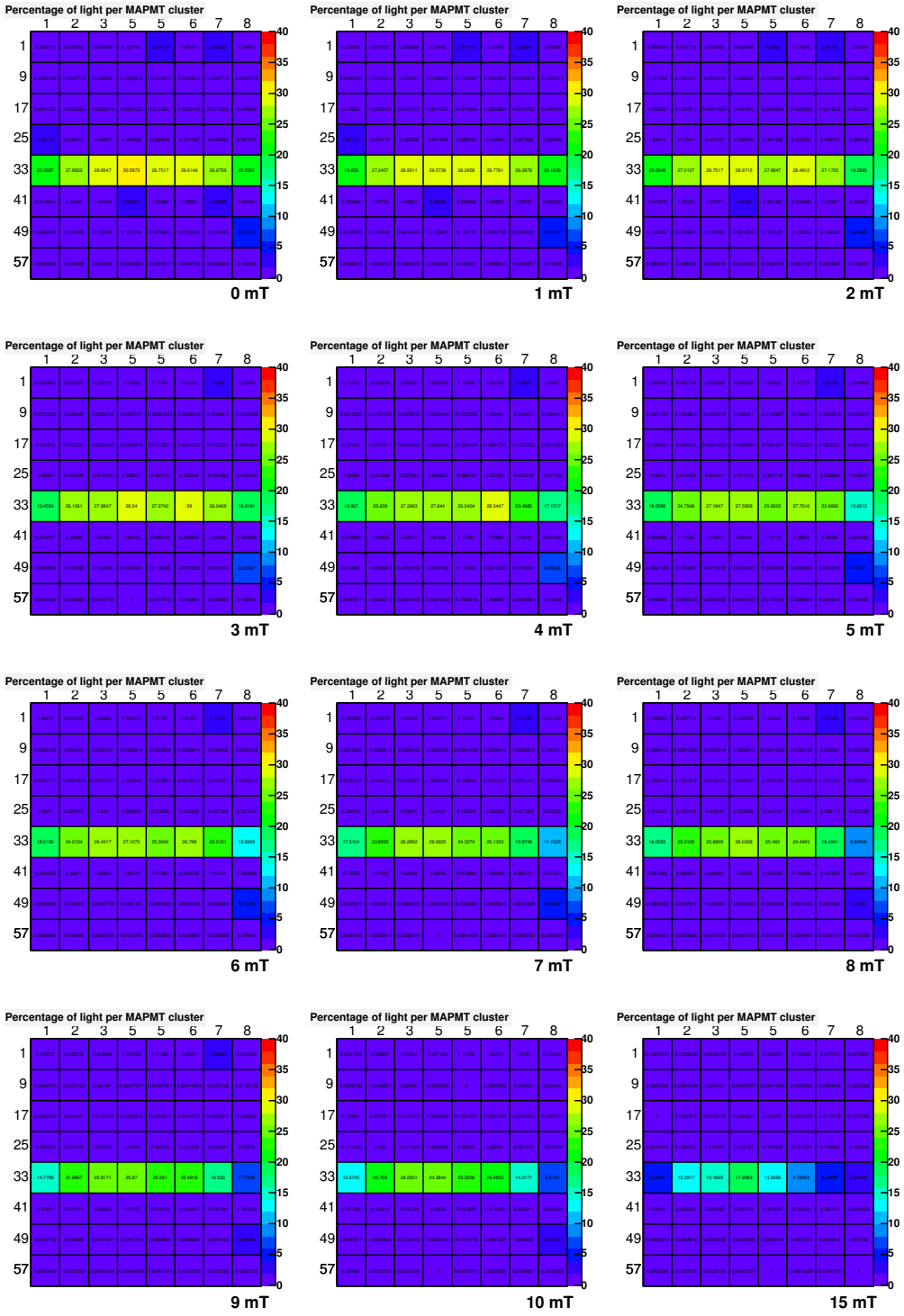

Figure A.5: *Signal response of tube 9K20C3 with a pinhole mask leaving row 5 exposed, without shielding, to longitudinal magnetic fields of 0, 1, 2, 3, 4, 5, 6, 7, 8, 9, 10, 15 mT, respectively (from left to right).*

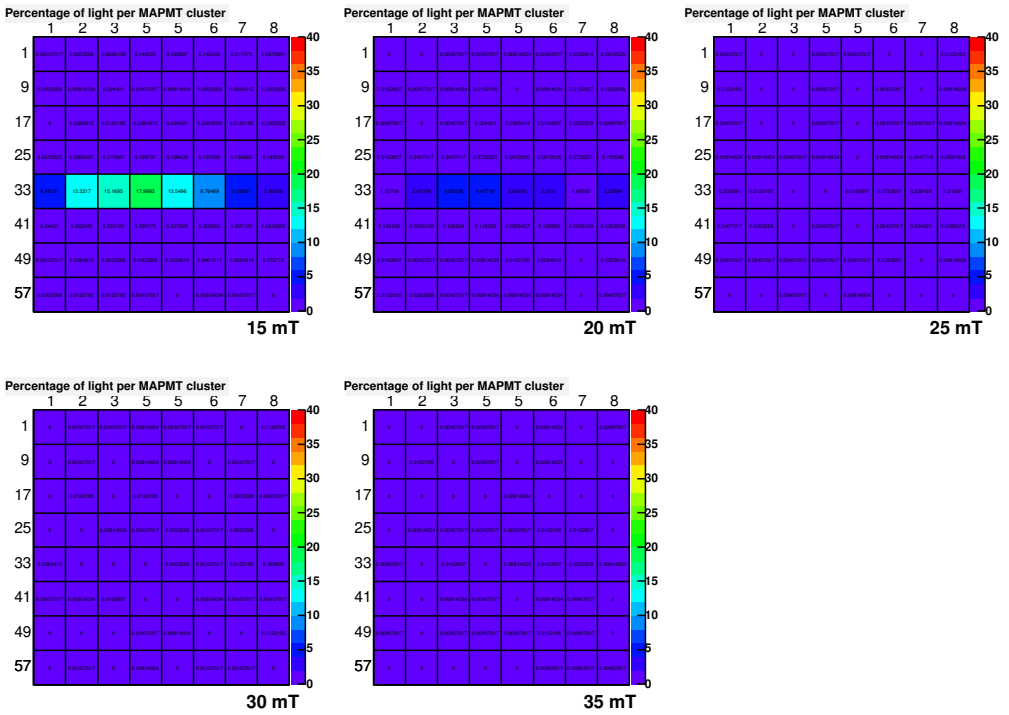

Figure A.6: *Signal response of tube 9K20C3 with a pinhole mask leaving row 5 exposed, without shielding, to longitudinal magnetic fields of 15, 20, 25, 30 and 35 mT, respectively (from left to right).*

A.4 MaPMT Signal Map with Mask leaving Row 5 exposed

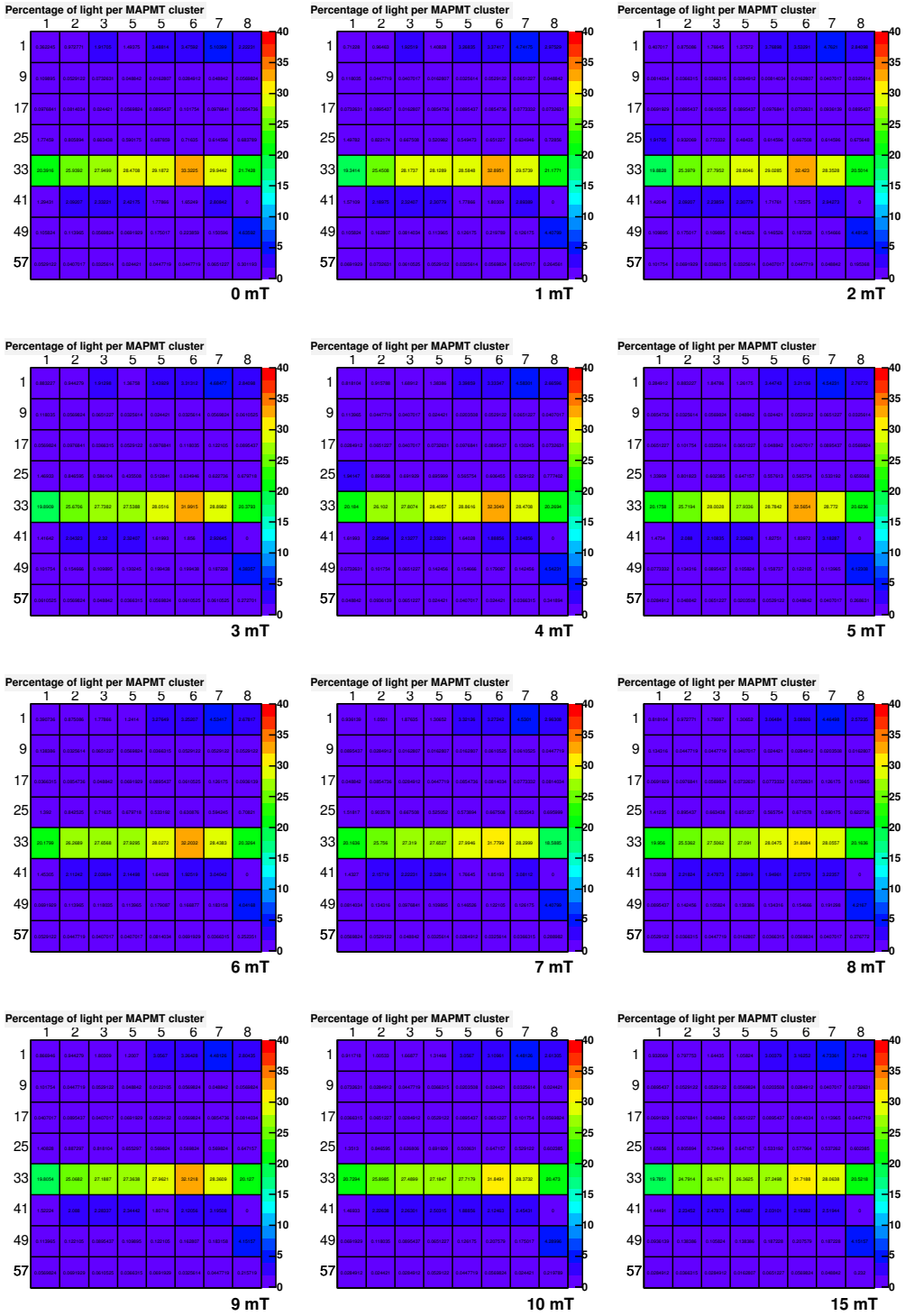

Figure A.7: *Signal response of tube 9K20C3 with a pinhole mask leaving row 5 exposed, without shielding, to transverse magnetic fields of 0, 1, 2, 3, 4, 5, 6, 7, 8, 9, 10, 15 mT, respectively (from left to right).*

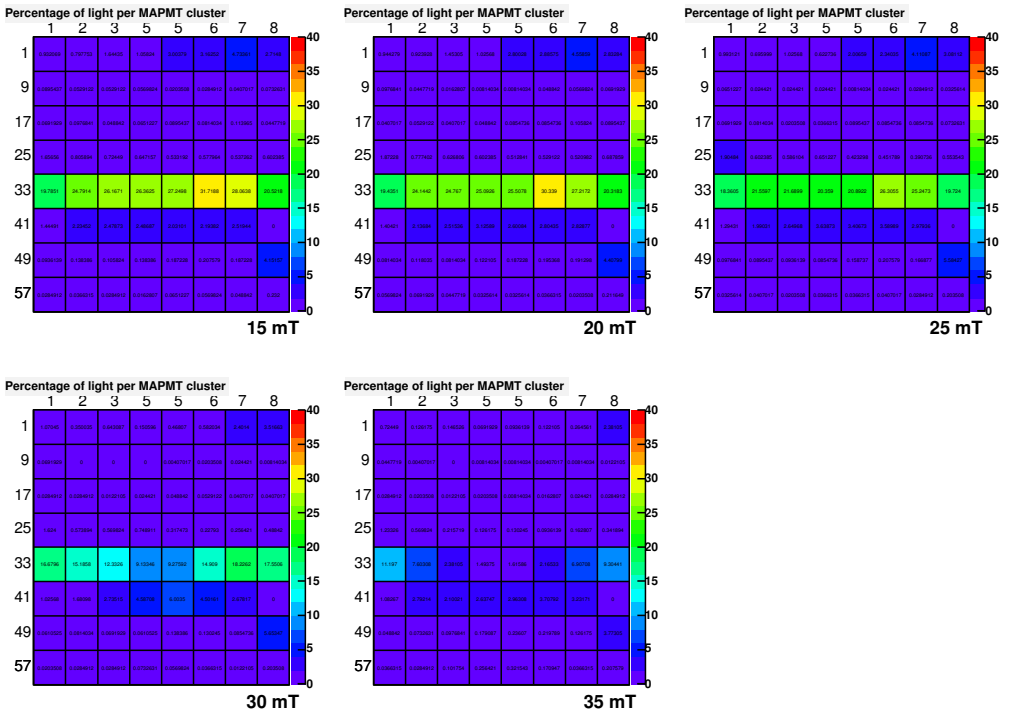

Figure A.8: *Signal response of tube 9K20C3 with a pinhole mask leaving row 5 exposed, without shielding, to transverse magnetic fields of 15, 20, 25, 30 and 35 mT, respectively (from left to right).*

Appendix B

OPERA8 Simulation

B.1 Comparison of OPERA8 with the Experiment

The following figures compare the experiment and the simulation for 10, 20 and 30 G respectively, with and without the shield.

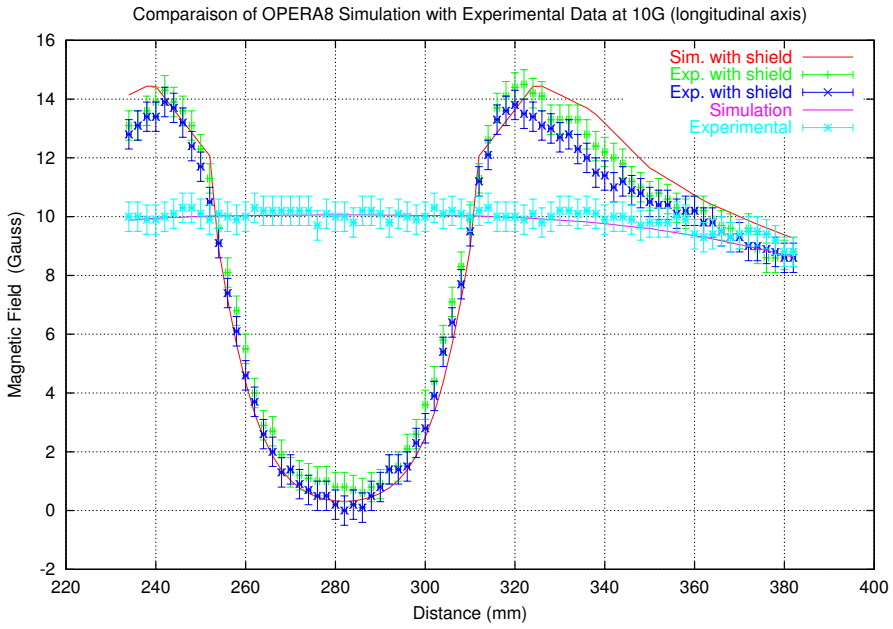

Figure B.1: *Comparison of OPERA results with the experiment for 10 G.*

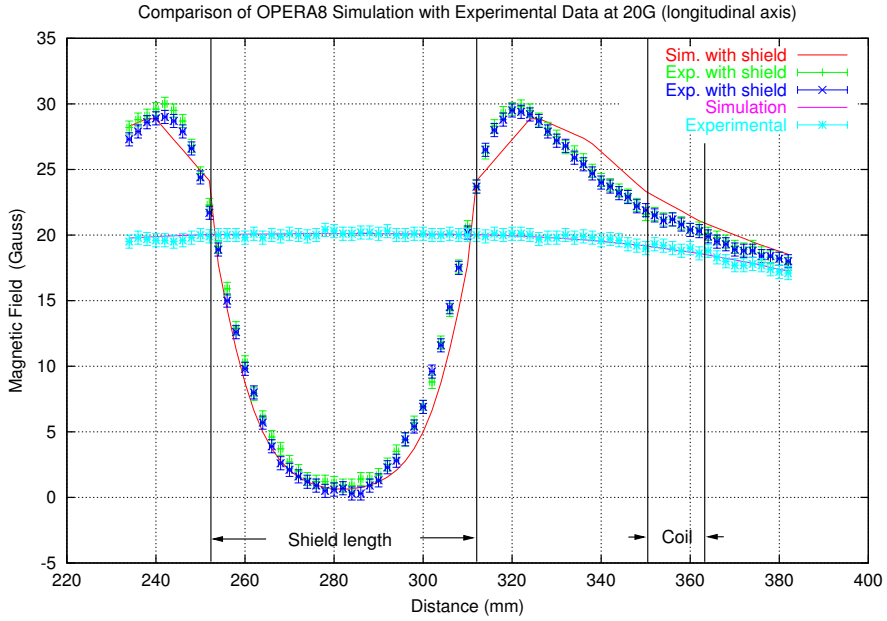

Figure B.2: *Comparison of OPERA results with the experiment for 20 G.*

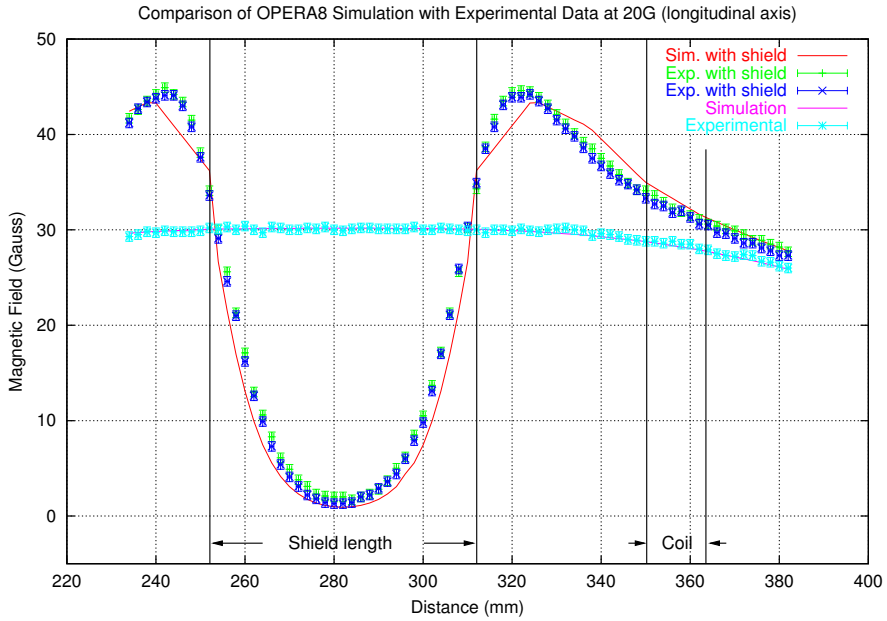

Figure B.3: *Comparison of OPERA results with the experiment for 30 G.*

Appendix C

Testbeam Analysis

C.1 Fitting function

The following is the code used to fit the signal spectrum of individual MaPMT pixels. It was adapted from FORTRAN to C++ and root.

```
double poissonf(double *v, double *par)
{

  double K1;
  double phe_poiss_dyn=0;
  double factn,factm,factk,arean,areak,area,sigma,aream,areatot,x0;
  int nphe,mhigh;

  double norm      = par[0];   // normalisation factor
  double average   = par[1];   // average number of p.e. per event
  double pedestal  = par[2];   // position of pedestal
  double width_ped = par[3];   // width of pedestal
  double signal    = par[4];   // offset from pedestal to single p.e. signal
  double width_sig = par[5];   // width of single p.e. signal
  double fstdynavg = par[6];   // average number of p.e. created by 1st dynode
  double firstdyn  = par[7];   // position of 1st dynode p.e. signal
  double width_dyn = par[8];   // width of 1st dynode signal

  K1  = signal / firstdyn;
```

```
  for(int n=nlow;n<=nlim;n++){
    for( int k = klow;k<=klim;k++){
      nphe = n + k;
      factn = fact[n+1];
      factk = fact[k+1];

      arean = pow(average,n) * exp(-average) / factn;
      areak = pow(fstdynavg,k) * exp(-fstdynavg) / factk;
      area  = norm * arean * areak;

      if (n==0 || n>2){
        sigma = sqrt(pow(width_ped,2) + double(n)*pow(width_sig,2)
                + double(k)*pow(width_dyn,2));
        x0 = pedestal + double(n)*signal + double(k)*firstdyn;
        phe_poiss_dyn+=area*exp(-0.5*pow((v[0]-x0),2)/pow(sigma,2))
                       /(2.50663*sigma);
        continue;
      }

      mhigh = n*10 + 10;
      for(int m= 0;m<mhigh;m++){
        sigma = sqrt(pow(width_ped,2)+(double(m)+double(k))*pow(width_dyn,2));
        x0 = pedestal+(double(m)+float(k))*firstdyn;
        factm = fact[m+1];
        aream = pow((double(n)*K1),m)*exp(-double(n)*K1)/factm;
        areatot = area*aream;
        phe_poiss_dyn+=areatot*exp(-0.5*pow((v[0]-x0),2)/pow(sigma,2))
                       /(2.50663*sigma);
      }
    }
  }

  return phe_poiss_dyn;

}
```

C.2 Spectrum fits of one MaPMT

The following figures are the spectrum fits of each 64 pixel of the MaPMT taken at -900V for a LED light scan.

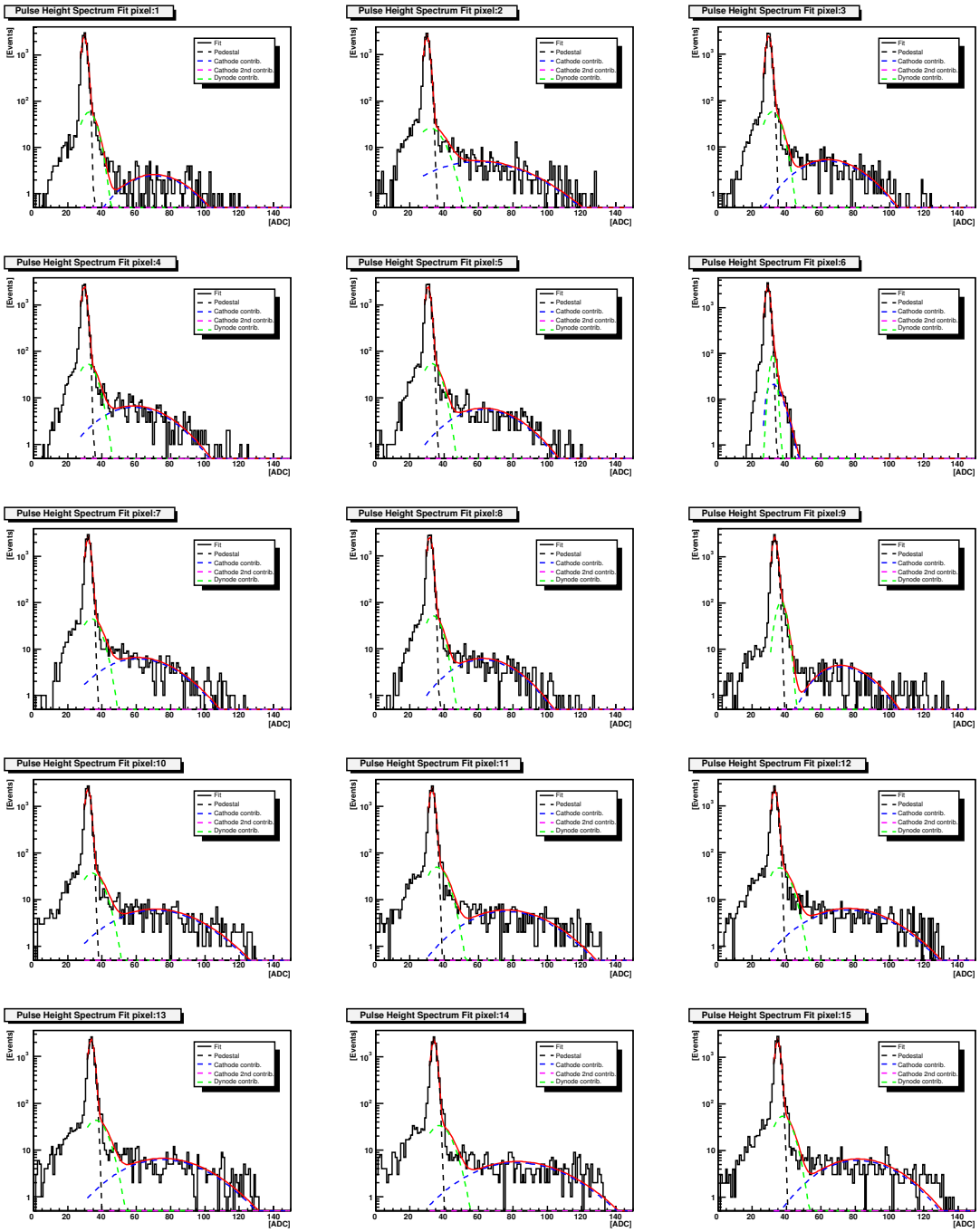

Figure C.1: *LED Spectrum fit for pixel 1 to pixel 15.*

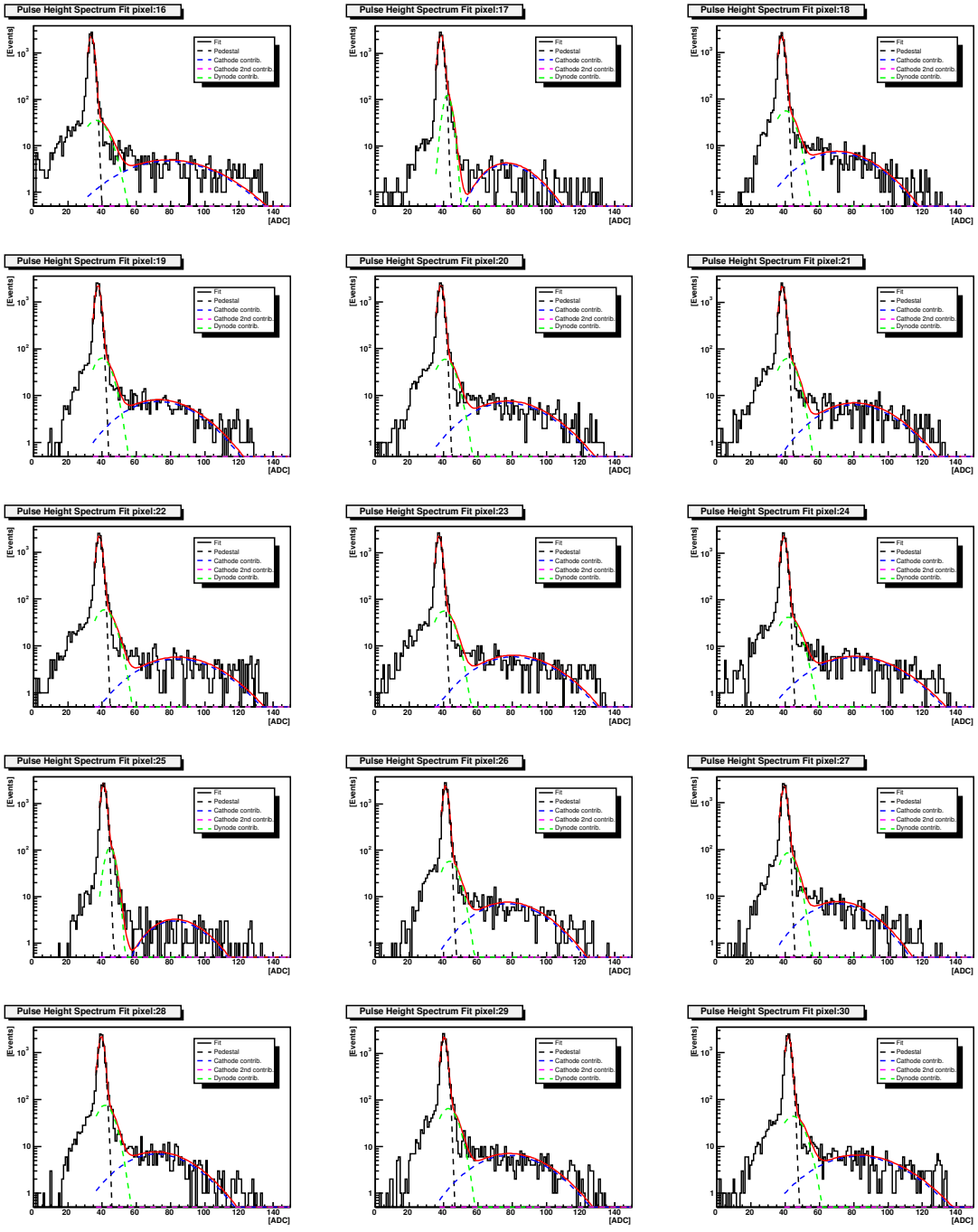

Figure C.2: *LED Spectrum fit for pixel 16 to pixel 30.*

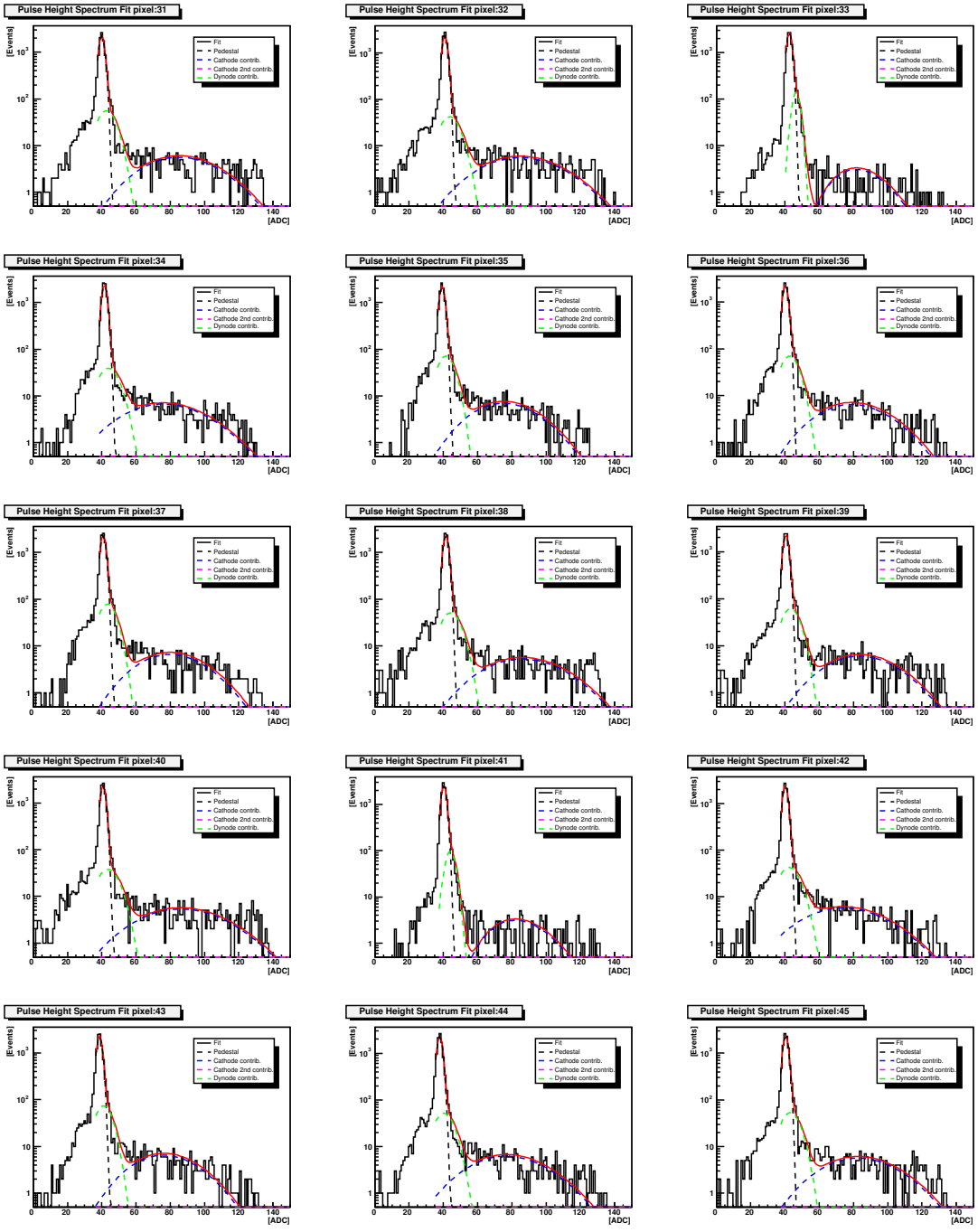

Figure C.3: *LED Spectrum fit for pixel 31 to pixel 45.*

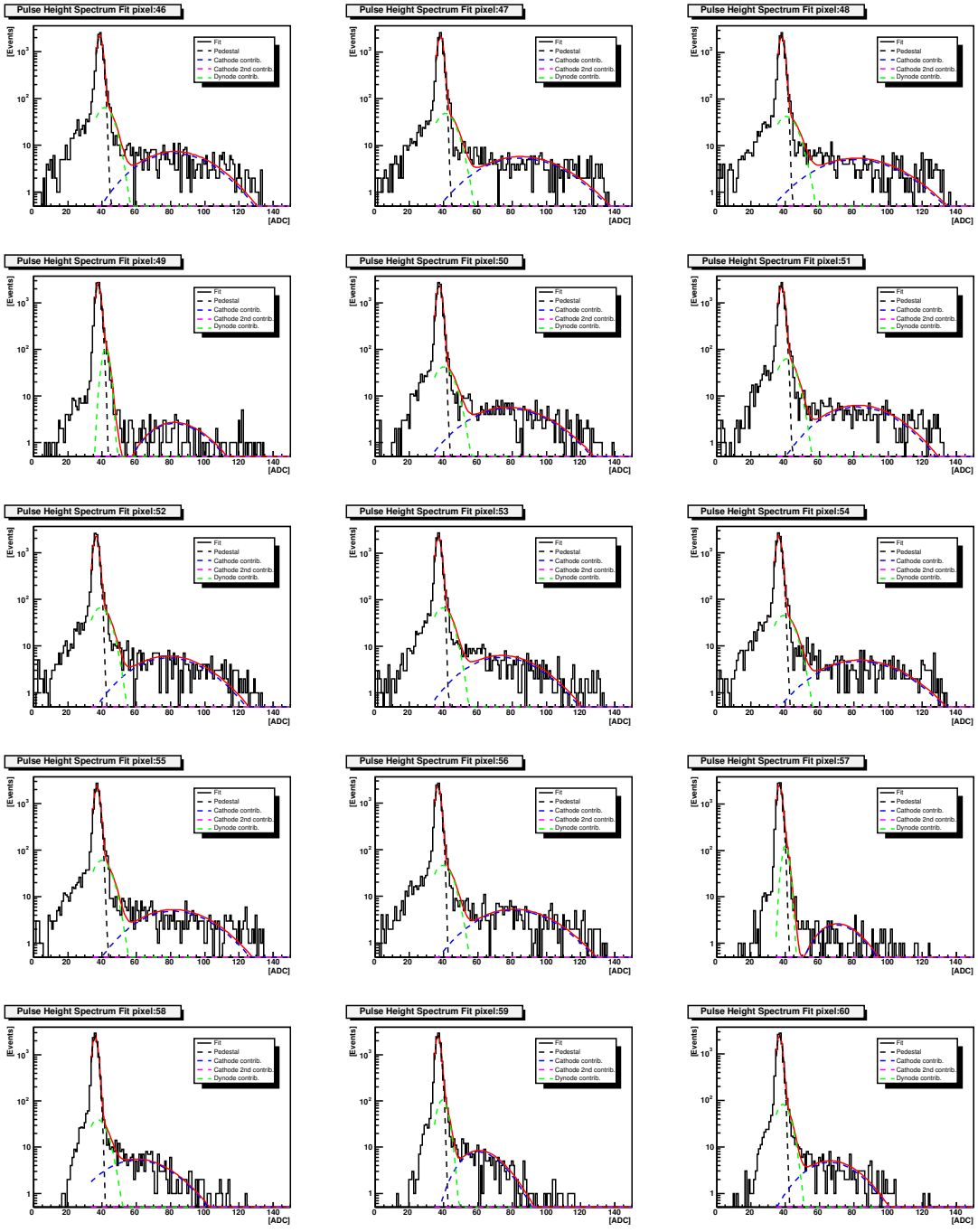

Figure C.4: *LED Spectrum fit for pixel 46 to pixel 60.*

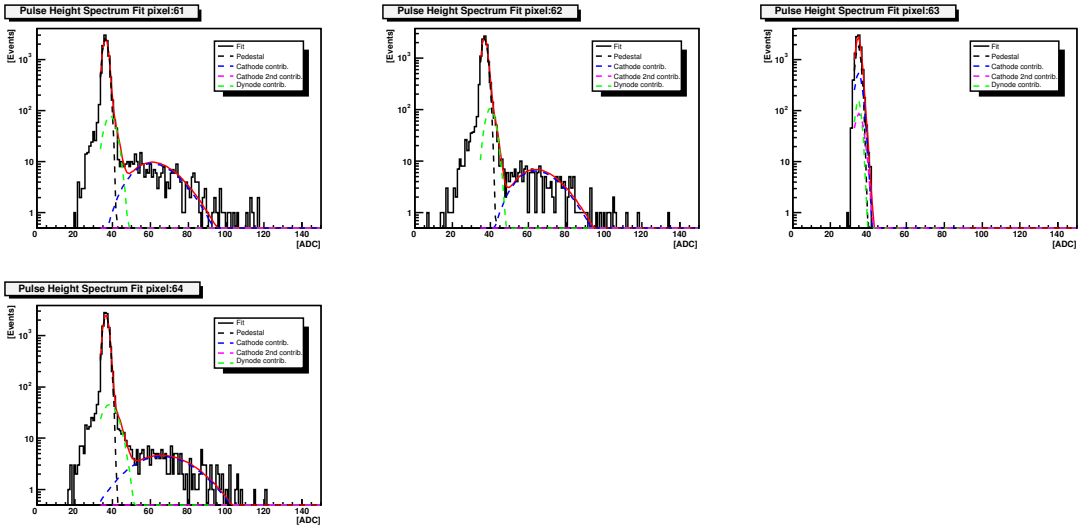

Figure C.5: *LED Spectrum fit for pixel 61 to pixel 64.*

Bibliography

[1] A. D. Sakharov, Pisma Zh. Eksp. Teor. Fiz. 5, 32 (1967) [JETP Lett. 5, 24 (1967)].

[2] *Baryogenesis*, U A Yajnik, Pramana - J.Phys, vol 54. No. 4, April 2000

[3] T.D Lee and C.N Yang *Question of parity conservation in weak interactions*, The Physical Review, 104, OCt 1, 1956

[4] C.S Wu et al. *Experimental test of parity conservation in beta decay*, Physical Review, 105(4), 1957

[5] V.L Fitch, J.H Christenson, J.W Cronin and R. Turlay, *Phys. Rev. Lett*, 13(1964):138

[6] B. Aubert et al. (BaBar collaboration), *Measurement of CP-Violating Asymmetries in B^0 Decays to CP Eigenstates*, Phys. Rev. Lett. 86, 2515 (2001)

[7] A. Abashian et al. (Belle collaboration), *Measurement of the CP Violation Parameter sin2 phi in B_d^0 Meson Decays* Phys. Rev. Lett. 86, 2509 (2001)

[8] M. Kobayashi and T. Maskawa. *CP violation in the renormalizable theory of weak interactions*, Pro.Theor.Phys., 49(1973):652

[9] F.J Gilman, K Kleinknecht, B Renk, *The Cabibbo-Kobayashi-Maskawa Quark-mixing Matrix*, Physics Letters B, Review of Particle Physics, Vol 592 Issues 1-4, 15 July 2004, p130

[10] L, Wolfenstein, Phys. Rev. Lett, 51, 1945 (1984)

[11] C.Jarlskog, Phys. Rev. Lett, 55, 1039 (1985)

[12] Michael Beyer (Ed), *CP Violation in Particle, Nuclear and Astrophysics*, Springer, 2002

[13] Gustavo Castelo Branco, Luís Lavoura, João Paulo Silva, *CP violation*, International Series of Monographs on Physics 103, Oxford Science Publicaitons, 1999

[14] M.Krämer, FJP Soler, *Large Hadron Collider Phenomenology*, *Proceedings of the Fifty Seventh Scottish Universities Summer School in Physics, B Physics* Valerie Gibson, Institute of Physics, Scottish Graduate Series, 2003

[15] The CKMfitter Group, *Updated Results on the CKM Matrix* http://www.slac.stanford.edu/xorg/ckmfitter/ckm_inputs.html, March 30,2005

[16] The CKMfitter Group, *CKM Fitter Plots*, http://www.slac.stanford.edu/xorg/ckmfitter/ckm_results.html

[17] R.Forty and O.Schneider, *RICH pattern recognition*, LHCb 98-40.

[18] LHCB collaboration, *LHCB: Reoptimized Detector Design and Performance*, CERN/LHCC 2003-03, LHCb TDR9, 2003

[19] S.Korpar, *HERA-B RICH*, Nuclear Instruments and Methods in Physics Research A 502 (2003) 41-45, (2003)

[20] E.Albrecht et al. (Ed), *Performance of a cluster of multi-anode photomultipliers equipped with lenses for use in a prototype RICH detector*, Nucl. Instrum. Meth. A488: 110-130,2002

[21] Richtmyer and Kennard, *Introduction to Modern Physics*, McGraw Hill Book Company, 1947

[22] Ann. d. Physik, vol.31, p.983, (1887)

[23] Ann. d. Physik, vol.31, p.301, (January 1888)

[24] Ann. d. Physik, vol.38, pp.40,497, (1889)

[25] J.J. Thomson,*Cathode Rays*, Philosophical Magazine 44, 295, 1897.

[26] A.Einstein, Ann. d. Physik, vol 17, p132 (1905)

[27] V.K Zworykin and J.A Rajchman:proc.IRE,27,558 (1939),

[28] J. Seguinot, T. Ypsilantis (CERN) *Photoionization and Cherenkov Ring Imaging*, CERN-EP-PHYS-76-60, Nov 1976. 44pp. Published in Nucl.Instrum.Meth.142:377,1977

[29] W.R Leo, *Techniques for Nuclear and Particle Physics Experiments*, Springer-Verlag, 1994

[30] S-O Flyckt and C Marmonier, *Photomultipliers Tubes: Principles and Applications*, Photonis, 2002

[31] Hamamatsu Photonics, *Photomultiplier Tube: Principle and Application*, 1994

[32] Glenn F.Knoll, *Radiation Detection And Measurement - Second Edition*, Wiley, 1989

[33] E.Albrecht, *et al*, Nucl. Instr. and Meth. **A442**(2000) 164

[34] S.Easo, *et al*, *Tests of full-scale Pixel HPD prototype*. LHCb 2000-70

[35] T Gys et al., *Performance of Full-Scale Pixel HPD Tubes in low Magnetic Fields*, LHCb 2000-69 RICH

[36] S.Jolly (Imperial College), *Development of Ring Imaging Cherenkov Detectors for the LHCb Experiment*, PhD thesis, June 2004

[37] Rebecca Cikoski, *Cherenkov Candle Analysis of Multianode Photomultiplier Spectra*, Master of Science Thesis - The Univeristy of Edinburgh, 2003

[38] LHCB collaboration *LHCb Technical Proposal*, CERN/LHCC/98-4, LHCC/P4, 20 February 1998

[39] LHCB collaboration *LHCb Magnet Technical Proposal*, CERN/LHCC/2000-007

[40] LHCB collaboration *LHCb RICH Technical Design Report 3*, CERN/LHCC/2000-0037, 2000

[41] LHCB collaboration *LHCb VELO Technical Design Report*, CERN/LHCC/2001-0011, 31 May 2001

[42] LHCB collaboration *LHCb Inner Tracker Technical Design Report 8*, CERN/LHCC 2002-029, November 8, 2002

[43] LHCB collaboration *LHCb Outer Tracker Technical Design Report 6*, CERN/LHCC 2001-024, 14 September 2001

[44] LHCB collaboration *LHCb Muon System Technical Design Report 4*, CERN LHCC 2001-010 LHCb, 28 May 2001

[45] LHCB collaboration *LHCb Reoptimized Detector Design and Performance 9*, CERN LHCC 2003-030 LHCb, 9 September 2003

[46] R Plackett, *RICH1 re-optimization*: presentation to the RICH group meeting, 26 November 203,
Private communication

[47] I. Belyaev2, Ph. Charpentier1, S. Easo3, P. Mato1, J. Palacios4, W. Pokorski1, F. Ranjard1 and J. van Tilburg5, *Simulation Application for the LHCb Experiment*, Computing in High Energy and Nuclear Physics, 24-28 March 2003, La Jolla, California

[48] A.Bizzeti et al., *Design and Construction of the RPC Detector for the LHCb muon system*, Note LHCB 2001-027 Muon

[49] B.Bochin et al, *Wire Pad Chamber for LHCb Muon System*, LHCb 2000-003 Muon, 14 February 2000

[50] L.L. Jones, et al., *Electronics for the LHC Experiments*, CERN/LHCC/97-60(1997)158.

[51] Philips, *THE 2C-BUS SPECIFICATION VERSION 2.1 JANUARY 2000*: http://www.semiconductors.philips.com/acrobat_download/literature/9398/39340011.pdf

[52] *CMS website*, http://cmsinfo.cern.ch/Welcome.html/

[53] Hamamatsu, *R700-00-M64 Photomultiplier Tube*,
http://usa.hamamatsu.com/

[54] S.Eisenhardt, F.Muheim, the university of Edinburgh, *Performances of Multianode Photo Multiplier Tubes at Low Gain*, LHCb 2003-043 RICH, 25th November, 2003

[55] Vector Fields, Inc. *OPERA-3d Reference Manual*, http://www.vectorfields.co.uk/, March 2001, Oxford UK.

[56] Alex Howard, *MaPMT Testbeam Simulation in GEANT4*, MaPMT testbeam meeting, Private communication

[57] A.Pickford, *Performance of Multi-anode Photomultiplier Tubes for the LHCb RICH Detectors*, Elsevier Science, 13th of September 2004, 9 pages, 21 authors

[58] O. Toker et al., Nucl.Instr. and Meth. A340(1994) 572

[59] ASIC Labor Heidelberg, *Beetle - a readout chip for LHCb*, http://wwwasic.kip.uni-heidelberg.de/lhcb/

[60] Chirikov-Zorin et al., *Method for precise analysis of the metal package photomultipier single photoelectron spectra*, NIM A456, 2001, Pages 310-324.

[61] R. Cikoski, S.Eisenhardt, F. Muheim, *Analysis of Signal Spectra of Multianode Photo Multiplier Tubes*, LHCb 2004-016 RICH, 26^{th} March, 2004